X-630-72-48

INFRARED ABSORPTION OF CARBON DIOXIDE AT HIGH DENSITIES WITH APPLICATION TO THE ATMOSPHERE OF VENUS

JOHN FITZALLEN MOORE

DECEMBER 1971

Goddard Institute for Space Studies
2880 Broadway, New York, N. Y.

GODDARD SPACE FLIGHT CENTER
GREENBELT, MARYLAND

INFRARED ABSORPTION OF CARBON DIOXIDE AT HIGH DENSITIES WITH APPLICATION TO THE ATMOSPHERE OF VENUS

John Fitzallen Moore

Submitted in partial fulfillment of the requirements for the degree of Doctor of Philosophy, in the Faculty of Pure Science, Columbia University.

1971

by

John Fitzallen Moore

ERRATA

page	for	read
2	bulit	built
20	(C) only)	(CO only)
25	absorbed	adsorbed
55 (footnote)	$01^{1}1$ columns	$01^{1}0$ column
66	$00^{0}1$-$4^{0}0$,II	$00^{0}1$-$4^{0}0$,II
71 (equation 10)	$\Delta\theta$	$d\theta$
84	section VII	section VI
89 (Fig. 26)	$2^{0}1$ Fermi pair	$2^{0}0$ Fermi pair
103	interchange the order of Π_u, Σ_g^+	
124	add, after Avduevsky et al.: Baldwin, George C. An Introduction to Non-Linear Optics Plenum Press, New York (1967)	117

Report X-630-72-48, Goddard Institute for Space Studies.

ABSTRACT

Several previously undiscovered infrared absorptions have been found in carbon dioxide. All are normally forbidden, and were collision-induced in an absorbing cell whose combination of pressure and path length has a unique sensitivity for induced absorptions.

The most thoroughly studied new absorptions, in the 2.3μ region, were measured to 95 amagat over path lengths of 2400 cm. They are attributed to transitions from ground to the $3^1 1$ Fermi pair at 4248 and 4391 cm^{-1}. Total strength, including the associated hot bands, is $(6.2 \pm 0.9) \times 10^{-6}$ cm^{-2} ama^{-2}. The strength ratio between the two members of the pair has been used to find the ratio of the unperturbed matrix elements: that of the $00^0 0$-$11^1 1$ transition is 8 times larger than that of the $00^0 0$-$03^1 1$, with a crossing-over of intensities between the unperturbed and perturbed states.

Other newly-observed induced absorptions are attributed to simultaneous CO_2-N_2 transitions, and to the $00^0 0$-$00^0 2$ transition in CO_2. In addition, measurements were made for the first time of induced absorptivities in spectral "windows" -- regions usually considered transparent -- at 11.2, 10.0, and 8.75μ, and of the induced strength of the $00^0 0$-$01^1 1$ transition.

The absorption strengths measured in this study are combined with others from previously published work to obtain a number of CO_2 polarizability derivatives, and to exhibit regular progressions in strength versus increasing ν_2 quantum number, for both allowed and induced transitions.

Absorptivities in the windows were used to test and reject a hypothesis about the behavior of the far wings of allowed absorptions.

The experimental spectra herein and others previously published were used to predict the radiative transfer in a dry CO_2 model of the lower atmosphere of Venus. To cover wavelengths greater than 18.5μ, a synthetic spectrum of absorption (with terms proportional to density and to density squared) was prepared. The results indicate that the radiation balance in the lower atmosphere of Venus is adequately explained by a dry massive atmosphere of CO_2 with a layer of infrared-opaque clouds. The new absorptions in the 2.3μ region are significant to this conclusion, as without them there is not enough opacity to sustain Venus' 768K surface temperature.

Appendices include summaries of CO_2 properties and vibrational levels, a proposal for simplified labeling of members of Fermi multiplets, calculation of atomic polarizability derivatives, an analysis of the effect of mechanical anharmonicity, and a discussion of relative strengths of hot bands based on the radial wavefunctions for ν_2 and ℓ.

ACKNOWLEDGEMENTS

I wish to express my highest appreciation for Dr. Patrick Thaddeus, who at many junctures has been instrumental in surmounting serious impediments to this work. He suggested the original problem, stimulated my interest with his knowledge of Venus and of molecules, and enabled me to complete this work at the Goddard Institute for Space Studies.

Thanks are due to many others. Dr. M. J. D. Low taught me the techniques of infrared spectroscopy and provided experimental equipment, as well as many valuable suggestions and discussions. Dr. William S. Benedict enlightened me about intensity relations in CO_2 absorption, and provided the results of some of his earlier work; Dr. William W. Y. Ho and Dr. Henry D. Welsh provided a number of unpublished reports on their work. Dr. Richard Wattson and Dr. Robert deZafra constructively reviewed this work and made valuable suggestions on atmospheric models and on statistics; the late William K. Squires of Squires-Sanders/Computone and Dr. William Whitmore offered challenging discussions and stimulating ideas. Michael J. Antal, Jr., Richard B. Houska, Ronald Resnick, and my son, Robin B. Moore, helped in the laboratory with an interest and enthusiasm which should be valuable in their own future work.

I received suggestions, materials, and design information from:

DSD Company (Toruseals)

Conax Corp. (Pressure Glands)

Speer Carbon Co. (Graphite)

Aminco (Compressors)

Princeton Applied Research (Amplifiers)

Reeder & Co. (I-R Detectors)

Eastman Kodak (Irtran)

Marsh Instrument Co. (Pressure Gauges)

Steel and Alloy Tank Co. (Pressure Tank)

Financial support and facilities were generously provided by Lockheed Electronics, Squires-Sanders/Computone, Programming Methods, Inc., Computer Sciences Corp., and NASA's Goddard Institute.

I am grateful to my office-mates at Goddard: E. Sam Palmer, Marc L. Kutner, and IBM 360-95, who helped me to learn computer language and who put up with my mistakes ... and puns; and to Jo Koller and Margie Kavanau for typing. Finally, I thank my wife, Betty Ann, for bearing the extra burdens which my work meant to her, conceiving the window design which made the pressure cell successful, and forebearing my irregular schedules and moods.

TABLE OF CONTENTS

IV. EXPERIMENTAL RESULTS

V. THEORETICAL INTERPRETATION

VI. APPLICATION TO THE ATMOSPHERE OF VENUS

INDEX OF FIGURES

INDEX OF TABLES

I. INTRODUCTION

A. GENERAL

In infrared spectra, carbon dioxide has probably been the subject of more studies than any other polyatomic molecule. Its structure is simple enough to give spectra whose details can be interpreted with precision, but not so simple that these details can be predicted by an ab initio wave-mechanical description. Interest in it stems both from this and from its frequent presence in physically important situations: combustion and respiration, refining and chemical processing, and the atmospheres of the earth and other planets.

In most of these situations, the radiation properties of CO_2 can be predicted well on the basis of measurements at pressures of a few atmospheres or less. However, the atmosphere of Venus is mostly CO_2, with a depth and surface pressure which are too great to allow accurate predictions based on earlier experiments. Early opinions that CO_2 alone could explain Venus' high surface temperature (near 750K) through the greenhouse effect were rejected because radiation balance analyses showed the need for an infrared opacity higher than any indicated by laboratory measurements. Most of the explanations which were advanced required one or more additional constituents, with H_2O being the one most commonly proposed. More recently, Thaddeus (1964) suggested that, at high pressures, a combination of collision broadening and induction of forbidden infrared absorption

could provide sufficient greenhouse effect to explain the surface temperature even with dry CO_2 alone.

B. PURPOSE

The purpose of this study was to complement the many previous observations of CO_2 infrared absorption at moderate pressures or path lengths by observations at a combination of path lengths and pressures large enough to permit measuring weak absorptions proportional to density squared. To that end, unique equipment was bulit with greater capacity for producing pressure-dependent effects, and with sufficient long-term stability to permit accurate estimates of absorption even if none of the spectrum remained transparent enough to act as a reference level. Observations made with this equipment were to be applied to models of the atmosphere of Venus and to the properties of the CO_2 molecule.

II. EXPERIMENTAL EQUIPMENT

The equipment in this study consisted of a specially-designed high-pressure, long-path cell and a conventional spectrophotometer.

A. LONG-PATH CELL

The absorption cell employed the multiple-reflection optics originally designed by White (1942). The problems which had to be solved included pressure sealing, stability of mirror alignment, temperature control, and window design.

1. Vessel

The pressure tank and its dimensions are shown in Figure 1. It is made of type 316 stainless steel, whose strength permits thinner walls than any other alloy not requiring annealing; its resistance to hydrogen embrittlement makes it suitable for possible experiments with hydrocarbons. The cylinder was formed from a rectangle of sheet stock 2.1 cm thick, with a welded seam, flange, and closed end. The tank and its removable cover weigh about 201 kg and 44 kg, respectively. Its internal volume is approximately 0.0403 m^3 (1.42 ft^3).

A 4-to-1 safety factor was used, designing to 827 bar in order to have maximum working pressure of 207 bar (3,000 lb/in^2, 204 atm). The completed tank was X-rayed, and withstood a hydrostatic test at 310 bar.

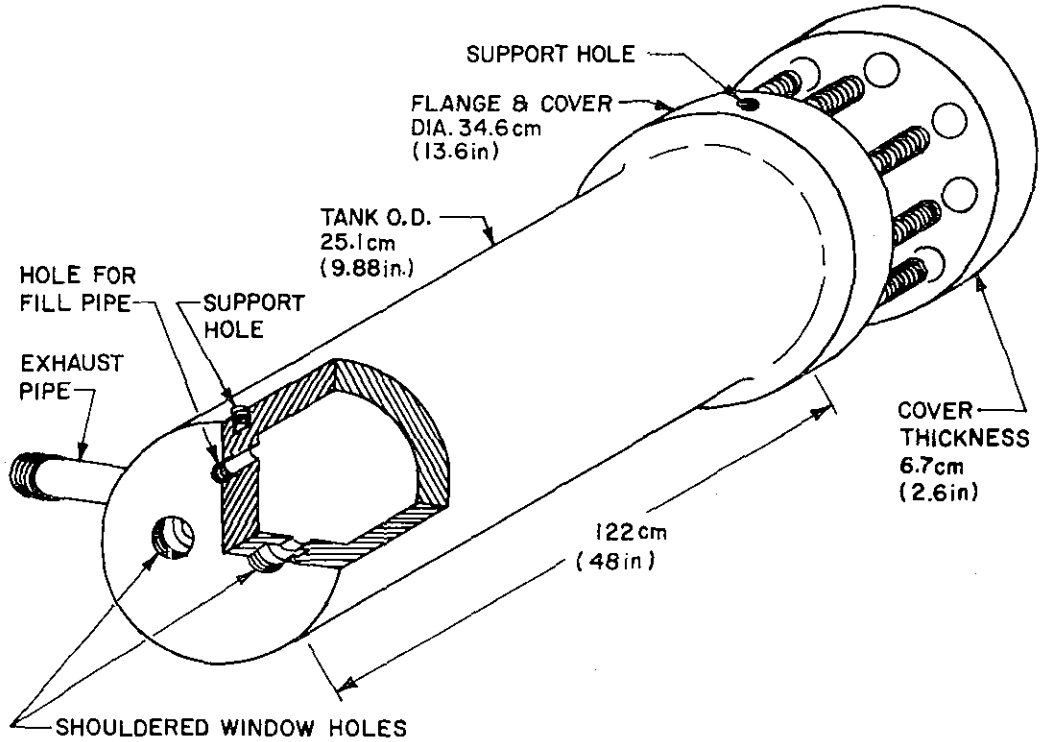

Fig. 1. Pressure tank to contain the White cell optics. The sealing groove on the far side of the flange and the electrical feedthrough connector (near the bottom of the cover) are not visible.

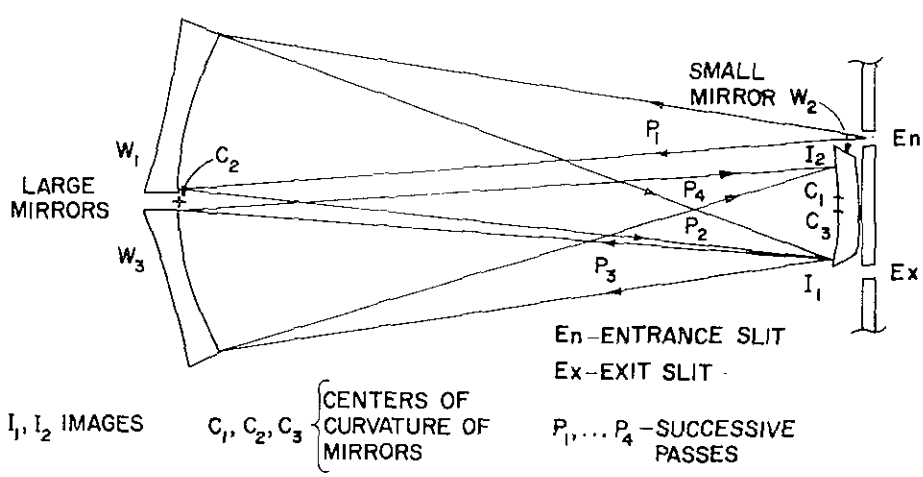

Fig. 2. White cell optics, showing the first four passes. En and I_1 are symmetric with respect to C_1; subsequent pairs of images are symmetric with respect to C_3 and C_1, alternately. By decreasing the angle between W_1 and W_3, the centers of curvature C_1 and C_3 are brought closer together, increasing the number of passes in multiples of four. The last reflection from W_3 leaves through the exit slit, and is symmetric with the first pass P_1, with respect to the center line.

The cover is bolted to twelve $1\frac{1}{4}$ - 8 studs mounted on the tank flange. All electrical connections to the interior are made via a Conax high-pressure electrical feed-through in the cover. The fixed end has holes for the windows and for gas filling; a full-length V-channel is welded inside the tank as a guide for the optics platform. In order to avoid the higher thermal conductivity of a supporting structure under the tank, the top of both tank and cover are fitted with threaded holes for suspension. The cover is suspended from a trolley which runs on an overhead channel, so that it can be removed and replaced without disturbing mirror alignment.

The cover is pressure-sealed with a 23 cm diameter ring which deforms inelastically when the bolts are tightened. A Toruseal hollow stainless-steel O-ring with a 0.1 mm Teflon coating gave better results than a solid copper ring or an uncoated Toruseal.

2. Internal Optics and Mounting

To form the White multiple-reflection long-path cell, three Vycor* mirrors, all with a radius of curvature of 100 cm, are inside the tank. One mirror, 4.45 cm high by 9.36 cm wide, is placed between the entrance and exit window slits. Two larger mirrors are mounted side

---

* Vycor, made by Corning Glass Works (Corning, N.Y.), is 96% silica, 3% B_2O_3, and smaller quantities of Al_2O_3, CrO_2, Na_2O, and As_2O_3. Its strength, melting point, and low coefficient of thermal expansion (8×10^{-7} per °C) are close to those of fused quartz.

by side at the opposite end of the tank, 100 cm from the first mirror. Their height and width are 15.24 by 10.16 cm (6 by 4 in), with outer corners beveled to fit within the tank's internal diameter of about 21.1 cm; the beveling reduces reflective area by 13%. Figure 2 shows the configuration and the first four passes.

Each mirror is gripped at its corners by fingers extending from a thin stainless-steel backing plate; each backing plate has three 2 - 56 threaded studs for mounting and adjustment. The studs pass through stainless-steel compression springs, through oversize holes in vertical stainless-steel plates, and then through coned bearing sleeves. These are necessary to keep the studs centered and to avoid small non-reversible shifts in mirror alignment during temperature changes and vibration.

The vertical support plates are mounted on a removable platform, which provides kinematic mounting, resistance to vibration, and accurate maintenance of mirror spacing over a wide range of temperatures, and permits initial setup and adjustment to be made outside the tank. The first design, used in the initial series of runs, was made of Vycor tubing and rods, as shown in Figure 3. It proved to be too springy and fragile, and was replaced by a stainless-steel plate 0.32 cm thick, stiffened with a welded U-channel underneath. Mirror spacing is maintained by permitting the large mirrors' vertical support plate to slide lengthwise on the platform, and spring-loading it

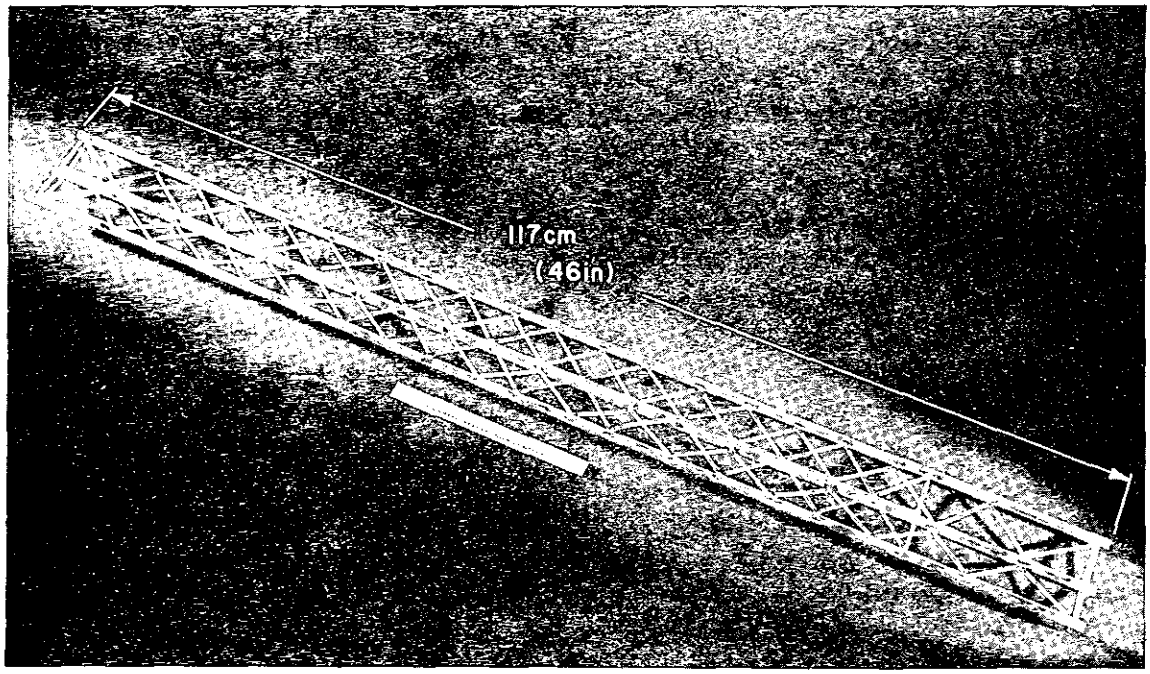

Fig. 3. Optical platform used in early measurements, made by fusing Vycor rod and tubing into a truss structure.

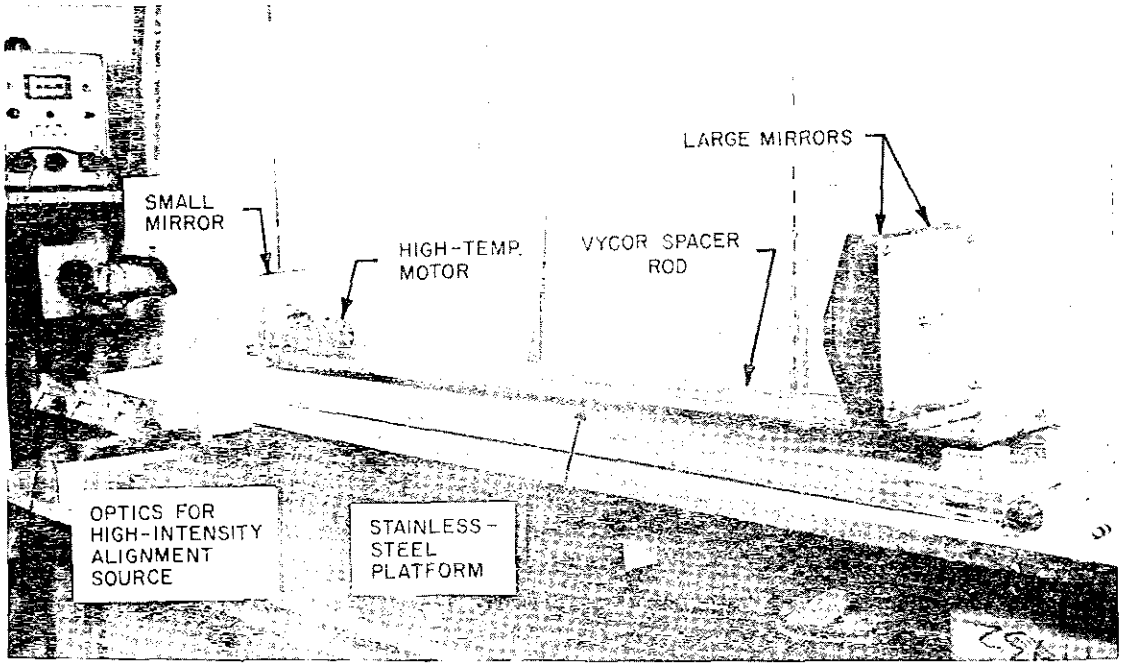

Fig. 4. Stainless-steel optical platform assembly. The adjusting screws for the large mirrors pass through the rectangular supporting plate at right; the stirring motor and fan are near the small mirror W_2, at left.

against two Vycor spacer rods. As with the Vycor platform, the rods' expansion exactly compensates for the change in curvature of the Vycor mirrors. This amounts to only 0.24 mm for a 300C temperature rise (or about 1 cm of path length with 40 reflections). Without the Vycor rods, the twenty-times greater expansion of stainless-steel would cause serious defocussing.

The spacer rod ends are in the plane of the mirror mounting surface, cancelling any expansion in the studs and other supporting structure. The two points on the vertical support plate which are pressed against the spacer rods (restraining them from lengthwise motion) also rest on the platform, which restrains them from vertical motion. A front-mounting point rests in a small V-groove on the platform, so that it is restrained vertically and laterally, but not longditudinally. There are thus six non-redundant constraints, as required in kinematic mounting. Hold-down springs are used at both front and rear. The assembly is shown in Figure 4. Six-point kinematic design is also used in mounting the platform in the tank.

3. Window Design

The White cell is normally used with external optics which magnify the source by a factor of two, and perform a compensating reduction before the beam enters the monochromator. Since the maximum slit size is 12 mm high by 2 mm wide, the appropriate window size is 24 by 4 mm. A good combination of mechanical strength and infrared

transmissivity is given by Eastman Kodak's polycrystalline materials: Irtran-2 (Zns) has a long-wave limit of 14 microns, and a rupture modulus of 14,100 psi; Irtran-4 (ZnSe) can be used to 22 microns, but has only 6,100 psi rupture modulus. Window thickness is 2 mm for Irtran-2 and 3.2 mm for Irtran-4; 345 bar tank pressure causes shear stresses of 3,100 and 1,940 psi, respectively.

Window plugs were made to fit the holes in the tank; each plug is shouldered and grooved to hold a Toruseal stainless-steel O-ring 4.45 cm diameter, which is compressed against a mating shoulder in the tank hole by a threaded locking ring. An Irtran blank is wrung against the inner surface of each plug, and held on by a slotted cover plate and a threaded holding ring. To test the windows, a hydrostatic fixture was made with hole dimensions duplicating those of the tank holes; in order to observe window behavior, an NE-51 neon bulb was placed inside the fixture and powered by wires through the pressurizing pipe. In all window plugs with slit-shaped windows, the Irtran failed by crazing without leaking, considerably below the predicted "safe" pressure*.

---

* The "safe" pressure is given by the following formula (courtesy Eastman Kodak):

$$T = 0.75\, AB \sqrt{PF/R\,(A^2+B^2)}$$

where P is the pressure and R the rupture modulus, both in units compatible with the thickness T and the slit dimensions A and B.

A possible explanation is that the high pressure caused enough plastic flow to shift the sintered grain boundaries. The neon bulb withstood 690 bar.

In an effort to provide more even support, new plugs were made with the slit replaced by a row of circular holes. Pressures up to 413 bar (6,000 psi) were reached without failure in the final configuration selected, which has six holes 3.9 mm in diameter, and is shown with all fittings in Figure 5. One window is Irtran-2 and one is Irtran-4, so as to average the wavelength dependence of transmission loss in the two materials. The flat windows cause vignetting, reducing the energy to about 20% of that obtained by Perkin-Elmer (1959) with the same mirror design, but with convex windows.

4. Temperature Control and Measurement

In addition to compensating the optical system for thermal expansion, as discussed previously, it is extremely important to avoid temperature gradients. These can ruin optical alignment through differential expansion of the supporting structure. Worse, temperature variations are much more effective at high pressure in deflecting or breaking up a light beam: for given ΔT, the change in refractive index is proportional to density. Moreover, the temperature difference required for

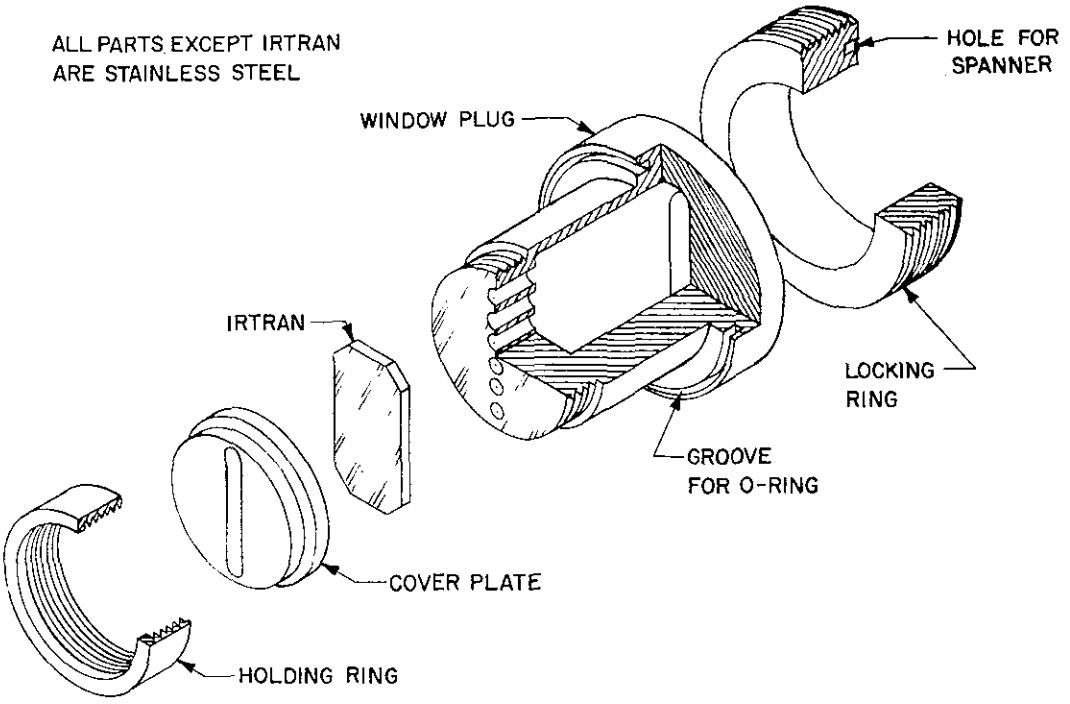

Fig. 5. Window assembly, exploded view, about 2/3 size.

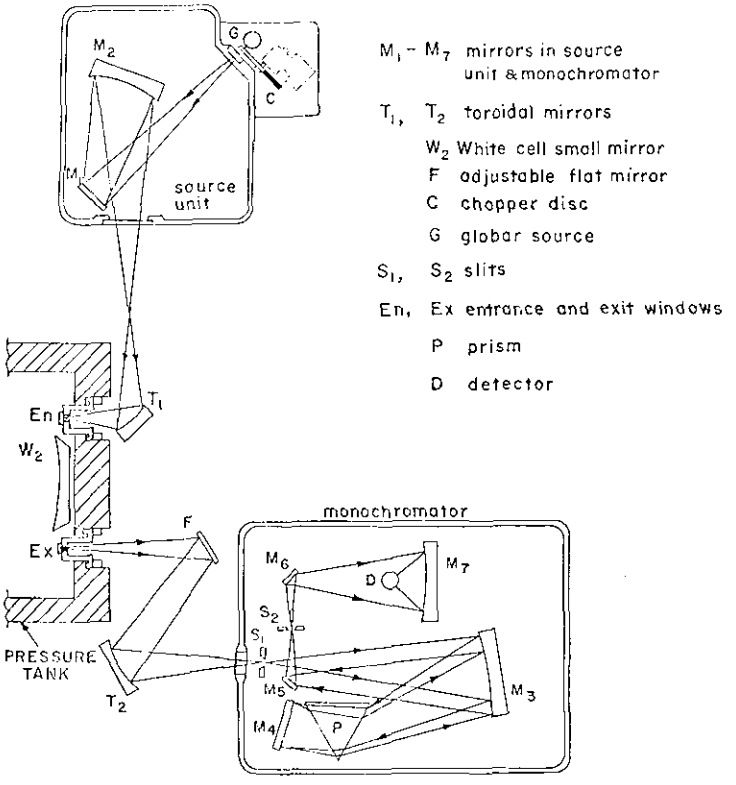

Fig. 6. External optics, about 1/8 size. For the light path within the pressure tank, see Figure 2. The wavelength drive, which rotates the Littrow mirror M_4, is not shown.

the initiation of turbulence decreases inversely as the square of the density (McAdams, 1954)*.

In this study, the initial goal was to reach 558K (600F), using electrical heating and an insulated jacket. In initial runs, the signal was totally lost for an internal temperature rise of only 30C (54F). As it disappeared, large fluctuations suggested the presence of strong convection turbulence -- probably due to uneven heating. This was confirmed by noting variations in the readings of thermocouples on the outer surface of the tank. More seriously, room-temperature signal levels varied by up to 10% from day to day, apparently due to small temperature changes.

To improve heat distribution, the tank was jacketed with 3.2 mm of annealed copper, hammered in place for best thermal contact, and held by steel strapping. The entire tank was then wrapped with about 5 cm of fiberglass insulation, covered by aluminum foil to block air convection through the fiberglass. A removable insulating cap of fiberglass and sheet aluminum was applied to the cover.

Temperatures are measured by a series of copper-constantan thermocouple junctions, referenced to an ice bath. The thermocouples,

---

* As a consequence, the long-path cell at Ames is reported to suffer beam breakup with temperature differences of a few tenths of a degree.

whose purpose is less to measure temperature than to assure equilibrium, are distributed around the exterior and interior of the tank. Those inside are sheathed in stainless steel jackets 1.6 mm diameter with welded closed ends and MgO electrical insulation. They enter the tank through a Conax 10,000-psi packing gland.

The laboratory was air conditioned to keep ambient temperature constant. Optical performance at elevated temperatures has been improved to the point where spectra can be taken, but without the stable absolute signal level required for the work in this investigation. Turbulence seems to have been cured, but beam alignment is lost because of temperature differentials in the platform and support plates. As a result, the findings herein are restricted to room temperature. Modified means of supporting and adjusting the mirrors have been designed and will be installed to make the long-path cell stable over a wider temperature range, in its new location at New York University.

5. Internal Mixing

The Conax fitting also carries wires to power a stirring motor mounted on the optical platform in the tank. Its purpose is to provide mixing so as to reach thermal equilibrium more rapidly, and to avoid stratification when mixtures of gases are in the tank.

The motor was designed to operate at 600K (620F) without introducing spectrographic contaminants. A commerical induction motor was

completely rebuilt to eliminate all organic materials, retaining only the laminated-iron field and the copper-and-iron armature. Though these appeared to be varnish-free, they were cleaned in acetone and degreased in Freon vapor, as were all other parts. New unlubricated bearings were machined from organic-free graphite and mounted in adjustable steel bearing plates. A new field coil was wound from copper wire insulated with specially made unvarnished fiberglass braid; mica underlayment on the field iron prevented abrading the brittle braid.

The motor, which can be seen in Figure 4, was fitted with a cast aluminum two-bladed propeller. It has been test-operated for six hours in an oven at 600K. In the tank, the motor has run at vacuum and at high pressures.

Another method of mixing employed a commercial magnetic stirrer. With this, a motor-driven Alnico magnet outside the tank was able to spin a glass-encapsulated rotor magnet inside the tank, through a gap of 5 cm, including the 2.1 cm thick stainless steel wall. However, mixing efficiency was poor because of the small ratio of rotor size to tank volume, and no practical way was found to attach a propeller with necessary supports and bearings.

B. EXTERNAL COMPONENTS

Outside the pressure cell, the major subsystems are the optics, including the source and monochromator; the electronics, which

comprise source stabilization and phase locking, signal amplification, and recording; and gas handling for both the high-pressure and the flush systems.

1. Optics

A model 12-B spectrometer, as described by Perkin-Elmer (1956) was cut so as to separate the source unit from the monochromator and wavelength drive unit. Mating the spectrometer to the pressure cell requires additional optical components; mirrors are used in order to avoid the losses and dispersion which would occur with lenses over the wide wavelength range. The only way to avoid excessive distance between mirrors is to use them off-axis. However, image quality from a spherical mirror deteriorates badly for angles of more than 10° from the axis (20° included angle), whereas toroidal mirrors are designed for a specific angle of off-axis use. Geometrically, off-axis focussing requires a prolate spheroid, but the two orthogonal circular curvatures of a toroidal mirror bear the same relationship to the spheroid curvatures as a sphere bears to the center of a paraboloid. One toroidal mirror, with radii 7.42 and 14.84 cm, is used to turn the beam from the source into the pressure cell. The formula for the half-angle is $\cos^2\theta = R_1/R_2$, giving $\theta = 45°$, or a total turning angle of 90°. The focal length is given by $2f^2 = R_1R_2$, so that $f = 5.25$ cm. This mirror is mounted in a frame with adjustments for tilt, rotation, and position.

A toroidal mirror and a flat mirror are used to bring the beam into the monochromator. In this case, primary adjustment is via the flat mirror, which has a three-point suspension. The toroid has radii of 21.65 and 28.87 cm, for a turning angle $2\theta = 60^\circ$ and focal length f = 12.5 cm.

Figure 6 shows a top view of the external portion of the optical layout. The source is a Globar SiC rod about 0.5 by 5.1 cm, with silvered ends. It operates at about 1400K (2061F) with 200 watts of dissipation. Its radiation is chopped at 39 Hz by a sector wheel.

The double-pass monochromator has two geared-together slits: one to narrow the input beam and the other to narrow the spectral region. As a result, signal intensity is approximately proportional to the square of the slit width. Wavelength selection is accomplished by rotating the Littrow mirror behind the NaCl prism, and because of varying dispersion in the salt, wavelength and resolution are not linear functions of the Littrow position.

The monochromator Littrow drive uses a synchronous motor with a gear box providing 1, 2, 4, or 8 minutes per turn. New gears were made, extending the range to 16 and 32 minutes per turn.

The detector is a high-speed thermocouple with a rectangular target 0.2 by 0.02 cm. Its d-c responsivity is 23 μ volt/μ watt; its time

constant τ is 10 milliseconds, so that the net responsivity is 8 μ volt/ τ watt at the chopping frequency F of 39 Hertz, based on

$$S_\tau / S_o = \sqrt{1 - 4\tau F \tanh (1/4\tau F)}$$

which relates the r. m. s. signal S_τ for a given time constant to that for S_o, the "perfect response" to square-wave chopping with a 50% duty cycle.

The only other optical component is an alignment bench, using a collimated high-intensity Hg-vapor lamp to set up the mirrors before inserting them in the tank. During alignment, the light is focussed on a sheet-metal mask with holes the same as those in the tank's entrance and exit windows.

2. Electronics

The thermal power received by the detector may be as little as 10^{-13} watts. After allowance for conversion losses in the detector thermocouple, the corresponding electrical power is in the order of 10^{-18} watts. The usual beam-chopping technique is employed, using a Princeton Applied Research HR-8 lock-in synchronous amplifier at 39 Hz in order to obtain its best noise figure (referred to room temperature) of 0. 5dB, and to avoid a simple ratio of line frequency. A type B preamplifier is connected to the amplifier through a remoting cable so that the preamp can be as close as possible to the detector, minimizing noise and pickup. Under these conditions, sensitivities

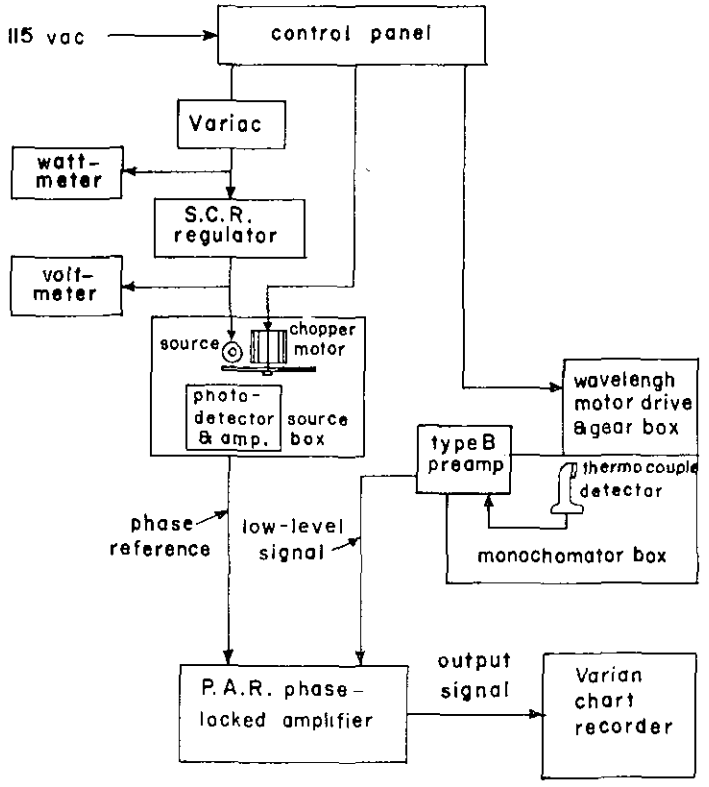

Fig. 7. Electronics block diagram. Lines from the control panel are 115 vac, while that from the SCR regulator is from 25 to 35 vac. The phase reference and low-level signal are chopped at 39 Hertz; the signal output is d-c, varying from zero to 10 volts.

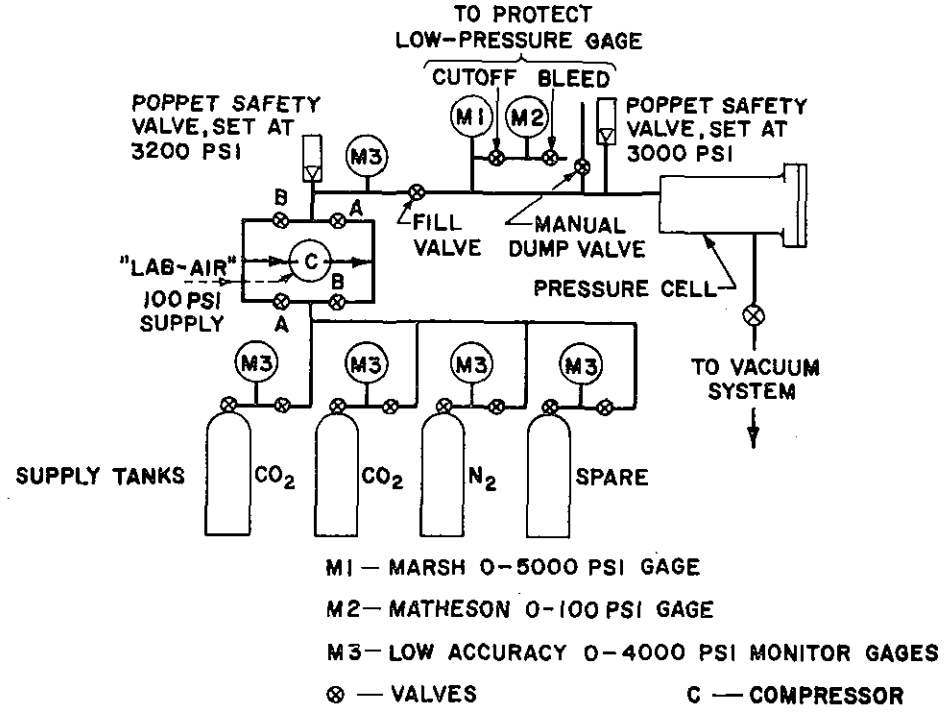

Fig. 8. High-pressure gas system.

of 2×10^{-9} volts full scale can be used with an output time constant of 10 seconds. Chopping phase is sensed by a photo-transistor placed next to the chopper; the photo-transistor drives a reference input. The amplifier output, ranging from 0 to 10 vdc, drives a 10-inch chart recorder geared to synchronize with the Littrow drive.

Since the major operating criterion is long-term stability, special provisions are required to keep the Globar emission constant, in spite of line voltage variations. In order to obtain greater stability than with constant-voltage transformers, a silicon controlled rectifier regulator was built. In this circuit, the SCR's reduce the nominal 115 vac to 25-35 vac by varying the conduction time. Regulation rate and output voltage are separately adjustable.

Figure 7 gives the electronics block diagram.

The overall stability of the equipment (including internal and external optics, Globar, amplifier, and chart recorder) was tested in a number of long runs (up to 36 hours) at fixed settings. Maximum variation was ±1.5%, and r.m.s. variation was under 1%.

3. Gas Handling

Gases, obtained from the Matheson Corporation, had compositions (given by the supplier) as listed in Table 1.

TABLE 1: GAS PROPERTIES

Gas	CO_2	N_2(filling)	N_2(flushing)
Grade	Coleman	Prepurified	Extra Dry
Pressure, psi	838*	3500	2200
Other Gases, ppm:			
O_2	4	8	300
$CO + CO_2$	5 (C) only)	1	25
$N_2 + N_2O$	50 + 4	-	-
H_2	4	2	?
hydrocarbons	5	0.5	?
H_2O	10	2	11
Total	100	40	3000

*vapor pressure of liquid at room temperature

The complete high-pressure system is shown in Figure 8. A supply manifold is connected to four tanks: one N_2, one spare, and two CO_2. When filling the pressure cell, evaporative cooling of the liquid CO_2 in the first tank causes its vapor pressure to drop by as much as one-third; the manifold is then transferred to the other CO_2 tank. The spare tank is used to hold gases temporarily when it is not desired to dump them. An Aminco #46-14025 compressor, driven by a standard 100-psi laboratory air pressure line, is

connected between the supply manifold and the tank, using a four-valve bridge. By opening the appropriate pair of valves A and B (Figure 8), the compressor can be used in either direction or can be bypassed. The compressor, valves, and piping all have 689 bar (10,000 psi) maximum rating. Two poppet safety valves are used: one on the manifold and one on the pressure cell. Pressure is measured by a Marsh #200-3S gage, with adjustable zero set and an accuracy of 0.2%. For low pressures, it is supplemented by a Matheson 0-100 psi gage. A roughing vacuum system is used before filling, to aid in baking off impurities adsorbed on the pressure cell walls.

To exclude ambient CO_2 and H_2O from the external optical system, a transparent dry-box was built around the source and the external mirrors. The wall on the side next to the pressure cell is glass; other walls and the top are acrylic. The dry-box is connected to the monochromator by a vinyl tube through which the beam passes; all joints are sealed with silicone-rubber cement or with tape. Flushing is accomplished by low-pressure N_2, which is introduced near the infra-red source, flows past the mirrors and into the monochromator, and is then dumped. A half-hour of flushing reduces the effective amount of H_2O to 0.6 cm-atm and of CO_2 to 0.2 cm-atm. This includes not only the 260-cm external optical path, but also the 2400-cm path in the N_2-filled tank.

C. COMPARISON WITH OTHER EQUIPMENT

In spite of the many long-path cells in existence, this study was able to discover previously unobserved absorptions through a combination of pressure and path length with greater sensitivity to pressure-induced effects. For permitted transitions, the sensitivity of an absorption cell depends on the total number of molecules in the path, proportional to the density ρ times the path length L. Values of the product ρL are shown in Figure 9 on the family of light lines sloping downward at 45°; they show that the cells at Ames and Penn State are nearly ten times more sensitive for allowed absorptions than the one used in this study. However, induced absorption is proportional to the number of molecular pairs; an appropriate figure of merit is density squared times length. This is shown in the steeper family of light lines sloping downwards at about 63°. From this viewpoint, the work herein is about 1.8 times more sensitive than any other in seeing pressure-induced lines, with a $\rho^2 L$ of 2.2×10^7 cm-ama^2, as compared to 1.2×10^7 for the cell at Penn State (not yet used with pressurized CO_2), 9.1×10^6 in work by Adel & Slipher (1934), and 3.4×10^6 for the cell at Ames.

In Figure 9, the major reason that points for design and actual operation are not the same is experimental difficulty, the chief problem being signal stability with respect to vibrations, adjustments, and temperature variations.

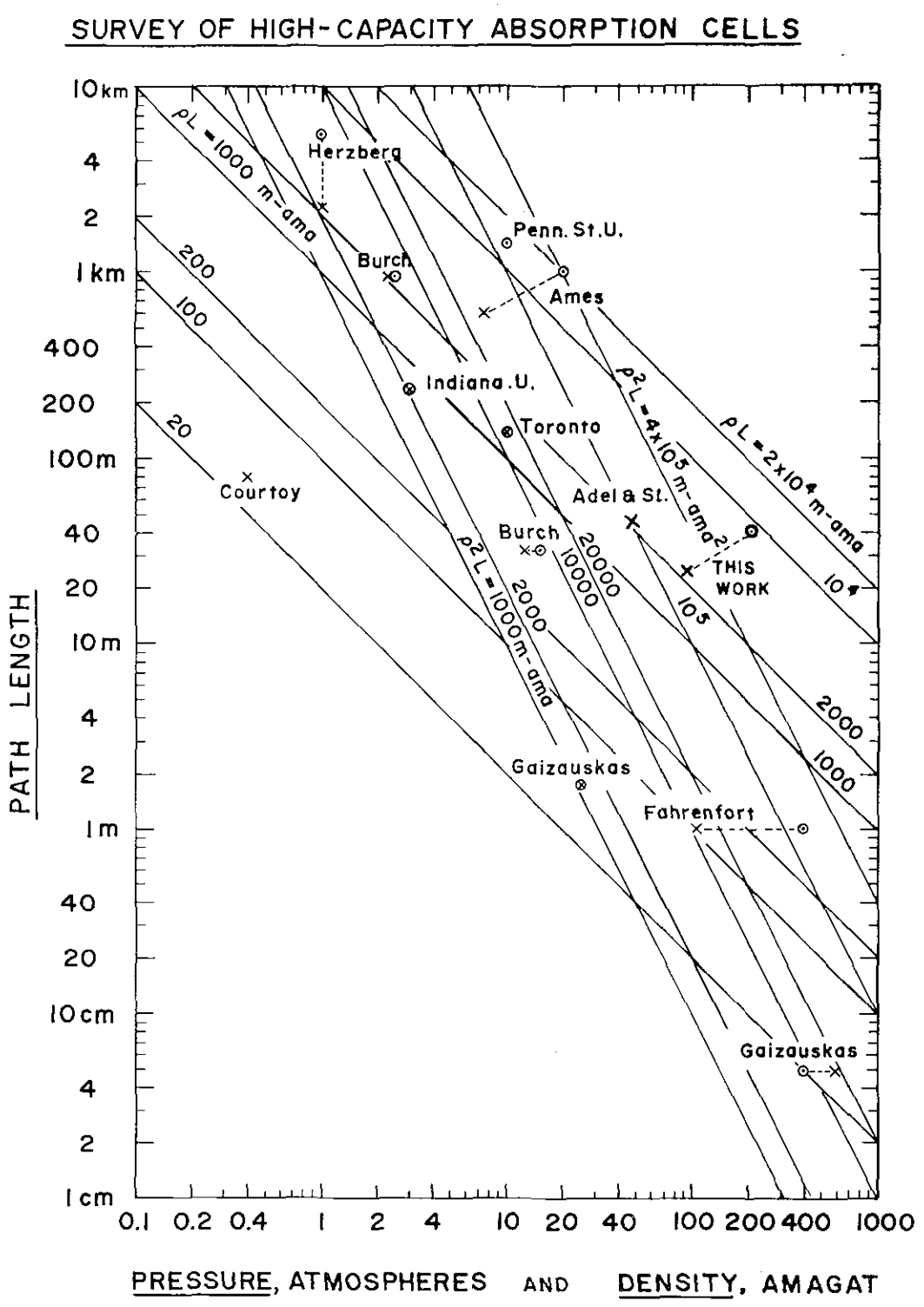

Fig. 9. The maximum capability of each cell is indicated by ⊙, where the abscissa should be read in atmospheres (as design pressure is independent of the gas used). The greatest published use of each cell with CO_2 is given by X, with the abscissa in amagat (as absorption is a function of density).

NOTE ADDED IN PROOF: A cell with a planned capability of 80 meters and 100 atmospheres has recently been built at Martin-Marietta, Denver (Pilston, 1972).

III. EXPERIMENTAL PROCEDURES

The experimental plan was to measure infrared absorption at high densities of CO_2 over the range from 1 to 14 microns, seeking absorptions in regions previously considered transparent. If any new absorptions were found, they were to be measured at enough different pressures to establish the nature of their density dependence. Nitrogen spectra were to provide reference levels with which the CO_2 spectra could be compared.

A. ADJUSTMENT

The White cell mirrors were aligned out of the pressure cell, using the high-intensity source to render the image patterns visible. The procedure recommended by Perkin-Elmer (1959) was followed until an even row of 11 images was obtained on the small mirror*, giving a path length of 2400 cm. The mirrors were then installed in the tank, and final adjustment was made with the Globar source in operation.

B. OPERATION

1. Sequence of Spectra

The basic approach was to compare the CO_2 spectra with a stable reference (because of the possibility that no wavelength regions

*For N images, there are 2N + 2 passes through the cell.

would be free from absorption). Before filling with gas, the tank was evacuated, and heaters brought the interior to 65C to bake out absorbed impurities. After the tank cooled, nitrogen was added, and N_2 spectra were taken at ambient pressure and at 7, 14, 21, and 42 bar (600 psig). Signal level showed no change with pressure, except for a random run-to-run variation of about 1% which is believed due to the gas flow causing mechanical hysteresis in the White cell mirror supports. The results of the N_2 runs were averaged to form a reference with which the CO_2 levels were compared.

The N_2 was then replaced by CO_2. In spite of heating the inflow pipe to counteract evaporative cooling in the CO_2 supply tank, temperature inhomogeneities were unavoidable, and initially caused signal loss of about 30%. Though the signal returned close to its original level within two hours, irregular slow drifts continued. The first five CO_2 spectra were therefore taken only after equilibrating overnight or longer. In these spectra, the signal level in the absorption-free "window" near 5700 cm^{-1} (1.75μ) was the same as the corresponding region for N_2 within 1%, indicating that no unexpected shift of level occurred with CO_2.

The first five CO_2 spectra, at pressures from 46 to 52 bar, were followed by several with mixtures of CO_2 and N_2. The tank was then evacuated and refilled with N_2 to check for long-term drift in signal level; results were consistent with those found previously.

After preliminary analysis of the CO_2 spectra had estiablished the presence of induced absorptions, a normalizing procedure was worked out to permit shorter equilibration times, and CO_2 spectra were then taken at fifteen additional pressures from 8.6 to 56 bar. Concluding runs were taken with N_2 in the tank, and with several reference absorbers.

2. Control Settings

The monochromator's highest resolution could not be used because the complex optical system reduced light intensity to about 5% of that obtained in normal use of the spectrometer. In order to get adequate signal-to-noise ratio without excessive scanning time, slit widths of 0.025 to 0.050 mm were used near 2.3 μ wavelength (giving 35 to 60 cm^{-1} resolution) and of up to 1.5 mm at 10 μ (giving 30 cm^{-1} resolution). Finer resolution was not required, as rotational structure was obliterated at the pressures that were used.

Amplifier time constants of 0.3 to 3.0 s enabled the entire spectrum to be covered in under three hours; regions of special interest were examined in fine detail at closely spaced, fixed wavelength settings.

C. WAVELENGTH CALIBRATION

Calibration at wavelengths longer than 5μ was based on 0.04 mm polystyrene film, with a reference spectrum by Plyer & Peters (1950). From 2 to 5μ, reference spectra from Perkin-Elmer (1952) were used for absorptions in water, methanol, and 1, 2, 4-trichlorobenzene. From 1 to 2μ, CO_2 absorptions were used, with reference spectra from the work of the group at Aeronutronics.*

---

* In order of increasing energy: Gryvnak, Patty, Burch, & Miller (1966), Burch, Gryvnak, & Patty (1968), (1964), (1965C), (1965A), (1967), (1965B).

IV. EXPERIMENTAL RESULTS

A. INTRODUCTION

The apparatus described in previous section was used to obtain CO_2 spectra from 1.05μ to 14μ as a function of density to 95.1 amagat, over a path length of 2400 cm. In addition to many well-known allowed lines, a number of weaker bands were observed at 3.3μ, 2.3μ, and 2.14μ. These have been identified as collision-induced because of their position, their density-squared absorption dependence, or both.

Measurements have been made of the strengths of several of these induced transitions; some were previously unobserved, and other had previously been observed so weakly as to prevent their measurement.

Attention was also directed to several "windows" — regions between strong absorptions, and normally considered transparent — near 11.2, 10.0, and 8.75μ. Measurements of their induced absorptivities versus wavelength were obtained.

B. OBSERVATIONS

1. 2.3μ Region

This is the only region where clearly defined induced transitions cause opacity in a window, so that more detailed results than in any other region could be obtained.

Two absorption bands with no visible rotational structure have been observed at 4240 ± 20 and 4380 ± 20 cm^{-1}. In both bands, optical thickness is proportional to density squared over a density range of more than 10 to 1, with optical thicknesses at the centers of the bands being 0.49 and 0.55 over the 2400 cm path, at 95.1 amagat. Figure 10 shows the induced absorptivity versus wavelength, and indicates corrections for the far wings of allowed lines, as discussed in section IV. D. 1. Total induced strength of the overlapping pair is $(6.2\pm0.9)\times10^{-6}$ cm^{-2} ama^{-2}, with the individual induced strengths of the bands centered at 4240 and 4390 cm^{-1} being $(2.6\pm0.5)\times10^{-6}$ and $(3.6\pm0.6)\times10^{-6}$ cm^{-2} ama^{-2}.

The new bands are identified as transitions of the common isotopic species from the ground level to $3^{1}1$, I and $3^{1}1$, II (the Fermi pair whose unperturbed states are $03^{1}1$ and $11^{1}1$), with wavenumbers 4247.714 and 4390.628 cm^{-1}, according to the formulae in Appendix A, sections 4 and 5. The levels have previously been observed only in hot bands. The assignments are made on the basis of position and spacing, and are confirmed by the ρ^{2} dependence, which is not appropriate for allowed lines.

The region from 4000 to 4600 cm^{-1} is lacking in strong absorptions, as can be seen in Table 2. This gives, for various isotopic species, all allowed transitions with strengths greater than 10^{-7} cm^{-2} ama^{-1}.

TABLE 2: ALLOWED CO_2 TRANSITIONS, 2.3μ REGION*

Isotopic Species†	Transition Label Old	Transition Label New†	Energy cm^{-1}	Strength $cm^{-2}atm^{-1}$
626	$02^20\text{-}01^12$	same	3980.60	2.0×10^{-6}
628	$00^00\text{-}22^00$	$00^00\text{-}6^00$, III	3987.61	4.0×10^{-5}
626	$01^10\text{-}00^02$	same	4005.94	2.2×10^{-5}
627	$00^00\text{-}22^00$	$00^00\text{-}6^00$, III	4023.48	2.0×10^{-6}
626	$02^00\text{-}01^12$	2^00, I-01^12	4030.32	1.0×10^{-6}
628	$00^00\text{-}30^00$	$00^00\text{-}6^00$, IV	4167.91	2.4×10^{-6}
626	$01^10\text{-}08^20$	$01^10\text{-}8^20$, I	4379.85	1.0×10^{-7}
626	$00^00\text{-}07^10$	$00^00\text{-}7^10$, I	4416.15	1.0×10^{-6}
638	$01^10\text{-}01^12$	same	4485.60	4.2×10^{-7}
638	$00^00\text{-}00^02$	same	4508.75	5.0×10^{-6}
637	$00^00\text{-}00^02$	same	4524.88	4.6×10^{-7}
636	$00^00\text{-}15^10$	$00^00\text{-}7^10$, II	4527.28	3.5×10^{-8}
626	$01^10\text{-}16^00$	$01^10\text{-}8^00$, II	4529.87	6.0×10^{-7}
626	$01^10\text{-}16^20$	$01^10\text{-}8^20$, II	4578.09	4.8×10^{-7}
626	$00^00\text{-}15^10$	$00^00\text{-}7^10$, II	4591.12	5.5×10^{-6}
626	$11^10\text{-}07^11$	3^10, II-7^11, I	4611.31	1.0×10^{-6}
628	$01^10\text{-}01^12$	same	4614.78	2.8×10^{-5}
627	$01^10\text{-}01^12$	same	4630.37	2.6×10^{-6}
628	$00^00\text{-}00^02$	same	4639.50	3.5×10^{-4}
627	$00^00\text{-}00^02$	same	4655.21	3.4×10^{-5}
626	$01^10\text{-}24^00$	$01^10\text{-}8^00$, III	4662.15	2.7×10^{-7}
636	$02^20\text{-}06^21$	$02^20\text{-}6^21$, I	4673.68	4.0×10^{-6}

* Courtesy William S. Benedict.

† For explanation, see Appendix B.

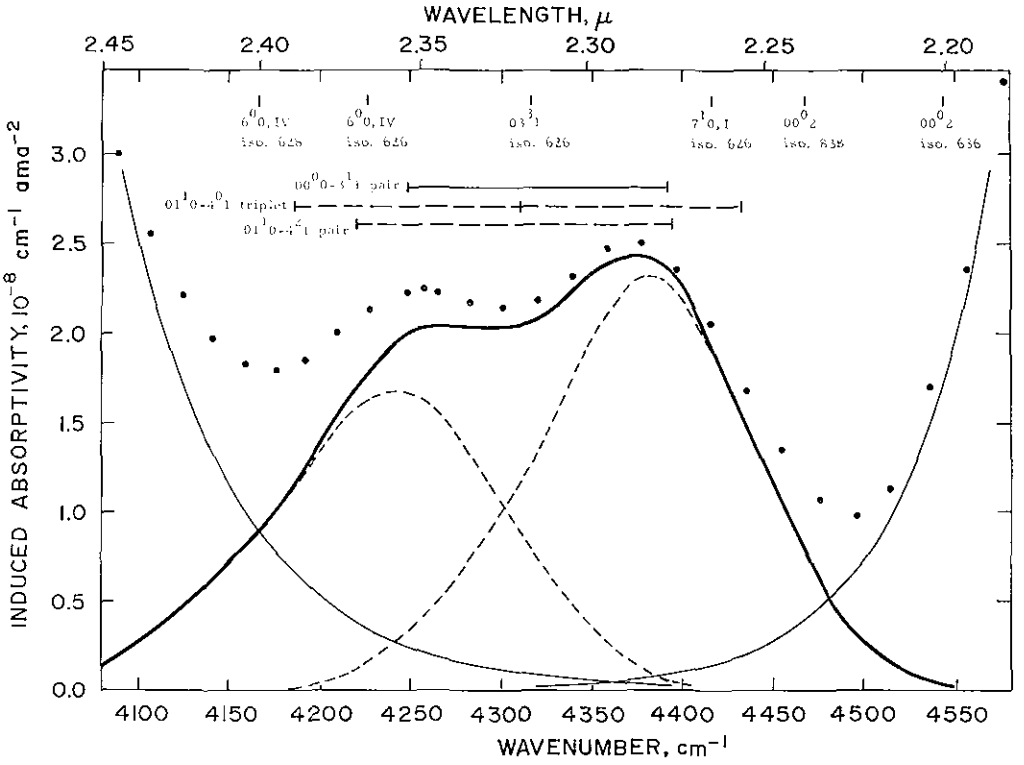

Fig. 10. Absorptivity vs. wavelength in the 2.3μ region. The dots are observed values. The light solid curves are estimated far wings of the transitions $00^0 0$-$2^0 1, II$ at 3715 cm^{-1} and $00^0 0$-$4^0 1, I$ at 4853 cm^{-1}; the heavy solid curve is the absorption due to the new lines, after subtracting these wings. The dashed curves show a decomposition into the two members of the Fermi pair. At top are the positions of other levels in this region; immediately below are the positions of the $3^1 1$ pair (identified with the new absorption) and the "not" triplet and pair which are related to it.

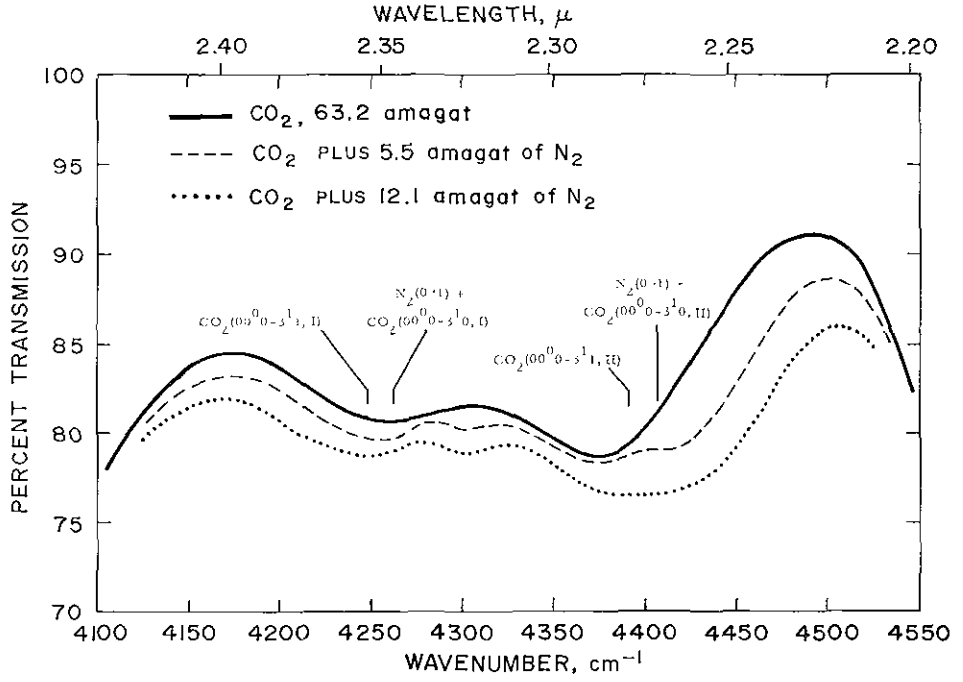

Fig. 11. Results of adding N_2 to CO_2. Absorption is downward. The solid curve is based on the absorptivities shown in Figure 10; the other curves are each the result of averaging three spectra, with the indicated amounts of N_2. In the mixtures, the CO_2 density had dropped slightly, so their results are normalized to 63.2 amagat of CO_2.

These are rejected because of the density dependence of the observed bands. Referring to Table 9 (Appendix A), the only density-inducible candidates near the observed location are transitions from ground to $6^0 0, IV$ at 4225 cm^{-1} in species 626 and to $00^0 2$ at 4467 cm^{-1} in 838. Not only do these transitions fail to give the observed spacing, but their strengths are expected to be several orders of magnitude smaller than the observed bands, on the basis of intensity arguments given by Stull, Wyatt, & Plass (1963) in the case of the $6^0 0, IV$, and on the basis of species 838's abundance of only 4.5×10^{-8} is the case of the $00^0 2$. The induced hot bands representing transitions from the $01^1 0$ level to the $4^0 1$ triplet and $4^2 1$ pair levels are discussed in section V. B.

When N_2 was added to CO_2 at high density, additional absorptions were seen. These are attributed to simultaneous transitions in which the N_2 goes from ground to the first vibrational level at 2330.7 cm^{-1} and the CO_2 goes from ground to the $3^1 0$ pair at 1932.5 and 2076.9 cm^{-1}. Because the N_2 0→1 transition lies near the $00^0 1$ level at 2349.1 cm^{-1} in CO_2, the simultaneous transitions (at 4236.2 and 4507.6 cm^{-1}) lie close to the induced $3^1 1$ pair in CO_2 discussed above, and cannot be separated from them. Figure 11 shows the effect of two admixtures of N_2. While the additional absorption appears to be proportional to the amount of N_2 as expected, the positions of the strongest additional absorptions do not coincide with the predicted positions. This may be

due to the P and R branches (which are more prominent in simultaneous transitions than in self-induced transitions), or to frequency shifts of the sort noted by Vu (1960) for induced transitions in mixtures. Some of the additional absorption is because the N_2 quadrupole moment increases the strength of the $3^1 1$ pair in CO_2.

2. Other Induced Absorption Bands

The 3.3μ region in CO_2 has been observed over a sufficiently wide range of densities so that the observed optical thickness can readily be resolved into the sum of two components, as shown in Figure 12. The linear component is believed to result from allowed transitions: the strongly absorbing C-H stretch near 3000 cm^{-1} in methane and other hydrocarbons, usually present as a few parts per million; and allowed $00^0 0$-$01^1 1$ transitions in the asymmetric CO_2 species 627 and 628, at 2993 and 2984 cm^{-1}. The square-law component is from the $00^0 0$-$01^1 1$ induced transition at 3004.0 cm^{-1} and gives an induced absorptivity of $(8.2 \pm 1.4) \times 10^{-7}$ cm^{-1} ama^{-2} at the band center. With a half-width of 75 ± 10 cm^{-1}, the band's induced strength is $(6.2 \pm 1.3) \times 10^{-5}$ cm^{-2} ama^{-2}.

Evidence for an induced absorption has been seen at 2.14μ, a region which is dominated by the wing of the allowed $4^0 1, I$ (centered at 4854 cm^{-1}). Its extent has been estimated by comparing the observed signal with the interpolated wing profile at various densities. Figure 13 shows

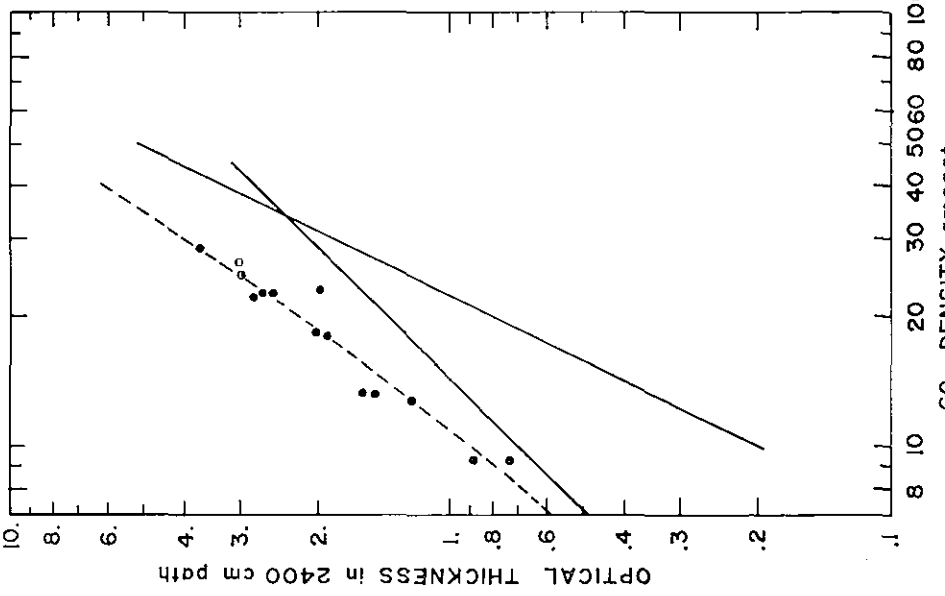

Fig. 12. Optical depth versus density at 3.3μ is indicated by •, with a dashed curve showing the two-parameter least-squares fit. The separate linear and square-law components are shown in solid lines.

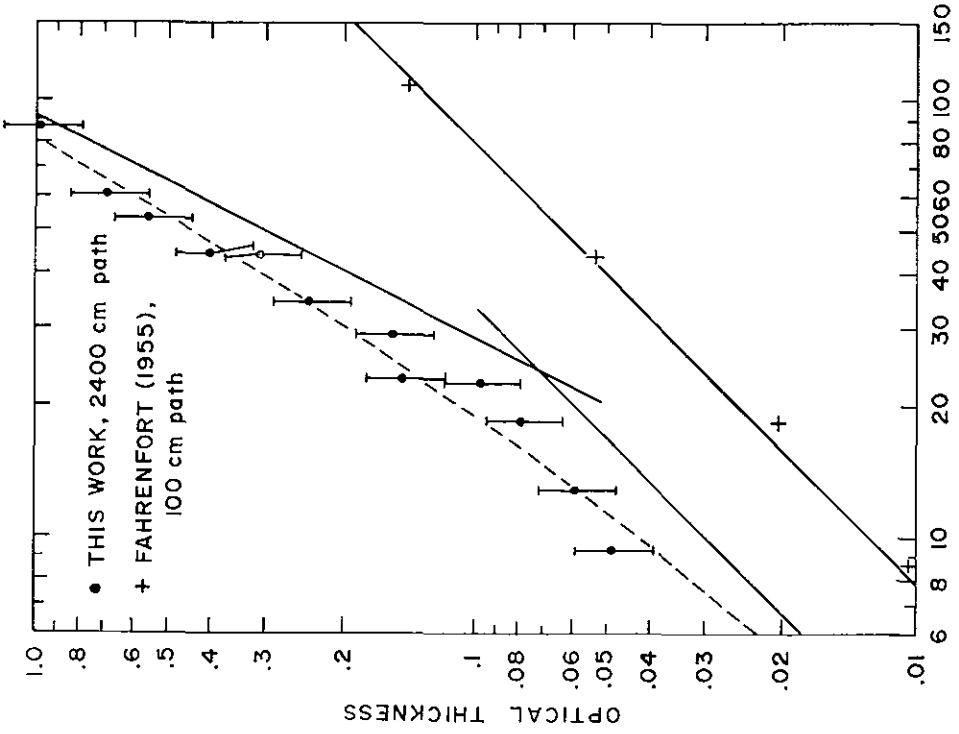

Fig. 13. Density dependence of the broad absorption found near 4660 cm^{-1} in this work, compared to the narrower absorption found at 4640 cm^{-1} by Fahrenfort. Both are relative to the $00^0 0\text{-}4^0 1, I$ far wing. Path lengths and resolutions are different, so that the results *cannot be compared in magnitude.* Fitted linear and square-law slopes are shown; for data in the present study, the dashed curve is their sum.

the resulting optical thickness versus density. As was the case in the 3.3μ region, the function can be expressed as the sum of linear and square-law components. The former is attributed to allowed $00^0 0\text{-}00^0 2$ transitions in species 627 and 628 (at 4655.2 and 4639.5 cm^{-1}); the latter is attributed to induction of the same transition, normally forbidden in species 626, at 4673.3 cm^{-1}. Because of the absorption's position on the steep slope of a wing and because of the moderate resolution, it was not possible to separate the three bands or to measure the half-width. However, the latter may be approximated by the 75 ± 15 cm^{-1} of the $00^0 0\text{-}00^0 1$ transition, giving an induced strength of the $00^0 0\text{-}00^0 2$ transition in isotopic species 626 as $(3.8 \pm 1.1) \times 10^{-6} cm^{-2} ama^{-2}$.

3. Windows at Longer Wavelengths

Optical thickness has been measured as a function of density and wavelength in the three windows centered at 11.2, 10.0, and 8.75μ. In each, the optical thickness is proportional to density squared, as expected from the fact that the windows are formed by the far wings of nearby allowed lines. The induced absorptivities at the centers of the windows have been found to be 1.5×10^{-6}, 7×10^{-7}, and 5×10^{-7} cm^{-1} ama^{-2}, respectively. Values at other wavelengths are shown in Figure 14. Errors are about ±20%.

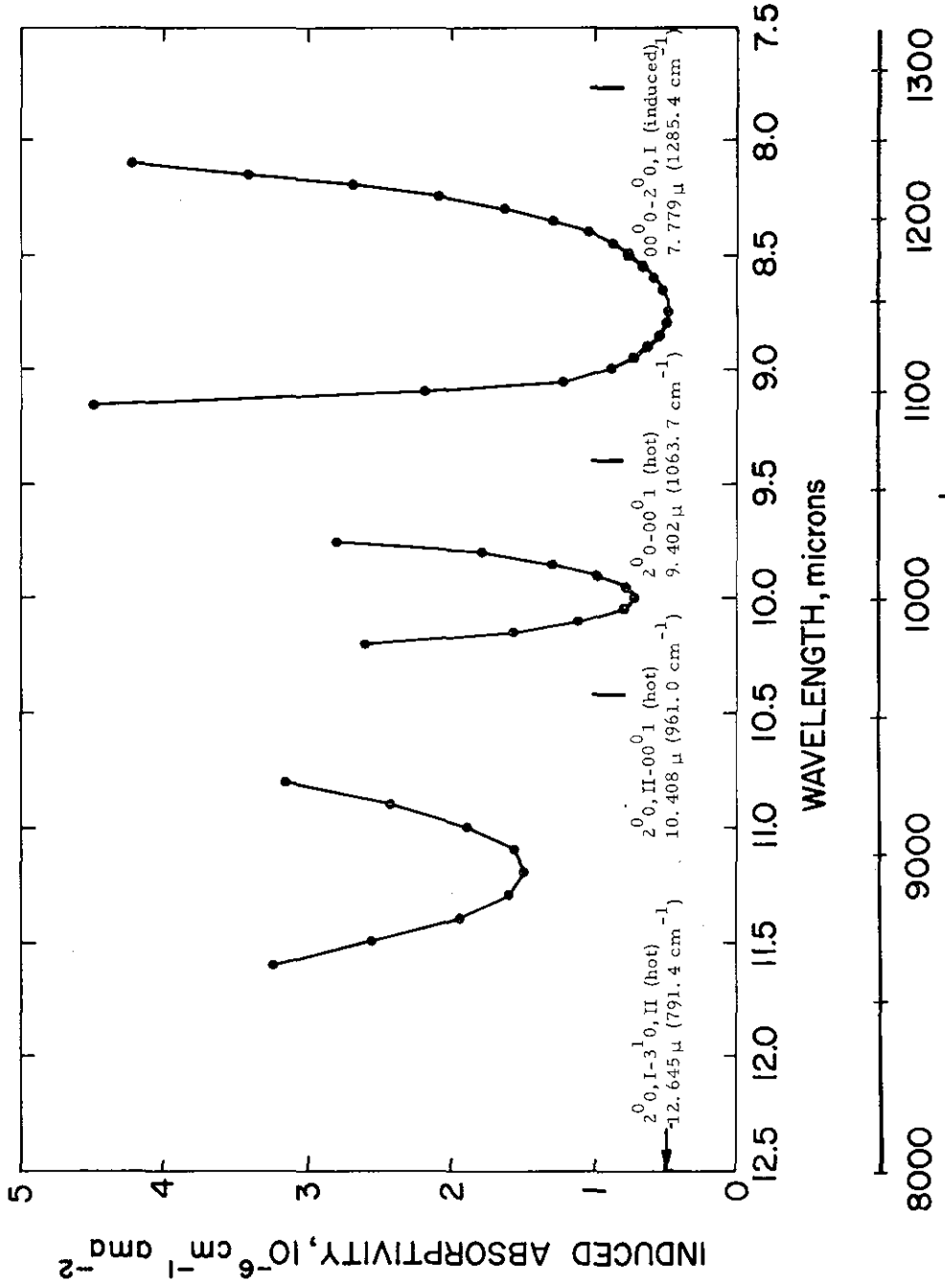

Fig. 14. Induced absorptivity in CO_2 in three windows centered at 11.2, 10.0, and 8.75μ. The contours are formed by the overlapping wings of allowed strong absorptions, some of whose positions are indicated.

C. DISCUSSION OF PREVIOUS INVESTIGATIONS

1. 2.3μ Region

No previous investigations have found absorption in this region. The cell at Pennsylvania State University has not yet been used at the pressures that would give it sensitivity for induced lines close to that in the present work; the cell at Ames, with less than one-sixth the sensitivity, has been used primarily in the photographic infrared. Burch (1971) has not recognized any absorptions in the 2.3μ region; it appeared transparent in Burch, Gryvnak, & Patty (1964 and 1968), using a cell with induced sensitivity about $2\frac{1}{2}$% of that in the present study.

With respect to the simultaneous transitions with N_2, it may be noted that Fahrenfort (1955) observed several other bands due to simultaneous excitation of the $0 \rightarrow 1$ transition in N_2, O_2, and H_2 and the $00^00\text{-}01^10$ or $00^00\text{-}00^01$ transitions in CO_2.

2. Other Induced Absorption Bands

Fahrenfort (1955) observed absorption in the 3.3μ region; though he attributed it entirely to the induced $00^00\text{-}01^11$ transition in CO_2, Gaizauskas (1955) has shown that the results were contaminated by hydrocarbon impurities. With only a few data points over a 100 cm path length, Fahrenfort's results cannot be analyzed to separate the allowed impurity transitions from the induced CO_2 transitions.

Fahrenfort also claimed to have observed the induced $00^0 2$ at 4640 cm^{-1}, but his attribution appears to be in error, for three reasons. First, the location is in error by more than three times any of his other wavenumber errors; second, the branch structure which he observed at low pressures argues for an allowed band; third, the absorption's dependence on density is not square-law. Though Fahrenfort believed it to be square-law, he did not allow for the absorption's lying on a far wing with density-squared absorption; when his results are plotted with respect to that wing, as in Figure 13, the density dependence is linear. It is likely that Fahrenfort observed the allowed $00^0 0$-$00^0 2$ transition in species 628 at 4639.5 cm^{-1}.

A number of other induced bands have been observed previously:

a) The $2^0 0$ pair (1285.4 and 1388.2 cm^{-1}) was first observed by Welsh, Crawford, & Locke (1949). The most recent of several measurements of their strength is by Burch, Gryvnak, & Pembrook (1970), giving a total of $(4.52 \pm 0.36) \times 10^{-3} cm^{-2} ama^{-2}$.

b) Transitions from ground to $4^0 0$, II and $4^0 0$, III at 2670.9 and 2797.0 cm^{-1}, have been observed by Fahrenfort (1955) and by Gryvnak, Patty, Burch, & Miller (1966), but with no estimates of strength.

c) Burch, Gryvnak, & Patty (1968) have observed shallow absorptions attributed to the induced transitions from ground to $6^0 0$, II and $6^0 0$, III at 3942.5 and 4064.2 cm^{-1}.

3. Windows at Longer Wavelengths

Burch, Gryvnak, Singleton, France, & Williams (1962) have observed a maximum of 10% absorption in the center of the 11.2μ window and 8% in the 10μ window, including the effects of weak allowed lines; Burch, Gryvnak, & Pembrook (1970) saw a maximum of 14% absorption in the center of the 8.7μ window. There was not enough data to permit calculating the form of pressure dependence or the absorptivity. In another window, Burch, Gryvnak, & Pembrook (1970) analyzed the region between 5.4 and 6.5μ, obtaining curves for the linear and square-law dependence of absorptivity on density. The latter reaches a minimum value of about 4×10^{-8} cm^{-1} ama^{-2} at 5.6μ.

D. DETAILS OF DATA REDUCTION

At all wavelengths (obtained as in section III. C), observed pressures were converted to densities using the data of Michels & Michels (1936)*, and the CO_2 spectra were corrected for source and instrumental variations with wavelength by dividing by the N_2 reference spectrum.

Thereafter, specific procedures most appropriate to each wavelength region were used to find absorptivities.

---

* Later confirmed by MacCormack & Schneider (1950).

1. 2.3μ Region

In this region, the spectra fell into three classes, one of which was not normalized. After normalization, the dependence of optical thickness on density was analyzed at a number of wavelengths to determine absorptivities. The curve of absorptivity versus wavenumber was corrected for the far wings of allowed lines, and then numerically integrated to get total induced strength.

The three classes of spectra are:

a) Those with long equilibration times (see section III. B. 1). These had reliable absolute signal levels, as verified by constancy in nonabsorbing windows.

b) Those with short equilibration times at densities from 28. 8 to 95. 1 amagat. In these, preliminary analysis disclosed shifts in overall signal level. The transmission minima at wavelengths B and D (refer to Figure 15) are both visible.

c) Those with short equilibration times at densities from 9. 3 to 22. 7 amagat. In these, only the minimum at wavelength B was visible. Absorption at wavelength E was less than 1%, so that the extrapolated peak could be used as a reference level.

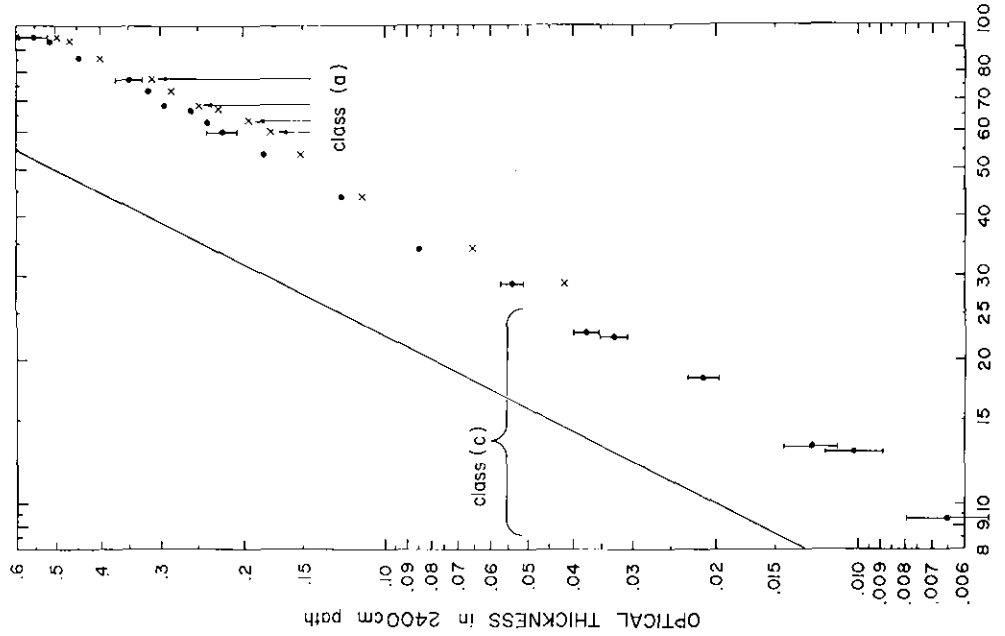

Fig. 16. Optical thickness versus density near 2.3μ. The experimental values at transmission minima B and D in Figure 15 are indicated by x and •, respectively. Points not marked are in class (b). Sample error bars are as discussed in section VII.B.

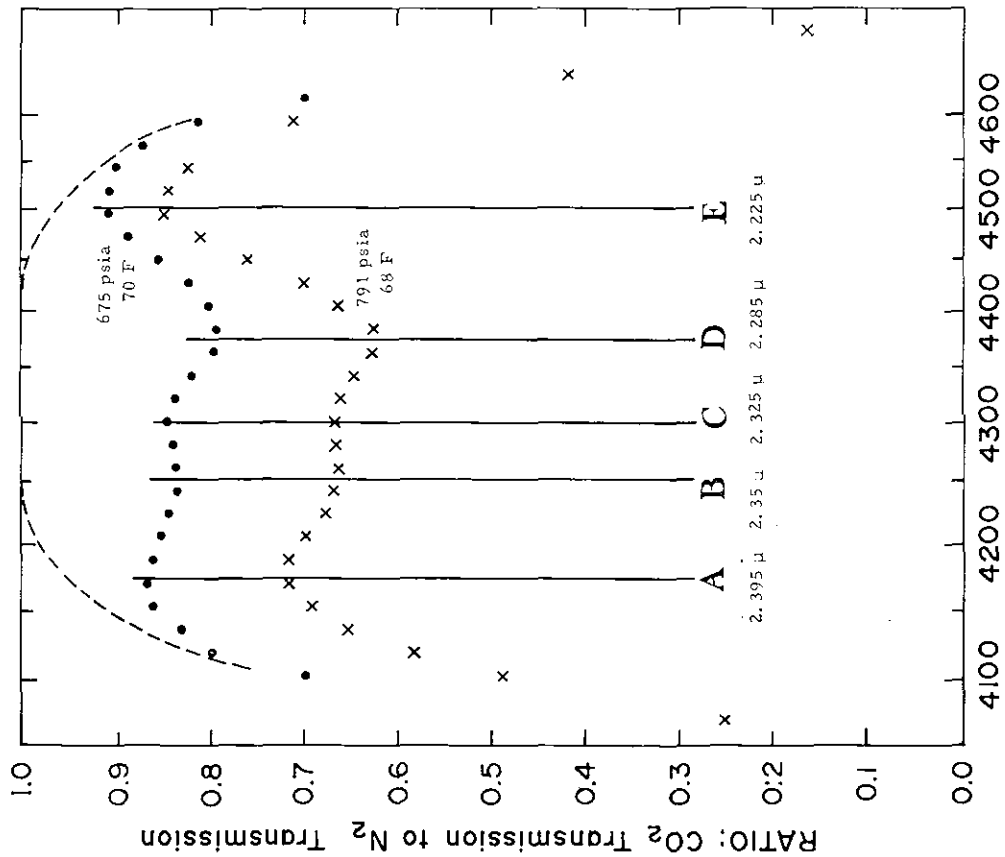

Fig. 15. Examples of unreduced data at two pressures of CO_2. The dashed lines show the approximate far wings of nearby strong allowed transitions (at 675 psia), as they might be seen if there were no absorption due to the $00^0 0\text{-}3^1 1$ pair. The transmission maxima and minima referred to in the text are labeled A through E.

Normalizing procedure was to determine, for the spectra in class (a), absorptivities a and e at wavelengths A and E by a least-squares fit of optical thickness versus density squared. For each spectrum in class (b), a correction factor was taken as the average difference between predicted and observed optical thickness at A and E.*

The class (c) spectra were used as a check: if the correction process were wrong, points from the three classes would not lie on a single straight line of optical thickness versus density squared. Figure 16 shows that the fit is satisfactory.†

The far wings of the allowed transition $00^0 0\text{-}2^0 1, \mathrm{II}$ at 2.69μ (3714.8 cm^{-1}) and $00^0 0\text{-}4^0 1, \mathrm{I}$ at 2.09μ (4853.6 cm^{-1}) extend into the 2.3μ region. Their absorptivities are approximated by $\tau/L = a\rho^2 e^{-b\Delta\nu}$, where a and b are constants, and $\Delta\nu$ is the distance from the line center (Birnbaum, 1971). Exponentials were fitted to the observations

---

*For example, corrected optical thickness at 2.285μ (the minimum marked D in Figure 18) is $D_j' = D_j + (a\rho_j^2 - A_j + e\rho_j^2 - E_j)/2$ at density ρ_j, where the unprimed capitals are uncorrected observations.

† A least-squares fit at wavelength D gives an absorptivity of $(2.499 \pm 0.059) \times 10^{-8}$ cm^{-1} ama^{-2} for classes (a), (b), and (c), and $(2.498 \pm 0.101) \times 10^{-8}$ cm^{-1} ama^{-2} for classes (a) and (b) alone. The errors here include only formal statistical error, and have not allowed for others (see section VII. B).

near 4100 cm^{-1} and near 4550 cm^{-1}, extrapolated as shown in Figure 10, and subtracted to obtain absorptivities due to the induced transitions alone. Separation of the induced pair into two overlapping components was estimated in several trials, using as criteria smoothness and symmetry of the individual curves.

The spectra taken with added N_2 all had long equilibration times, so that normalization was not required.

2. Other Induced Absorption Bands

Observations in the 3.3μ region were at low enough densities so that the signal at the band center could be compared with the black-body curve, interpolated between nearby windows; errors in individual points are estimated to be ±20%. In the 2.14μ region, the interpolated wing of the $00^00\text{-}4^01, I$ was used as reference.

3. Windows at Longer Wavelengths

In each window, the logarithm of the signal at the most transparent point was plotted with respect to density squared, and a least-squares fit was obtained. Absorptivities for the other points were based on the logarithms of the amplitude ratios between the off-peak wavelengths and the central peak.

V. THEORETICAL INTERPRETATION

Observations of the strengths of absorption bands can be used to determine ratios in a progression of overtone or combination bands, which may be useful in predicting the strength of transitions unobservable in the laboratory. They permit estimates of the matrix elements of certain molecular parameters, and can indicate the relative strength of matrix elements within Fermi groups.

A. RELATIVE INTENSITIES

Using the constants in Table 8 and formulas (A4) and (A5), the unperturbed levels are calculated to be:

$$G^{o}(11^{1}1) = 4312.1978 \text{ cm}^{-1} \text{ and } G^{o}(03^{1}1) = 4326.1440 \text{ cm}^{-1},$$

$$\text{with} \quad W_{AB} = 71.1163 \text{ cm}^{-1}.$$

Since $\delta = 13.9462$, formula (A1) gives $\Delta = 142.9147$, making the perturbed levels 4247.7135 and 4390.6282. By use of (A3), $a^2 = 0.5488$, $b^2 = 0.4512$, and $a = 0.7408$, $b = 0.6717$.

The observed strength ratio can be used to determine the ratio of the unperturbed matrix elements. The induced strength of each line is

*Table 8 and formulas (A1) through (A5) are in Appendix A.

$$K' = \int \kappa'(\nu)\, d\nu = 2(8\pi^3 N'\nu/3hc) \left| \int \psi_o \mu \psi' \, d\tau \right|^2 \qquad (1)$$

where N' is the number of molecules involved in collisions, μ is the induced dipole moment, ψ_o is the ground state, and ψ' is the mixture as defined in (A2). The initial 2 allows for the degeneracy in ℓ.

For brevity, define $A = \int \psi_o \mu \psi^o_{11^1_1} d\tau$, and $B = \int \psi_o \mu \psi^o_{03^1_1} d\tau$.

This gives $K'_{4391}/K'_{4248} = 4391\,(bA + aB)^2/4248\,(aA - bB)^2$. Setting $R = B/A$ and $r = 0.967K'_{4391}/K'_{4248}$, this simplifies to:

$\sqrt{r} = (b + aR)/(a - bR)$, giving $R = (a\sqrt{r} - b)/(a + b\sqrt{r})$.

Experimentally (section IV. D. 1), $r = 1.35 \pm 0.19$. From this, $R = 0.124^{+0.033}_{-0.038}$ for the ratio of 03^1_1 to 11^1_1*, indicating that the 11^1_1 matrix element is stronger by $8.1^{+3.5}_{-1.7}$.

We have calculated the comparable figures for the 2^0_0 Fermi Raman pair on the basis of energy levels given by Gordon & McCubbin (1966) and by Burch, Gryvnak, & Pembrook (1970). The ratio of 02^0_0 to 10^0_0 is $0.121^{+0.019}_{-0.021}$, so that the 10^0_0 matrix element is stronger by $8.26^{+1.71}_{-1.12}$.

---

*The new notation is not required, of course, when referring to the unperturbed levels, as they are derived unambiguously from the vibrational constants and quantum numbers.

It may be noted that the earlier literature gives markedly higher values for the ratio of unperturbed $10^0 0$ to $02^0 0$ matrix elements. These range from 14 (Stoicheff, 1950), based on the Raman effect, to 29 (Fahrenfort, 1955), based on pressure-induced infrared absorption. These results are in error: in effect, they say that if the upper perturbed line is somewhat stronger, then the upper unperturbed level is much stronger. This result was reasonable at the time, as the $10^0 0$ unperturbed level was believed to lie above the $02^0 0$. The $10^0 0$ matrix element was expected to be larger, as it contains a first derivative of the polarizability, while the $02^0 0$ contains a second derivative. However, Amat & Pimbert (1965) showed that the $02^0 0$ level actually has the higher energy of the two unperturbed levels, so Stoicheff's and Fahrenfort's results now imply that it is the stronger, which appears unlikely.

A resolution of this question lies in the fact that there are two solutions for R, corresponding to the two signs for $\sqrt{r}$ (or, in equation (A3), for a and b, whose phase is arbitrary). Thus, the data of Burch et al. (1970) can either indicate that the upper $02^0 0$ level is 23 times stronger -- in good agreement with Fahrenfort -- or that there is a crossing-over of intensities, and the lower $10^0 0$ level is 8.26 times stronger.

The second of these alternatives is undoubtedly correct. Appendix C demonstrates that the matrix element of the atomic polarizability derivative is, as expected, larger for the 10^00 level, and indicates this will also be true for the electronic polarizability.

However, the best evidence comes from examining the spectra of other triatomic molecules in which no Fermi resonance occurs between the 100 and 020 states*, so that the observed levels and strengths are unperturbed. According to Herzberg (1945), the 000-100 transition is stronger in CS_2, N_2O, HCN, H_2O, and NO_2; there are no counterexamples. Of these, CS_2 is the most significant, as its structure, including valence electrons, is closest to that of CO_2.

Returning to the 3^11 pair, the quantum numbers, matrix elements, and polarizability derivatives are related to those of the 2^00 Fermi Raman pair by an additional operation each in ν_2 and ν_3. It is therefore clear that, as before, the transition to the unperturbed term with fewer quantum numbers (11^11) is the stronger. Again looking at other molecules for confirmation, the 000-111 transition is seen in H_2O, but not the 000-031. Since the lower unperturbed term and the upper perturbed term are stronger, there is again a crossing-over of strengths.

---

*The superscript for ℓ is omitted, as some of the examples do not have the degeneracy.

B. POLARIZABILITY DERIVATIVES

The total strength for the pair is given from (1) by:

$$K'_T \equiv K'_{4391} + K'_{4248} \tag{3}$$

$$= 2(8\pi^3 N'/3hc)\left\{4391\left|\int \psi_o \mu \psi_{4391}\, d\tau\right|^2 + 4248\left|\int \psi_o \mu \psi_{4248}\, d\tau\right|^2\right\}$$

Replacing ψ_{4391} and ψ_{4248} by the mixed expressions used previously, and employing A and B as the matrix elements as before, we can obtain a form with a main term based on the average wavenumber $\bar{\nu}$, and smaller terms which will indicate that the result does not depend strongly on other quantities.

$$K'_T = (16\pi^3 N'\bar{\nu}/3hc)\left[A^2 + B^2 + (2\Delta/\bar{\nu})abAB - (\delta/2\bar{\nu})(A^2 - B^2)\right] \tag{4}$$

$$K'_T = 16\pi^3 N'\bar{\nu} A^2 [1. + .0159 + .0042 - .0016]/3hc$$

In the last expression, values for a, b, and R = B/A have been inserted, but the individual terms have been left unsummed in order to show their relative size. The quantity in brackets is 1.018, and varies by less than ±1% when R is varied from 6.4 to 11.6, as found earlier.

As before, $A = \int \psi_o \mu \psi_{11^1_1}\, d\tau$, where $\mu = E\alpha$, the product of the perturbing field and the polarizability. Expanding the latter as in equation (D1), the only significant term will be $\frac{\partial^3 \alpha}{\partial\xi_1 \partial\xi_2 \partial\xi_3}\xi_1\xi_2\xi_3$;

Appendix D explains why other terms, representing mechanical anharmonicity, are not significant.

The induced field E results from the quadrupole moment of nearby CO_2 molecules, with r.m.s. value at distance r of $E = Q/r^4$.

Equation (4) now becomes

$$K'_T = \frac{16\pi^3\bar{\nu}}{3hc} \frac{N'Q^2}{r^8} 1.018 \left(\frac{\partial^3 \alpha}{\partial\xi_1 \partial\xi_2 \partial\xi_3} \right)^2 \left\langle \psi_o \xi_1^1 \xi_2^1 \xi_3^1 \psi_{11}^{11} \right\rangle^2 \qquad (5)$$

To obtain the average value of $N' Q^2/r^8$, a molecular potential is required. The 6-12 potential, originally proposed by Mie (1903) and usually called Lennard-Jones, has proved to be a very good approximation for polyatomic molecules, according to Münster (1965).

With CO_2, this takes the following form:

$$U = 4u \left[(r_o/r)^{12} - (r_o/r)^6 \right] \qquad (6)$$

where u is 25.6×10^{-15}, the minimum value of U in ergs, and $r = 4.57 \times 10^{-8}$ cm is the radius at which U = 0.

The number of molecules lying in a spherical shell dr around a given molecule is $(N/V_o)\, e^{-(\nu/kT)}\, 4\pi r^2\, dr$; when multiplied by (N/V_o), we get the number of pairs per cm^3 interacting at distance r. The total interaction is thus

$$\left(\overline{\frac{N' Q^2}{r^8}}\right) = 4\pi Q^2 \left(\frac{N}{V_o}\right)^2 \int_0^\infty r^{-6}\, e^{-(\nu/kT)}\, dr \qquad (7)$$

where the integral, evaluated numerically, is $1.755 \times 10^{36}\ cm^{-5}$. Since $(N/V_o) = 2.69 \times 10^{19}$ molecules cm^{-3} ama^{-1}, and dimensions of Q^2 are gm cm^7 sec^{-2}, those of (7) are pairs gm cm^{-4} sec^{-2} ama^{-2}.

Combining equations (5) and (7), we have

$$\frac{\partial^3 \alpha}{\partial \xi_1\, \partial \xi_2\, \partial \xi_3} \equiv \alpha'''_{123} = \frac{(6K'_T hc/1.018\bar{\nu}\ 1.755 \times 10^{36})^{1/2}}{4\pi^2 Q(N/V_o)\, N_1\, N_2\, N_3} \qquad (8)$$

where the matrix element in (5) has been evaluated according to Appendix E.*

---

*We have used the customary approximation that the eigenfunctions for unperturbed states are purely those of harmonic oscillators. A brief discussion of anharmonicity appears in Appendix D; details of the mixing of eigenfunctions (even for the 00^00 state) appear in Statz, Tang, & Koster (1966).

The induced strength of $(6.2 \pm 0.9) \times 10^{-6}$ cm^{-2} ama^{-2} found in section IV. B. 1 is a total which includes not only the induced transitions from ground to the $3^1 1$ pair, but also any associated induced hot bands with the same change in vibrational quantum numbers. The only ones whose strengths are not so small as to be neglected are from the lowest excited level (667 cm^{-1}): transitions from $01^1 0$ to the $4^2 1$ pair should have a total strength of 0.43×10^{-6} cm^{-2} ama^{-2}, and those from $01^1 0$ to the triad $4^0 1$ of 0.22×10^{-6} cm^{-2} ama^{-2}. These are based on the Boltzmann population of the $01^1 0$ level at room temperature, times the appropriate ratios of matrix elements.* Subtracting the "hot" bands, the remaining induced strength attributable to the $00^0 0$-$3^1 1$ pair alone is $K'_T = (5.55 \pm 0.8) \times 10^{-6}$ cm^{-2} ama^{-1}. Substituting this and the normalizations N_j and other constants (see Appendix A, section 6), we find $\alpha'''_{123} = 112 \pm 17$, dimensionless.

Other polarizability derivatives can be obtained similarly, using measurements of the strength of the $00^0 0$-$01^1 1$ and $00^0 0$-$00^0 2$ transitions from the present study for α''_{23} and α''_{33}; of the $00^0 0$-$2^0 0$ pair from Burch, Gryvnak, & Pembrook (1970) for α'_1 and α''_{22}; and of the $00^0 0$-$4^0 0$ and $00^0 0$-$6^0 0$ groups (dominated by the matrix elements from ground to the unperturbed $20^0 0$ and $30^0 0$ states) for α''_{11} and α'''_{111}, where we have analyzed the results of Fahrenfort (1955) and Burch,

---

* See Table 13 in Appendix E.

Gryvnak, & Patty (1968), respectively, to obtain rough estimates of these groups' induced strength.

Summarizing the results, we have the following r. m. s. values:

$\alpha_0 = 2.65 \times 10^{-25}$ cm^3 (Brand & Sparkman, 1960)

$\alpha_1' = 1.20 \times 10^{-15}$ cm^2. This result differs from Fahrenfort's (1955) value of 1.46×10^{-15} cm^2 not only through more accurate measurement of strength and correction for hot bands, but also through use of the proper ratio between members of the $2^0 0$ pair, as discussed in the preceding section.

$\alpha''_{11} = 0.54 \times 10^{-7}$ cm $\quad \alpha''_{22} = 2.8 \times 10^{-7}$ cm

$\alpha''_{33} = 1.3 \times 10^{-7}$ cm $\quad \alpha''_{23} = 1.7 \times 10^{-7}$ cm

$\alpha'''_{111} = 136.$ $\quad \alpha'''_{123} = 112.$

$\alpha''''_{2223} = 5.4 \times 10^{10}$ cm^{-1}

The other second and third derivatives are zero by symmetry, except for α'''_{122} and α'''_{133}, which correspond to transitions from ground to the unperturbed $12^0 0$ and $10^0 2$. The former cannot be calculated without observation of the $00^0 0 - 4^0 01$ transition at 2548 cm^{-1}, which is completely hidden in the wing of the very strong $00^0 0 - 00^0 1$ transition. The latter is the dominant member of the $2^0 2$ pair at 5915 and 6017 cm^{-1}; it may be possible to observe them with equipment of

better resolution than that in the present study. Of course, all induced lines are expected to be active in the Raman effect, and should be visible with laser excitation.

C. INTENSITY RATIOS BETWEEN GROUPS

The following table is a summary of the total strength for a number of Fermi groups, tabulated in series according to the value of v_3. The strengths of allowed transitions are taken from Benedict & Wattson (1969); those of induced transitions are as in sections IV. B. 1, IV. B. 2, and IV. C. 2 -- except for transitions to the $4^0 0$ and $6^0 0$ groups, where we have analyzed the results of Fahrenfort (1955) and Burch, Gryvnak, & Patty (1968) to estimate the induced strengths.

TABLE 3: GROUP STRENGTHS

Max. value of v_2	Allowed Transitions units: cm^{-2} ama^{-1}				Induced Transitions units: cm^{-2} ama^{-2}	
	$v_3 = 0$	$v_3 = 1$	$v_3 = 2$	$v_3 = 3$	$v_3 = 0$	$v_3 = 1$
0		0.24×10^{4}		0.40×10^{-1}		
1	0.20×10^{3}		0.45×10^{-3}			0.6×10^{-4}
2		0.73×10^{2}		0.57×10^{-2}	0.45×10^{-2}	
3	0.71×10^{-1}		0.82×10^{-4}			0.5×10^{-5}
4		0.10×10^{1}		0.11×10^{-3}*	0.14×10^{-5}	
5	0.46×10^{-2}		0.64×10^{-5}			
6		0.26×10^{-1}			0.7×10^{-6}	
7	0.54×10^{-4}					
8		0.46×10^{-3}				
r.m.s. ratio	0.005	0.021	0.12	0.05	0.012	0.08

*From Burch, Gryvnak, & Patty (1965B); value uncertain.

The last line in the table shows, for each series, the strength ratio from one member to the next, based on a least-squares fit to the logarithms of the strengths. While accuracy is not great in such short series, it does appear that the series ratios for allowed lines given by Stull, Wyatt, & Plass (1963) require modification*. Also, the ratio for induced series is not the same value of v_3 (see Herzberg, Fig. 80, p. 264, 1945). Instead, it is interesting to note that, if the induced series are placed to follow the allowed series with the same v_3, a monotonically increasing sequence of ratios occurs (except for the questionable value for $v_3 = 3$). Additional measurements of intensities for both allowed and induced bands will be necessary to verify such a sequence.

---

*They give the decrease in total group strength as 0.001 for the second column in Table 3 (transitions from ground to $01^{1}1$, $3^{1}0$, $5^{1}0$, etc.) and 0.04 for the third columns (ground to $00^{0}1$, $2^{0}1$, $4^{0}1$, etc.).

D. LONGER-WAVE WINDOWS: RELATION TO LINE SHAPE

The absorptivities measured herein for the longer-wave windows permit testing the hypothesis that collision-broadened far wing shapes become increasingly sub-Lorentzian at increasing wavelength. This hypothesis was based on only three experimental cases*.

The measured window absorptivities are formed by overlapping wings of rotational lines from two or more vibrational transitions. It is therefore not possible, within the scope of the present study, to

*Burch, Gryvnak, Patty, & Bartky (1968) observed the extreme wings of CO_2 lines in three spectral regions near 2400, 3800, and 7000 cm^{-1}, with pressures to 14.6 atm. Computer analysis was used to separate the effects of line centers at different wavelengths, in order to find the average contours for individual rotational lines. When normalized at the line centers, absorptivities in the wings (10 to 100 cm^{-1} from the centers) were sub-Lorentzian by 0.1, 0.2, and 0.6, respectively. The authors say, "it is certainly significant that [beyond 10 cm^{-1} from line center] the curves occur from bottom to top in the order of increasing wavenumber. This phenomenon may be based on the ratio of the period of the electromagnetic waves to the time the colliding molecules are within a certain distance." They suggest the need for absorption measurements near 875 cm^{-1} (11.4μ) to verify the expectation of even further deviation below Lorentz.

isolate the individual contours. Instead, the observed absorptivities at the centers of the 11.2μ and 10.0μ windows are compared to those predicted under three different assumptions:

a) Deviation from the Lorentz contour is inversely proportional to wavenumber, as implied by the ratio of period to collision time.

b) Deviation is proportional to the square root of wavenumber. This assumption provides an intermediate case.

c) The null hypothesis of no regular dependence on wavenumber. An average of the values in Burch et al. is used.

These cases correspond to values of -1, -1/2, and 0 for the exponent in

$$\ln [k(\nu)/k(L)] = a_n \nu^n \qquad \text{(at a given } \Delta\nu \text{ from line center)}$$

where $k(\nu)$ is the actual contour, $k(L)$ is the Lorentz contour, and a_n are constants fitted to the points in Burch et al.

As a first-order approximation to the overlap of rotational lines, the shape of the experimental curve near 3800 cm^{-1} in Burch et al. is used for the dependence on $\Delta\nu$; its values are corrected for the strength of each band contributing to the window contours. Table 4 gives the results, and appears to favor the null hypothesis, (c). This conclusion is used in synthesizing a spectrum beyond 19μ, in section VI. B. 3.

TABLE 4: PREDICTION VS. OBSERVATION

Wavelength	11.2μ	10.0μ
Wavenumber	895 cm^{-1}	1000 cm^{-1}
Number of contributing bands	4	3
Predicted absorptivity under (a)	0.3×10^{-7}	0.1×10^{-7}
Predicted absorptivity under (b)	0.5×10^{-6}	0.11×10^{-6}
Predicted absorptivity under (c)	0.11×10^{-5}	0.32×10^{-6}
Observed absorptivity	$(0.15\pm0.03)\times10^{-5}$	$(0.71\pm0.14)\times10^{-6}$

(absorptivity is collision-induced; units are cm^{-1} ama^{-2})

VI. APPLICATION TO THE ATMOSPHERE OF VENUS

A. BACKGROUND

A combination of earth-based studies and data from the Mariner and Venera spacecraft have established that the atmosphere of Venus contains large quantities of CO_2, some N_2 and inert gases, small quantities of H_2O, and traces of HCl, HF, and CO.

Disagreement still exists as to whether other ingredients than CO_2 are present below the clouds in significant quantities. The amount of water is of particular interest, as it bears on the proposal by Dole (1956) that the differences between the atmospheres of Venus and the earth result solely from the earth's greater distance from the sun. A quantitative analysis of the evolutionary processes involved (Rasool & deBergh, 1970) suggests a concentration of H_2O of 0.1% at the present epoch. Water has also played a significant role in attempts to explain Venus' high surface temperature, by contributing to the microwave and infrared opacity of model atmospheres.

Comparing the temperatures of the surface and the cloudtops, it is obvious that nearly 99% of the surface black-body radiative flux must be prevented from reaching the clouds by opacity in the lower atmosphere. To explain such an opacity, the wavelengths where absorptions are usually seen in the laboratory are of little concern, as the depth and density of Venus' lower atmosphere are so great that even

small absorptivities will completely block radiation at those wavelengths. Rather, the "windows" — wavelength regions in the CO_2 spectrum that are usually considered transparent — are important: when their widths are weighted by the black-body curve, they transmit far too much radiation to sustain the observed surface temperature of over 750K.

Though some investigators (Sagan, 1960; Pollack & Morrison, 1970; etc.) believed that water is necessary to close the windows in the CO_2 spectrum, another alternative was suggested by Thaddeus (1964). He pointed out that the integrated opacity of CO_2 is very large, and if only partly spread into the windows by pressures and temperatures beyond those reached in previous experiments, a massive dry CO_2 atmosphere could provide enough greenhouse effect to sustain the surface temperature. In the present study, partial closure of a number of windows has been found; this section will apply these results and those of other investigators to a model of the Venus atmosphere.

In order to compare the net upward radiative flux within the lower atmosphere of Venus to the flux emitted from the cloudtops, attention was directed to ten windows in the CO_2 spectrum. In these windows, allowed and induced absorptivities versus wavelength were combined with an atmospheric profile of density and temperature, to obtain radiative intensities versus wavelength, angle, and altitude. Total

flux was found by integrating over angle and wavelength, both with and without the effects of an opaque cloud.

B. PARAMETERS

1. Profile

The profile from Avduevsky, Marov,& Rozhdestvensky (1970) is used. It has a surface temperature of 768K, is essentially adiabatic, is extrapolated from measurements made by Venera 5 and 6, and appears to be confirmed by data transmitted down to the surface by Venera 7 (Marov, 1971). The profile was used from zero to 95 km altitude.

2. The Windows

There are ten spectral regions within which the opacity of CO_2 is sufficiently low so that, in a dry model atmosphere, these wavelengths could carry energy from the lower atmosphere to the clouds. The limits of the window regions, as listed in Table 5, are those wavelengths where the opacity has become sufficiently great so that no significant additional flux is transmitted. In general, the spectral regions other than the windows are filled with well-known absorptions of sufficient strength so that substantial opacity occurs above the clouds, implying that these non-window regions do not contribute to radiative transfer from the surface and lower atmosphere to the clouds.

TABLE 5: WINDOW LISTING

Name	Limits, μ	Name	Limits, μ
Long-wave	60.5 - 18.5	3.5μ	3.725 - 3.135
11.2μ	11.75 - 10.65	2.3μ	2.500 - 2.150
10.0μ	10.225 - 9.725	1.75μ	1.815 - 1.665
8.75μ	9.175 - 8.075	1.26μ	1.285 - 1.245
6.0μ	6.925 - 5.325	1.1μ	1.200 - 1.070

3. Absorptivities in the Long-Wave Window

If the region beyond 18.5μ were transparent, it would radiate 3.6% of the total energy emitted by a 768K black body. This is 3.1 times the total emission of a black body at Venus' cloudtop temperature of 251K. Substantial opacity must therefore be present in the Venus atmosphere in this spectral region; since previous analyses have not considered CO_2 to be opaque at those longer wavelengths, they found it necessary to invoke the presence of water vapor.

Though there is still a substantial gap between 20μ and 45μ in published CO_2 experimental work, there is enough evidence available to permit synthesizing an absorption spectrum in the longwave window in a conservative manner.

First, the pressure-induced rotational absorption of CO_2 has been measured by Ho, Birnbaum, & Rosenberg (1971) from 7 to 220 cm^{-1}

(1428 to 45μ), over a temperature range from 243K to 333K. Birnbaum(1971) discusses the wavenumber dependence of such absorptions, and shows that an eventual exponential decrease at larger wavenumbers is preceded by a more slowly varying transition region. We have therefore extrapolated the Ho et al. results with an exponential, assuming that 220 cm^{-1} is past the transition region. If this assumption is wrong, the true induced absorptivity will be greater than used herein. Ho et al. show a temperature dependence which decreases with increasing wavenumber, reaching $T^{-0.68}$ near 200 cm^{-1}. We have used this exponent throughout the region of extrapolation. If, in fact, the temperature dependence continues to decrease at higher wavenumbers, the true induced absorptivity will again be greater than used herein.

Second, the collision-induced wings of the strong 15μ bands will extend to longer wavelengths. While no far-wing measurements exist in this region, measurements of wing shape as far as 380 cm^{-1} from other band centers have been made by Burch, Gryvnak, Patty, & Bartky (1968). Their results in the 3800 cm^{-1} region (far wing of the 00^00-2^01, II transition) have been adjusted to the greater strength of the 00^00-01^10 transition, and are used from 19μ to 34μ (526 to 295 cm^{-1}), with an exponential decrease thereafter. This extrapolation becomes smaller than the extrapolation from Ho et al. beyond 30μ, so that its shape is not critical.

Third, long-wave hot bands provide substantial allowed absorptivity. A list of such transitions, with their allowed strengths, has been calculated by Benedict & Wattson (1969). We have taken 24 of these hot bands which have significant strength, and whose centers lie from 177 to 544 cm^{-1} (56.6 to 18.4μ), to synthesize allowed absorptivities versus wavelength. The strength of each hot band was distributed over the same contour (P, Q, and R branches) as that of the transition from ground with the same change in quantum numbers*, located at the proper wavenumber, and summed. Table 6 gives the resulting allowed absorptivities, and also gives the induced absorptivities (the sum of the induced rotational absorption in Ho et al. and the collision-induced far wings of the 15μ band).

The values in Table 6 apply only to 295K, and will vary rapidly with temperature, in proportion to the changing populations of the lower states. This variation is approximated by selecting the most strongly absorbing transition at each point in the spectrum (in most cases, one is clearly predominant), and multiplying its allowed absorptivity by the Boltzmann factor corresponding to that transition's lower state. The absorptivity $\kappa(T)$ at temperature T is related to that at 295K by:

$$\kappa(T) = \kappa(295) \exp[(1 - 295/T)h\nu c/295k] \qquad (8)$$

The correction is unity if the lower state is ground.

---

* For example, the $00^{0}1\text{-}4^{0}0$, II at 322 cm^{-1} has the same change in quantum numbers as the $00^{0}0\text{-}4^{0}1$, II transition at 4978 cm^{-1}.

TABLE 6: ABSORPTIVITIES, LONG-WAVE WINDOW

Wavelength, microns	Allowed Absorptivity*, $cm^{-1} ama^{-1} \times 10^{8}$	Induced Absorptivity*, $cm^{-1} ama^{-2} \times 10^{5}$
60.	0.080	6.29
59.	0.115	5.90
58.	0.155	5.51
57.	0.200	5.14
56.	0.240	4.78
55.	0.280	4.44
54.	0.310	4.11
53.	0.325	3.79
52.	0.310	3.49
51.	0.210	3.20
50.	0.110	2.92
49.	0.250	2.66
48.	0.320	2.41
47.	0.320	2.18
46.	0.290	1.96
45.	0.200	1.75
44.	0.070	1.56
43.	0.040	1.41
42.	0.025	1.24
41.	0.027	1.14
40.	0.030	0.961
39.	0.028	0.838
38.	0.036	0.727
37.	0.095	0.629
36.	0.230	0.549
35.	0.420	0.476
34.	0.900	0.414
33.	1.85	0.362
32.	2.00	0.319
31.	0.400	0.284
30.	2.20	0.256
29.	0.800	0.254
28.	0.180	0.258
27.	0.060	0.278
26.	0.260	0.342
25.	1.11	0.429
24.	4.20	0.620
23.	17.5	0.863
22.	43.	1.31
21.	170.	2.21
20.	950.	5.00
19.	4000.	18.0

* See Appendix B, part 2, for definitions.

Several other factors do not appear in the synthesized long-wave absorption spectrum.

a. The effect of temperature in changing P and R branch shapes is not included. This will have the effect of filling in the regions where the linear absorption is low.

b. Pressure-induced wings of hot bands are not included. These will cause an increase of a few percent at room temperature, but will contribute more strongly at higher temperatures.

c. Isotopic species other than 626 (the common $C^{12}O_2^{16}$) have not been considered, except for the $00^{\circ}1\text{-}4^{\circ}0, II$ line at 322 cm^{-1} mentioned above, which is shifted to 272 and 261 cm^{-1} in species 628 and 636, respectively.

The greatest uncertainty in the synthesized spectrum is in the region near 20μ. However, the values of allowed absorptivity agree closely from 19 to 22μ with results reported by Anding (1967) using more sophisticated methods; and if both allowed and induced absorptivities are applied to the experimental conditions of Burch, Gryvnak, Singleton, France, & Williams (1962), predicted opacities agree with their results at 19 and 20μ. It is therefore believed that the synthesized spectrum will provide a valid basis for analysis until completion of current experimental work between 20 and 40μ (M. J. D. Low, 1971).

4. Sources of Other Data

In the windows at 11.2, 10.0, and 8.75μ, allowed absorptivities were obtained from 18 hot bands in the compilation by Benedict & Wattson (1969), using the procedure outlined in section VI. B. 3 and the Boltzmann correction for temperature as in equation (8). They were supplemented by the allowed absorptivity given by Burch, Gryvnak, & Pembrook (1970) for the wing of the $2^0$0, I in isotopic species 628 from 8.1 to 8.25μ, with exponentially decreasing extrapolation beyond. Induced absorptivities were as measured in section IV. B. 3.

In the 6.0μ window, the data of Burch, Gryvnak, & Pembrook was analyzed in a series of simultaneous equations in order to provide both allowed and induced absorptivities.

In the 3.5μ window, the data of Gryvnak, Patty, Burch, & Miller (1966) and Burch, Gryvnak, & Patty (1968) provided allowed absorptivities. Induced absorptivities were obtained from the present study by normalizing observed spectral contours at high density to the induced term in the analysis of measurements of 3.3μ (section IV.B.2).

The 2.3μ window has already been discussed in detail. Induced absorptivities as in section IV. B. 1 were supplemented with allowed absorptivities near 2.15μ from Burch, Gryvnak, & Patty (1964).

The 1.26μ window has only allowed absorptivities, taken from Burch, Gryvnak, & Patty (1967). The 1.75μ and 1.1μ windows are taken as transparent over the wavelengths where neither the present study nor Burch, Gryvnak, & Patty (1965B) found any absorption.

Figures 17 and 18 show the allowed and induced absorptivities at 295K, as used to calculate radiation properties of Venus' atmosphere. As explained previously, the absorptivities in the unplotted regions between the windows are so much larger that they do not contribute to the flux in the lower atmosphere.

5. Clouds

Calculations were performed with and without the effect of opaque clouds. In the former case, altitudes of the cloud bottom and top are taken as 59 km and 65 km, based on Avduevsky, Marov, & Rozhdestvensky (1970). The corresponding temperatures are 278.3K and 251K. Cloud emissivity is taken as unity.

6. Limitations of the Model

a) Temperature variations with latitude, longitude, and time are not included. However, Thaddeus (1968) has shown that there will be less than 30K variation at the surface. This is a small enough fraction of the average surface temperature so that results can be based on that average.

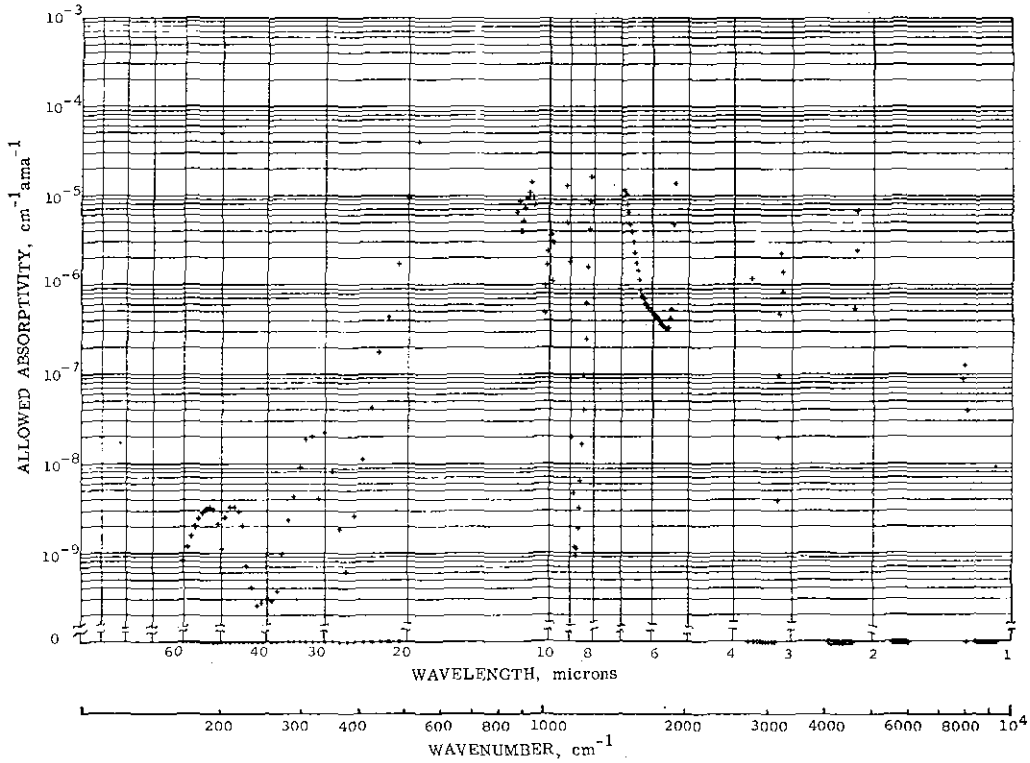

Fig. 17. Allowed absorptivity in the ten windows used to calculate radiative flux in the lower Venus atmosphere. Between the windows, absorptivity is large. Crosses denote the values used in basic calculations; the dots from 60_u to 19_u were used in calculating the significance of omitting the long-wave synthetic spectrum.

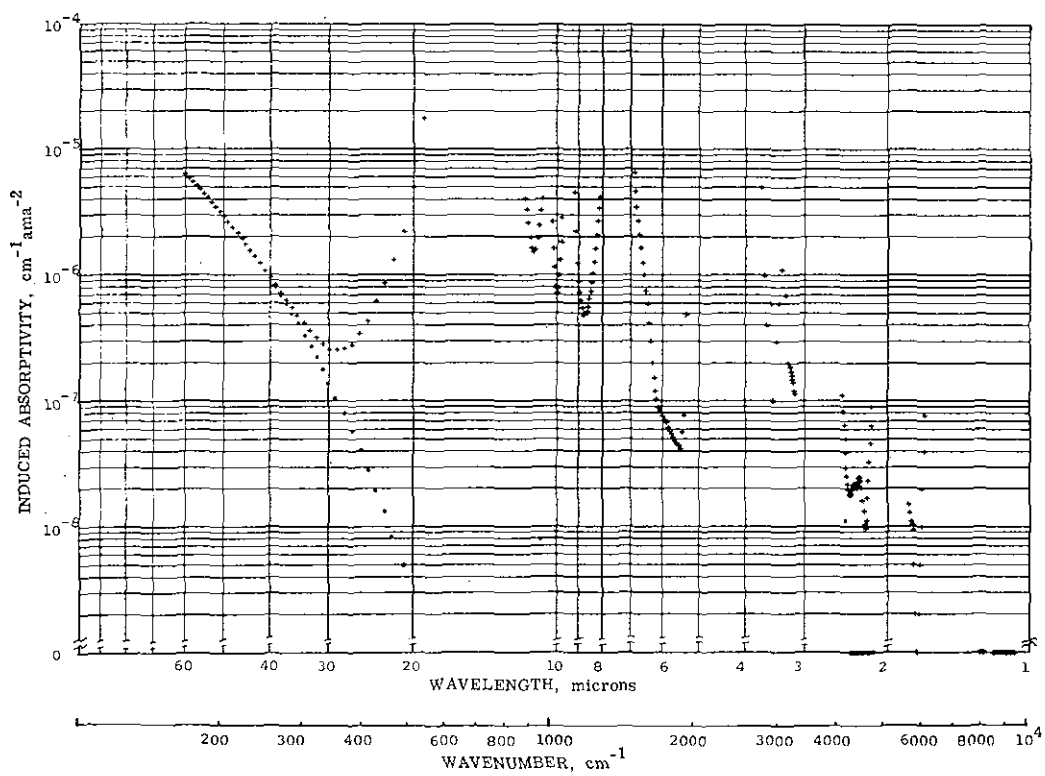

Fig. 18. Induced absorptivity in the ten windows. Crosses are basic values; dots in the long-wave region omit the estimated far wing of the 667 cm^{-1} band, but include the extrapolation from Ho, Birnbaum, & Rosenberg (1971). The zero values in the 2.3u region were used to evaluate the significance of the $00^00\text{-}3^11$ induced transitions.

b) The effect on the spectrum of individual rotational lines is not considered. Pronounced rotational structure appears in the strong allowed bands, not in the windows, except for a few weak hot bands and scarcer isotopic transitions. In these cases, it may be noted that the amplitude between peak and trough is reduced by pressure broadening to about 30% at 4 atm, permitting averaging over the rotational lines at altitudes of 40 km and lower on Venus.

c) Absorptivity is assumed to be either linear or square-law in density. Intermediate cases actually occur between the centers of bands and their far wings, but such near wings are outside the windows except for the edges of the 11.2, 10.0, and 8.75μ windows. In these, treating the experimental data as square-law is conservative.

d) The cloud may not have a well-defined bottom. Condensable or particulate material may extend to lower altitudes or even to the surface. This possibility can not be taken into account until more observational evidence from Venus is available to provide the parameters on composition, size, number density, etc.

C. CALCULATIONS

1. Transfer Equation

The radiative properties of the model of the lower Venus atmosphere were obtained through numerical integration of the transfer equation as in Chandrasekhar (1960). For upward radiation intensity I at a given wavelength, it gives:

$$I(\tau, \theta, \phi) = I(\tau_o, \theta, \phi) e^{-(\tau_o - \tau)/\cos\theta} + \int_{\tau}^{\tau_o} \mathcal{J}(t, \theta, \phi)\, e^{-(t-\tau)/\cos\theta}\, dt/\cos\theta \qquad (9)$$

where τ is the optical depth ($\tau = \tau_o$ at the surface), and $\mathcal{J}$ is the source function. The downward intensity is given by (9) if $\cos\theta$ and τ_o are replaced by $-\cos\theta$ and τ_m, where τ_m is the optical depth at the bottom of any opaque clouds; $\tau_m = 0$ for no clouds.

Assuming symmetry around the vertical, the radiation flux is

$$\mathcal{F} = 2\pi \int_o^{\pi} I(\theta) \cos\theta \sin\theta \Delta\theta \qquad (10)$$

Since the local temperature is defined, and since scattering is not considered, the source function $\mathcal{J}$ becomes B(T), the Planck function. In the absence of other sources, $I(\tau_o, \theta, \phi)$ is $\varepsilon B(T)$, at T_o or T_m, the temperature of the surface or cloud bottom.

2. Step Size

The number of steps in the numerical integrations over height, angle, and wavelength were varied in a series of trials, in which accuracy was checked as the number of steps was changed.

Intervals of 0.2 km were used in height. In angle, 20 steps were used (10 in each hemisphere), with size varying as described by Diamante (1969) so as to provide annuli of equal projected area.

In wavelength, 201 steps were used, with closer intervals in those spectral regions with more rapid changes of absorptivity. The step sizes were:

from 60.5μ to 15.0μ, 1.0μ wide,

from 15.0μ to 10.0μ, 0.1μ wide,

from 10.0μ to 3.25μ, 0.05μ wide,

from 3.25μ to 1.0μ, 0.01μ wide.

D. RESULTS

1. Flux

Figure 19 shows total flux for all wavelengths versus altitude, including the effect of infrared-opaque clouds. The level of flux for a black body at 251K, the cloud-top temperature, is also shown. Curves are also given indicating the amount of flux without the induced absorptions found in the present study near 2.3μ (the $00^{0}0$-$3^{1}1$ pair), and without

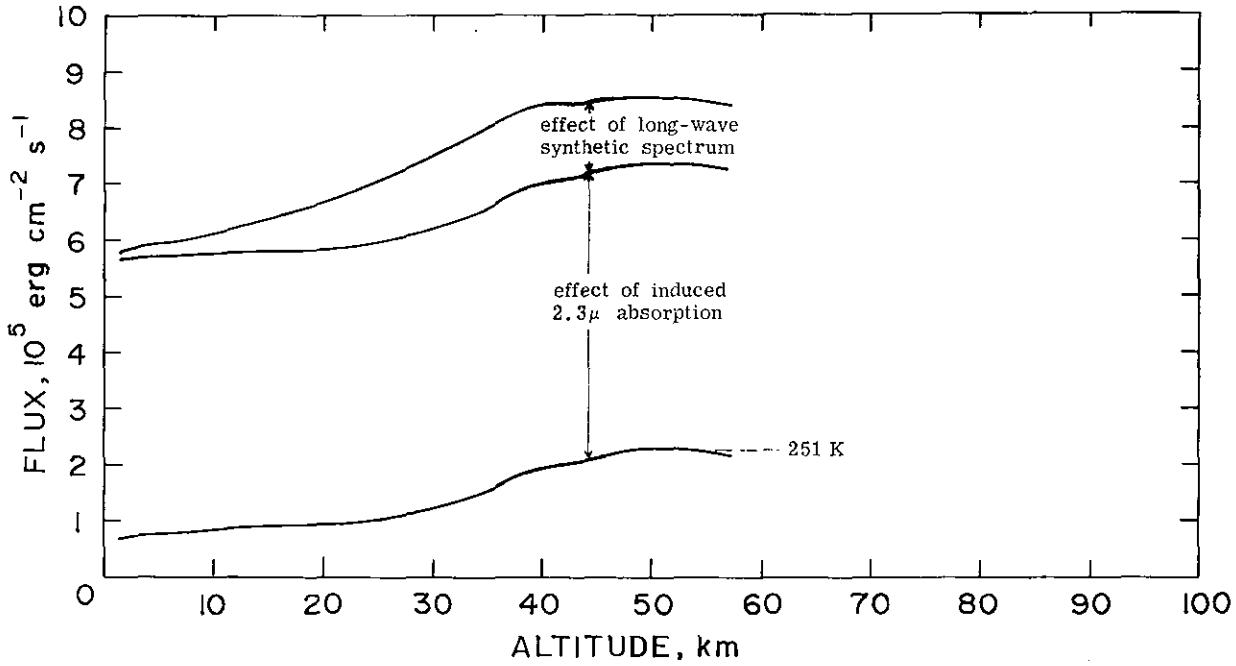

Fig. 19. Total radiative flux versus altitude, with a cloud bottom at 59 km. The black-body flux at 251 K is indicated. The lowest curve is with all absorptions, as labeled by crosses in Figures 17 and 18. The middle curve is without the induced absorption in the 2.3 μ region (section IV. B. 1). The top curve is without the 2.3 μ induced absorption and, in the long-wave region, without the allowed hot bands and the induced far wing of the 667 cm^{-1} band (see section VI. B. 3); values are labeled by dots in Figures 17 and 18.

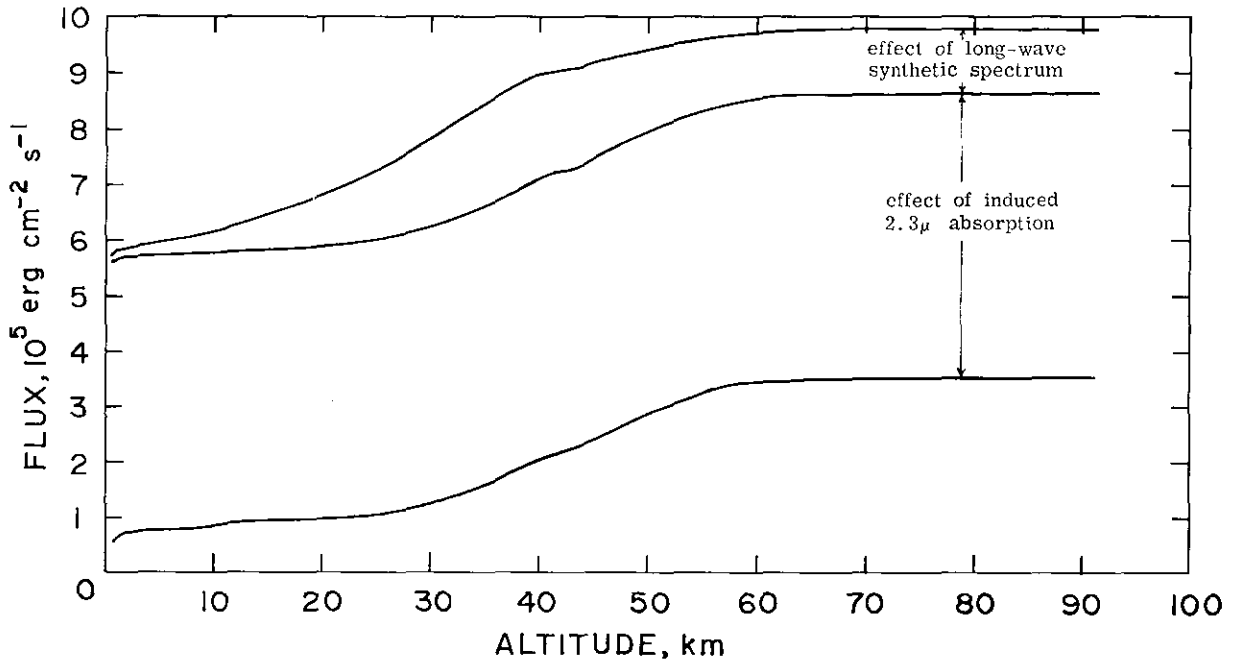

Fig. 20. Flux versus altitude without the effects of opaque clouds. Curves are as described in Figure 19.

the synthetic spectrum between 60.5 and 20.5μ in the long-wave region (though the induced rotational absorption from Ho, Birnbaum, & Rosenberg (1971) is still included). Neglecting the slight decrease which results from the cloud discontinuity, the flux entering the cloud bottom is 2.3×10^{5} ergs cm^{-2} s^{-1}, which compares closely with a cloud-top emission of 2.25×10^{5} ergs cm^{-2} s^{-1} at 251K. It is therefore not necessary to invoke the presence of other absorbers than CO_2 to sustain a surface temperature of 768K.

The induced $00^{0}0\text{-}3^{1}1$ transitions found in the present study are quite significant to this conclusion. This can be seen by noting the difference between the lower and middle curves in Figure 19: without the 2.3μ induced absorptions, an <u>additional</u> 5.1×10^{5} ergs cm^{-2} s^{-1} would reach the cloud bottom. Similarly, the upper curve shows that, without the long-wave synthetic spectrum, there would be an additional 1.1×10^{5} ergs cm^{-2} s^{-1}. While these increases may at first appear large (considering especially the narrowness of the 2.3μ window), they are actually small in comparison to the total flux of 1.98×10^{7} ergs cm^{-2} s^{-1} that would be emitted from the surface if there were no greenhouse effect.

Figure 20 presents the results of similar calculations without clouds, for comparison only; the curves have little physical significance, as they do not allow for radiative transfer in the upper atmosphere.

2. Other Variables

In the process of computing intensity and flux, other quantities were readily obtained as functions of wavelength. Optical depth is shown in Figure 21; the values (which, though not shown, are much higher in the more strongly absorbing regions between the windows) meet the criterion estimated by Wattson (1971) that an average optical depth between 10^3 and 10^4 is required to support the surface temperature.

The radiation intensity in the windows, averaged across the disc of Venus, that might be expected if there were no clouds, is shown in Figure 22. The effect of the upper atmosphere is not included.

Figure 23 shows the effective radiating altitude (that whose optical depth is equal to $\tau_m + 1$). For the wavelength regions between the windows, the effective altitude is above the clouds. Some of the deviations from smoothness in flux versus altitude (Figures 19 and 20) are explained by the fact that there are certain altitudes (such as 42-44 km) where a number of different wavelengths all "decouple" from the atmosphere (reach a large mean free path) at once; their energy is thus appropriate to the temperature at the effective altitude. This effective temperature is given in Figure 24; in the transparent windows, it is equal to the surface temperature.

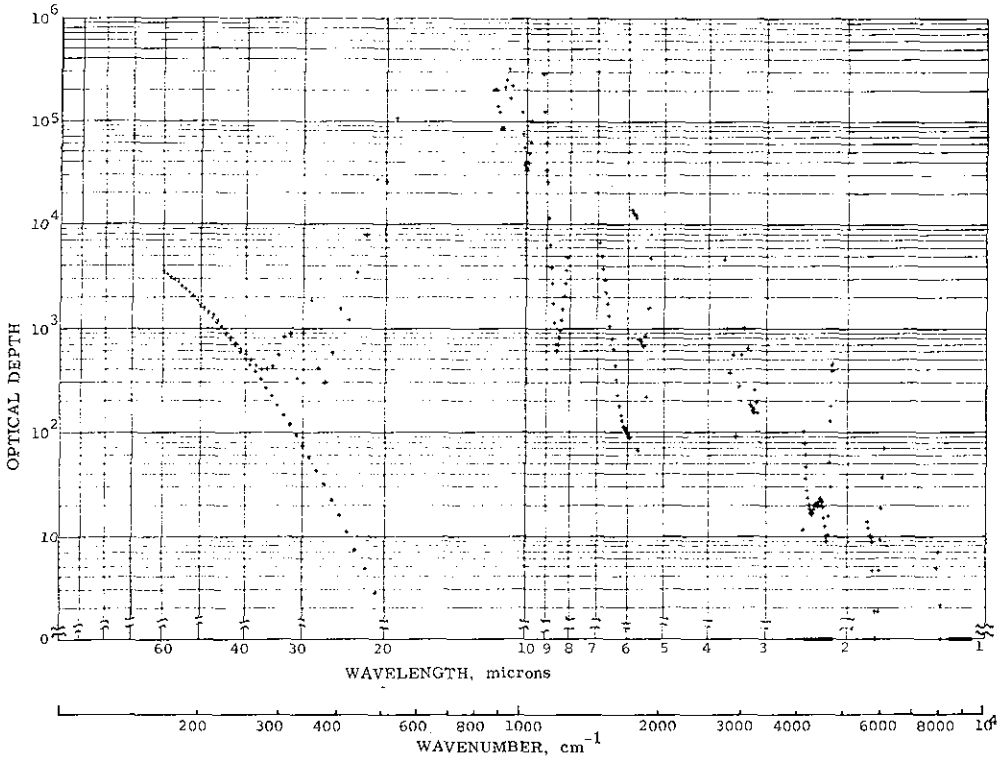

Fig. 21. Optical depth in the ten windows; between the windows, values are large. Clouds are not considered. Symbols are as in Figure 18.

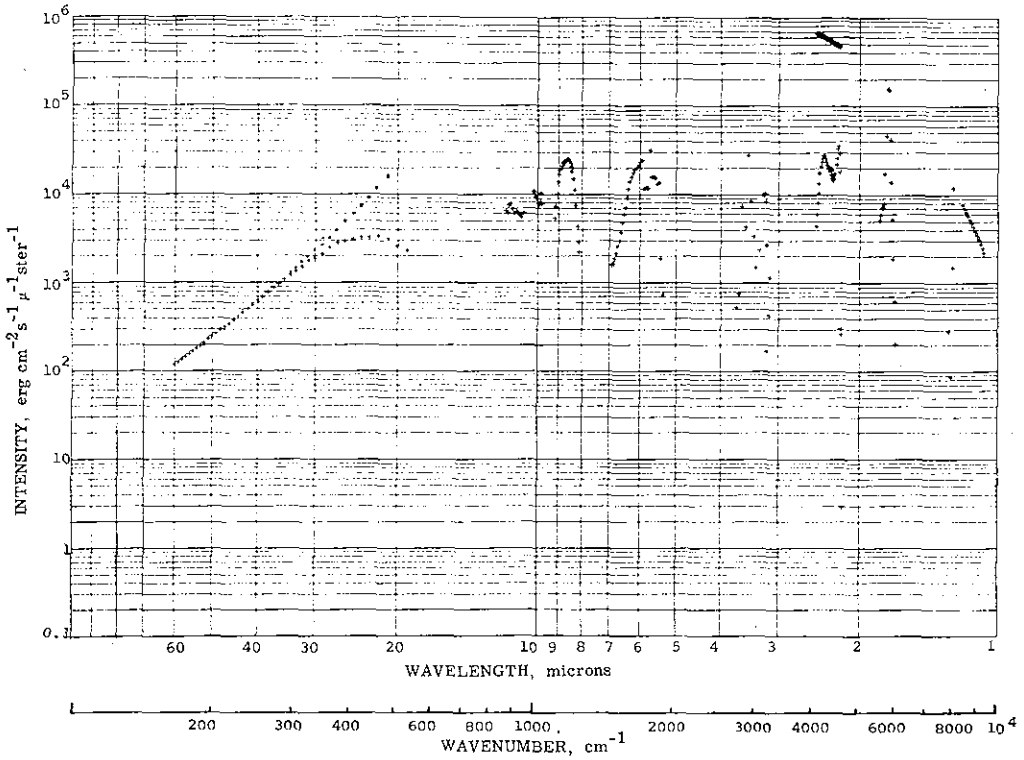

Fig. 22. Intensity from a CO_2 atmosphere without clouds, averaged across the disc of Venus, in the ten windows; between the windows, values are small. Symbols are as in Figure 18.

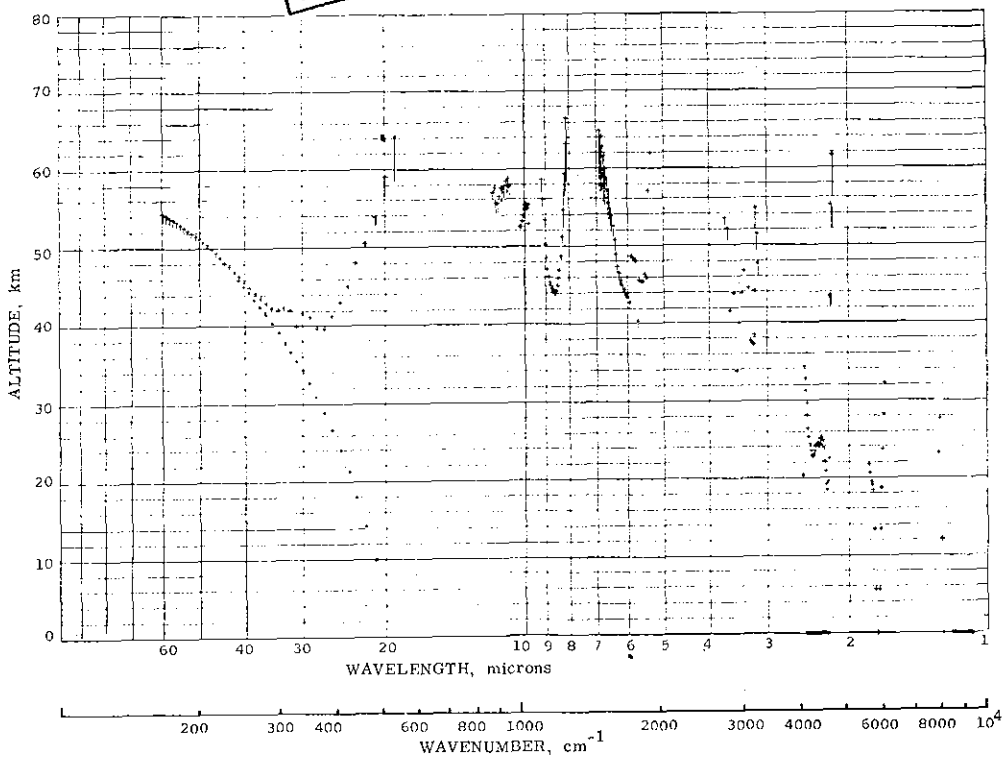

Fig. 23. Effective radiating altitude -- that whose optical depth is unity in the absence of clouds -- in the ten windows; between the windows, values are large. Symbols are as in Figure 18, with vertical lines added to show the lowering of effective altitude when clouds are present.

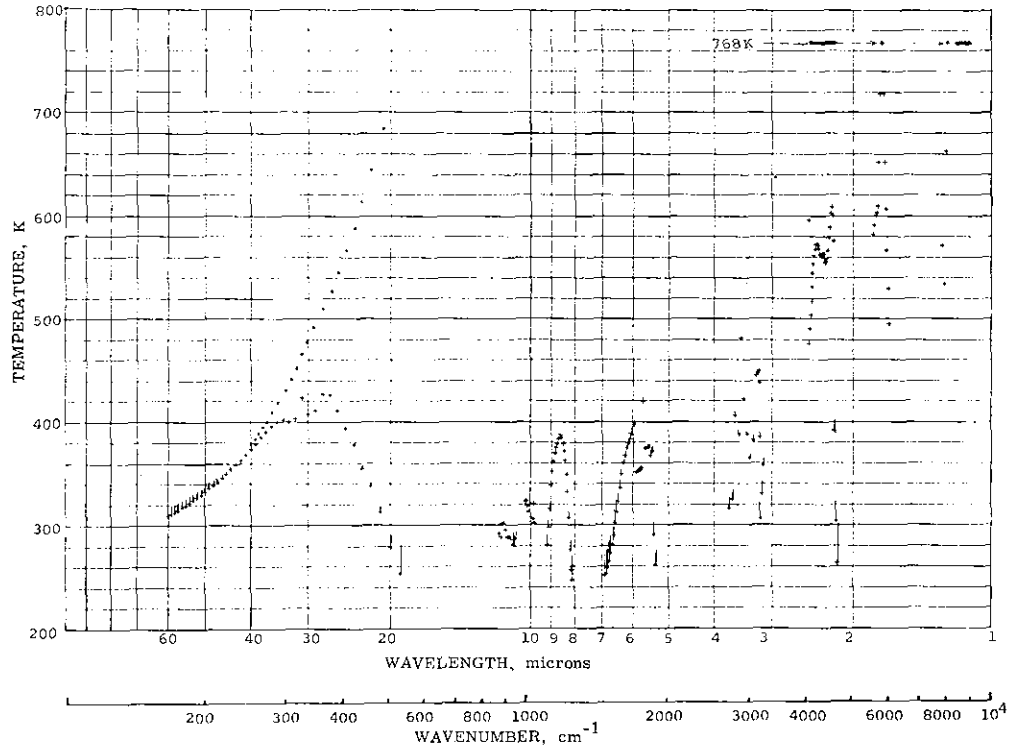

Fig. 24. Effective radiating temperature -- that corresponding to the effective altitude in Figure 23. Between the windows, values are small. The surface temperature is visible in transparent regions. Symbols are as in Figure 18, with vertical lines added to show the raising of effective temperature seen by the cloud bottom (not by an external observer) when clouds are present.

3. Comparison with Observation

The agreement shown in Figure 19 between the flux reaching the cloud bottom and that leaving the cloud top depends on the cloud-top temperature. While the 251K value is based on results from the Venera spacecraft, it is higher than the 235K to 245K often quoted on the basis of brightness temperature in the 8_{μ} region. It is therefore desirable to take a more comprehensive view of brightness temperature. Unfortunately, the available observations at other wavelengths are sparse. The results of Hanel, Forman, Stambach, & Meilleur (1969) show brightness temperatures rising from 240K at 8.5_{μ} to 255K at 12_{μ}, on the basis of carefully calibrated measurements from 8.4_{μ} to 9.4_{μ} and 10.3_{μ} to 13_{μ}. "Absorption-like" features are seen at 9 and 11.2_{μ}. Gillett, Low, & Stein (1969) cover the ranges 2.9 to 5.7_{μ} and 7.4 to 13.8_{μ}. Though similar dips are visible, their brightness temperatures are lower than those of Hanel et al., except for higher values at shorter wavelengths. A sharp rise to 350K at 2.9_{μ} is attributed to solar scattering, at least in part.

More recently, F. J. Low (1971) states that solar scattering has still prevented acceptable short-wave work, but broad-band observations in the 17.5 to 25_{μ} region show a rise of about 15K as compared to the 8 to 10_{μ} region (Armstrong, 1971). Since the 15_{μ} band of ν_2 in CO_2 plays a strong role out to 20_{μ}, the increase between 20 and 25_{μ} must be even larger. The work of F. J. Low and Armstrong also shows a

drop between 30 and 47μ, followed by an increase to over 270K from 46 to 100μ. In summary, it appears that a broad-band average of brightness temperatures may well agree with a cloud-top temperature near 250K.

Referring again to the work of Hanel et al. and Gillett et al., the fact that the intensities versus wavelength which they observe do not exhibit the variations in Figure 22 indicates a high degree of attenuation in the clouds, and justifies treating them as infrared opaque. It should again be emphasized that the parameters used in the present study are appropriate primarily to transfer within the lower atmosphere. While the results herein cannot exclude the possible presence of absorbing gases, dusts, or droplets below the clouds, they do indicate that infrared-absorbing constituents other than CO_2 are not required to explain the high surface temperature.

VII. ACCURACY AND STATISTICS

To confirm that the absorptions found in the 2.3μ region are due to collision-induced transitions, their proportionality to density squared must be verified. Then the accuracy of the peak and integrated absorption, and of other derived quantities, must be obtained. Finally, the accuracy of the application to the Venus atmosphere must be assessed.

A. FUNCTIONAL DEPENDENCE ON DENSITY

The experimental observations of absorption versus density can be fitted to smooth functions, using a least-squares approach to determine the function parameters. Where a choice of several possible functions exists, statistical tests can be made between them. The peak absorptions shown in Figure 15 were fitted four different ways: to polynomials of first, second, and third degree, and to a single term in density squared. Since there are not enough points to use a χ^2 test (at least 30 are recommended by Parratt, 1961), the F test is used.

Table 7 shows, for the four functional fits, the values of Parratt's $\Omega = (\Delta y)^2/(\text{d. f.})$, the sum of squared deviations around the regression line, divided by the number of degrees of freedom. The goodness of fit is tested for two different wavelengths, labeled B and D in Figure 15, and which are plotted versus density as x's and dots, respectively, in Figure 16. Note that the statistical measure F is defined as the ratio of Ω's when comparing two hypotheses.

TABLE 7: GOODNESS OF FIT

Type of Fit	Point B	Point D
(1) $A_0 + A_1x$	$\Omega = 0.25\times10^{-2}$	0.18×10^{-2}
(2) $A_0 + A_1x + A_2x^2$	$\Omega = 0.81\times10^{-4}$	0.59×10^{-4}
(3) $A + A_1x + A_2x^2 + A_3x^3$	$\Omega = 0.66\times10^{-4}$	0.63×10^{-4}
(4) A_2x^2	$\Omega = 0.87\times10^{-4}$	0.69×10^{-4}
Compare (1) and (2)	F = 30.8	30.3
Compare (4), best of (2), (3)	F = 1.32	1.17

A highly significant improvement occurs going from a linear fit to any of the others: for point B, the improvement will occur due to chance about once in 10^6, and for point D, less than once in 10^7. On the other hand, there is little difference between fits (2), (3), and (4). With respect to the pure square-law fit, (4), adding other constant, linear, or cubic terms gives no significant improvement, as the F-ratios could occur by chance 32% of the time for B and 38% of the time for D. Acceptance of the single term of the form A_2x^2 therefore seems justified.

B. ERRORS

1. Signal-Level Errors

The individual absorption measurements are affected by numerous sources of error. The quantity used in calculations is the logarithm

of the transmission ratio between CO_2 and N_2 -- where the separate measurements on the two gases were taken days or weeks apart. Thus, ordinary problems such as instrument error, reading error, etc. are supplemented by long-term drift, effects of filling the tank, etc.

On the basis of five test runs with N_2 over a period of seven weeks, r. m. s. errors appear to be:

Output noise fluctuations and reading error	0. 2%
Instrument error	0. 5%
Instrument drift	0. 5%
Source intensity variation	1. 0%
Hysteresis from pressure changes	1. 0%

Summing these twice on an r. m. s. basis (once for CO_2 and once for the N_2 reference) we obtain an r. m. s. error of ±2. 3% in the ratio. After taking the logarithm of the transmission ratio, this becomes an absolute error (not a percentage) of ±0. 023.

2. Gas-Based Errors

Temperature could be measured within ±0. 5C and pressure within ±5 p. s. i. *, on an r. m. s. basis. This causes density errors that are

*The pressure gage is rated with a maximum error of 10 p. s. i. in the range used. This is taken as 2σ rather than the usual 3σ because the manufacturer's quality standards cut off the tail of the distribution.

±0.17% and ±0.3 amagat, respectively, at low pressures, but rise rapidly as the critical point is approached. For example, at 60, 75, and and 95 ama, the combined effects are 1.6, 2.1, and 3.8 ama; with absorption proportional to density squared, apparent errors will be 5.3%, 5.8%, and 8.0%.

3. Effects of Errors on Absorption

Recalling from section IV. D. 1 that the spectra fell into three classes, we can estimate the error in optical depth as the r. m. s. sum of signal-level and gas-based errors for the spectra in class (a) -- those not requiring normalization. For those with normalization, class (b), the errors are estimated to be about twice as large. Though the errors in the lower-pressure spectra in class (c) will be smaller (since they were not compared to the N_2 reference spectrum), they do not affect the accuracy of the overall results.

Sample error bars have been placed in Figure 16 to show the errors in each class of spectra; in combination, they lead to an error in the induced absorptivity at each wavelength of about 10%. This is increased to 15% in the induced strength because of uncertainties in estimating the far wings of allowed lines, which must be subtracted.

In both the induced $3^1 1$ Fermi pair and the simultaneous transitions with N_2 (Figures 10 and 11) the relative error between absorptivities

at different wavelengths is of the order of 1% or less; the 15% applies to the overall level.

C. EFFECT OF ERRORS ON DERIVED QUANTITIES

Errors in the ratio between the $11^1 1$ and the $03^1 1$ matrix elements were derived by performing the calculation three times: at the central point and at the error extremes.

The polarizability derivative α'''_{123} is proportional to the square root of the induced strength and to the quadrupole moment. With the errors in induced strength and quadrupole moment being 14% and 5%, the formal error in this polarizability derivative would be 8.5%. This has arbitrarily been increased to 15% in order to allow for other errors. These might include errors in using the Lennard-Jones potential, as well as any other hidden or systematic errors.

D. ERRORS IN APPLICATION TO THE VENUS ATMOSPHERE

Considering the many sources of data used in section VII, any generalization about errors in the atmospheric results would be inappropriate. Instead, the sensitivity of the results to changes in the data was evaluated by varying the parameters in the computer analysis.

The only sensitive result is the optical depth at the surface, which is directly proportional to the absorption coefficients, and varies even more rapidly with surface density. For example, the additional CO_2

due to a 1-km reduction in radius increases the surface optical depth by about 15% at most wavelengths.

Other results are affected much less. This is because the emerging intensity is that of a black body whose temperature is at the "effective altitude" where the optical depth is unity (see Figure 24). Since typical density and temperature gradients are 6% per km and 8.5K/km, a 10% change in absorptivity will shift the effective altitude by 1.7km and the effective source temperature by only 1.4K. As examples in the Rayleigh-Jeans portion of the spectrum, a two-to-one change in both components of absorptivity causes only a 9% change of intensity; a 5% change in the CO_2 mixing ratio causes under 1% change in intensity.

The sensitivity is greater at wavelengths near the peak of the Planck curve and shorter (the peak is near 3.8μ for the 768K surface temperature), but these wavelengths contribute less than 20% of the total flux. Empirically, variation of 3 km in radius produces less than 1% change in the total flux; variations of 5% in the CO_2 mixing ratio produces less than 0.4%.

VIII. CONCLUSIONS

Using equipment built to detect previously unobserved collision-induced infrared absorptions, total strength of two new overlapping CO_2 bands near 2.3μ has been measured to be $(6.2 \pm 0.9) \times 10^{-6}$ $cm^{-2}ama^{-2}$. One is centered at 4240 ± 20 cm^{-1}, with strength $(2.6 \pm 0.5) \times 10^{-6} cm^{-2} ama^{-2}$; the other is centered at 4380 ± 20 cm^{-1}, with strength $(3.6 \pm 0.6) \times 10^{-6} cm^{-2} ama^{-2}$. These absorptions are attributed to induced transitions from ground to the Fermi pair $3^1 1$ at 4247 and 4391 cm^{-1}, and to the associated hot bands $01^1 0\text{-}4^0 1$ and $01^1 0\text{-}4^2 1$ with the same change in quantum numbers. The induced strength of the transitions from ground is $(5.25 \pm 0.25) \times 10^{-6}$ $cm^{-2}ama^{-2}$. The strength ratio of the upper absorption to the lower is 1.4 ± 0.2. From this, the lower unperturbed state $11^1 1$ is calculated to have a matrix element for the transition from ground $8.1^{+3.5}_{-1.7}$ times that of the upper state $03^1 1$. Such a crossing-over of strengths is shown also to occur in the CO_2 Fermi Raman pair near 7.5μ.

Absorptions due to simultaneous transitions $0 \rightarrow 1$ in N_2 plus $00^0 0\text{-}3^1 0$ in CO_2 have been observed; though their intensity increases in proportion to the amount of N_2 as expected, their shape requires further study at higher resolution. Evidence is presented for observation of the induced $00^0 0\text{-}00^0 2$ transition in CO_2 at 4673 cm^{-1}, with strength $3.8 \times 10^{-6} cm^{-2} ama^{-2}$. The induced $00^0 0\text{-}01^1 1$ transition at 3004 cm^{-1} has been observed in more detail than in previous work,

finding its strength to be $(6.2 \pm 1.3) \times 10^{-5} cm^{-2} amg^{-2}$.

Previous investigations have been surveyed or analyzed to obtain strength estimates of three other induced groups. These and the results herein have been used to calculate eight of the polarizability derivatives of the CO_2 molecule, including an improved value of $\alpha_1' = 1.20 \times 10^{-15} cm^2$, and all second derivatives. The change in strength with v_2 (for fixed v_3) has been determined, and is less rapid in induced groups than in the allowed groups with the same v_3.

Induced absorptivity versus wavelength has been measured in three "window" regions between 12μ and 8μ. The results permitted testing and rejecting a hypothesis that the far wings of allowed lines become increasingly sub-Lorentzian at longer wavelengths.

The experimental results in this study have been combined with those of other references to generate linear and density-squared components of absorptivity versus wavelengths in ten windows. Applying the window absorptivities to a profile of the Venus atmosphere, the flux reaching the bottom of the clouds is found to agree closely with the blackbody flux at the cloud-top temperature. Without the induced transitions discovered in the 2.3μ region, substantial additional opacity would be required from some other substance than CO_2.

APPENDIX A. REVIEW OF CO_2 VIBRATIONS

1. General

In carbon dioxide, the vibrational modes are: ν_1, a symmetric stretch; ν_2, a bending which is degenerate with respect to two orthogonal planes through the molecular axis; and ν_3, an asymmetric stretch. The degenerate bending modes combine to give a generalized bending and a rotation around the axis. The quantum number of this rotation, ℓ, is equal to or less than v_2 (the quantum number of ν_2), and is even or odd according to v_2. The modes are shown in Figure 25.

2. Infrared and Raman Activity

The ν_2 and ν_3 modes are observed in the infrared, with wavenumbers 667 and 2349 cm^{-1}. Because of the symmetry of the CO_2 molecule, it has no dipole moment at rest, nor during symmetric axial displacements of the oxygen atoms. The ν_1 mode and pure rotational transitions (around a normal to the axis) are therefore not optically active. For ν_2 and ν_3, opposing displacements are centrally symmetric, so that their even harmonics are also optically inactive.

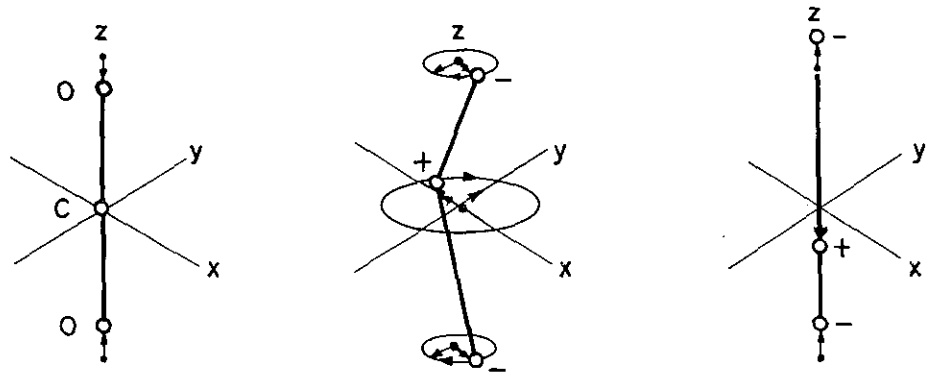

$\nu_1^0 = 1332.87\ cm^{-1}$
NO DIPOLE MOMENT

$\nu_2 = 667.38\ cm^{-1}$
DEGENERATE IN THE X-Z AND Y-Z PLANES, COMBINE AS ROTATION

$\nu_3 = 2349.14\ cm^{-1}$
STRONGEST DIPOLE

Fig. 25. The three fundamental modes of vibration of the carbon dioxide molecule.

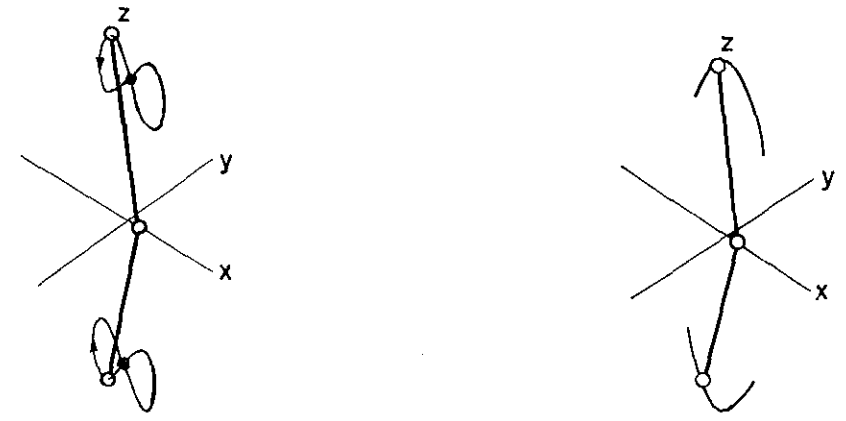

$W = 1285.41\ cm^{-1}$

$W = 1388.19\ cm^{-1}$

Fig. 26. Two classical trajectories in the x-y plane, which might correspond to the $2^0 1$ Fermi pair. Each is a Lissajous combination of the ν_1 and $2\nu_2$ classical motions; the two trajectories can be summed with appropriate phases to yield the straight-line motion for either ν_1 or $2\nu_2$.

Since the polarizability of CO_2 is, by symmetry, the same at either extremum for both ν_2 and ν_3, $\partial\alpha/\partial\xi_2 = \partial\alpha/\partial\xi_3 = 0$, and these modes will not be active in the Raman effect. The polarizability of ν_1 is different at its two extrema. It is therefore expected to be active in the Raman effect, as are pure rotational transitions and the even harmonics of the other two vibrational modes.

3. Induced Infrared Activity

Although the polarizing field in the Raman effect oscillates many times during the period τ of molecular vibration, Condon (1932) suggested that Raman-active vibrations might also be excited in the infrared region by an intense fixed polarizing field or by the transient fields resulting from close approaches of other molecules. The latter can be thought of as fixed from the point of view of molecular vibration: in CO_2, the strong Raman-active vibrations have $\tau \sim 3 \times 10^{-14}$ s, while a room-temperature molecule with a relative velocity $v \sim 3 \times 10^4$ cm/s will pass the molecular length of 2×10^{-8} cm in about 6×10^{-13} s, so that the induced field lasts over 20τ.

Since Raman activity is at a frequency displaced from that of the exciting line by the vibrational frequency, the displacement from "zero-frequency" excitation will be in the infrared, at the vibrational frequency itself. Actually, the displacement should be around the frequency spectrum corresponding to the Fourier transform of the

encounter time. This would give a half-width of about 60 cm^{-1} at room temperature, as is actually observed.

If the perturbing molecule is different from the perturbed molecule, it is possible for simultaneous transitions to be induced. In these, a single photon of incident radiation raises the energy of both molecules, giving rise to absorbing bands which are not present in either molecule alone. The likelihood of collision-induced absorption and of simultaneous-transition absorption depends on the number of collisions in the absorbing path. For foreign-gas induction, this is proportional to the path length times the product of the molecular densities of the two gases. For self-induction, it is proportional to the path length times the square of the density.

There are two other types of absorption that are proportional to density squared. First, the rigid motions of translation and rotation can be seen in the microwave and far infrared region. Second, absorption far from the center of an allowed line is also proportional to density squared at any given wavelength, even though the shape is not a predictable function of wavelength (Burch, Gryvnak, Patty, & Bartky, 1968).

4. Fermi Resonance

The ν_1 and $2\nu_2$ lines are found in the Raman effect at 1285 and 1388 cm^{-1}, rather than at their expected positions (both near 1336 cm^{-1}).

Fermi (1937) showed that if several vibrations with nearby energy levels have the same symmetry species, and if there is a cross-term in the potential function, mutual perturbations push the energy levels apart (without changing the average energy of the group). In the case of two interacting levels, the perturbed levels W' formed from the unperturbed levels W_A^o and W_B^o are

$$W' = \frac{1}{2}\left(W_A^o + W_B^o\right) \pm \sqrt{\delta^2 + 4W_{AB}^2} = \bar{W} \pm \Delta/2 \qquad (A1)$$

where W_{AB} is the interaction term, and δ is the unperturbed difference $|W_A^o - W_B^o|$.

The eigenfunction ψ' of each Fermi-perturbed level can be regarded as a mixture of the unperturbed eigenfunctions

$$\psi'_A = a\psi_A^o + b\psi_B^o \quad ; \quad \psi'_B = b\psi_A^o + a\psi_B^o \qquad (A2)$$

with $a^2 + b^2 = 1$ and $a^2,\ b^2 = 1/2 \pm \delta/2\Delta$. (A3)

In the case of CO_2, a Fermi group is formed from any set of levels with the same ℓ and v_3, and with a constant sum of v_1 and $2v_2$. Such groups can, of course, occur in infrared or Raman spectra. The Raman pair above is the result of interaction between the unperturbed ν_1 and $2\nu_2$ at 1332.87 and 1340.74 cm^{-1}, respectively. Figure 26 shows two possible motions for this pair. In each, one cycle of ν_1 occurs during each half-cycle of ν_2 (the latter at an amplitude corresponding to quantum number 2).

5. Energy Levels

Observed energies of overtone vibrations and of combinations of several vibrations are slightly different from sums of the fundamental energy levels, due to anharmonicity in the potentials of the three displacements. Dennison (1940) showed that higher-order and cross-terms in the potential cause additional terms in the energy formula, and gave an expression for the term values (energy divided by hc), referred to the potential minimum.

It is usually more convenient to refer the energy to the lowest state, thus deducting the zero-point energy. In CO_2, the appropriate expression includes modifications to allow for the ν_2 degeneracy; third-order terms provide sufficient accuracy for all experimental work:

$$G^o = g_{22}\ell^2 + \sum_i^3 \left(\omega_i^o v_i + y_{i\ell\ell}\ell^2 v_i \right) + \sum_{i \le j}^3 \sum^3 x_{ij}^o v_i v_j + \sum_{i \le j \le k}^3 \sum^3 \sum^3 y_{ijk} v_i v_j v_k \qquad \text{(A4)}$$

Table 8 gives values for the spectroscopic constants in equation (A4), from Benedict and Wattson (1969).

NOTE ADDED IN PROOF: Cihla & Chedin (1971) give constants for nine isotopic species, referenced to the potential minimum.

TABLE 8: CO_2 VIBRATIONAL CONSTANTS

ω_1°	= 1335.7470	ω_2°	= 667.2133	ω_3°	= 2361.6319
x_{11}°	= -2.9697	x_{22}°	= 1.6162	x_{33}°	= -12.5318
x_{12}°	= -5.3564	x_{13}°	= -19.1963	x_{23}°	= -12.4953
y_{111}	= -0.0019	y_{222}	= 0.0085	y_{333}	= 0.0052
y_{112}	= 0.0	y_{122}	= -0.0025	y_{113}	= -0.0864
y_{133}	= -0.0602	y_{223}	= -0.0022	y_{233}	= 0.0187
y_{123}	= 0.0	W_e	= 51.7416	$g_{\ell\ell}$	= 1.4604
$y_{1\ell\ell}$	= -0.0120	$y_{2\ell\ell}$	= 0.0184	$y_{3\ell\ell}$	= 0.0103
λ_1	= 0.5120	λ_2	= 0.6591	λ_3	= 0.2840
W_{22}	= 0.0100	W_{23}	= -0.1030		

The W and λ are used to calculate the interaction between levels in Fermi resonance:

$$2W_{AB} = \left[W_e - \lambda_1 v_1 - \lambda_2 v_2 - \lambda_3 v_3 - W_{22} v_2^2 - W_{23} v_2 v_3\right] \left[(v_2+2)^2 v_1 - \ell^2 v_1\right]^{\frac{1}{2}} \quad \text{(A5)}$$

where the levels have quantum numbers $v_1 v_2^{\ell} v_3$ and $(v_1-1)(v_2+2)^{\ell} v_3$. For more complex Fermi groups with N members, perturbed levels are found by linearizing the N x N matrix with the W_{AB} as off-diagonal elements. Table 9, at the end of this Appendix, gives term values and other data up to the $01^1 2$ level for various isotopic species.

6. Molecular Constants of CO_2

- C - O spacing, L — 1.16×10^{-8} cm (Herzberg, 1945)
- Effective charge on each oxygen — -1.01×10^{-10} esu (Fahrenfort, 1955)
- Quadrupole moment — $(-4.5 \pm 0.2) \times 10^{-26}$ esu-cm^2 (Ho et al., 1971)
- Moment of inertia — 7.17×10^{-39} g-cm^2 (Herzberg, 1945)
- Mie 6-12 (Lennard-Jones) potential constants: (Fahrenfort, 1955)

  Radius 4.57×10^{-8} cm Energy 25.6×10^{-15} erg.
- Polarizability, r.m.s. — $\bar{\alpha} = 26.5 \times 10^{-25}$ cm^3 (Brand and Sparkman, 1960)
- Force constants: for symmetric stretch $k_1 = 16.8 \times 10^5$ dyne/cm; for bending $k_\theta / L^2 = 0.57 \times 10^5$ dyne/cm. (Herzberg, 1945)
- Normalization factors for dimensionless normal coordinates

$$N_1 = \sqrt{h/2\pi^2 m\nu_1 c} = 0.562 \times 10^{-9} \text{ cm}$$

$$N_2 = \sqrt{h(2m+M)/8\pi^2 mM\nu_2 c} = 0.760 \times 10^{-9} \text{ cm}$$

$$N_3 = \sqrt{h(2m+M)/8\pi^2 mM\nu_3 c} = 0.405 \times 10^{-9} \text{ cm}$$

- Potential* $V/hc = 677.37\xi_1^2 + 336.45\xi_2^2 + 1198.16\xi_3^2 - 30.2\xi_1^3 + 73.9\xi_1\xi_2^2 - 251.\xi_1\xi_3^2 - 0.33\xi_1^4 + 52.\xi_2^4 + 0.01\xi_3^4 + 296.\xi_1^2\xi_2^2 + 25.9\xi_1^2\xi_3^2 - 27.55\xi_2^2\xi_3^2$

---

* Recalculated after Dennsion (1940), using his rotational constants and those in Table 8. Coefficients of ξ_2^4 and $\xi_1^2\xi_2^2$ are doubtful because Fermi resonance is not well handled as a perturbation, and because of the influence of higher-order terms (see Cihla & Chedin, 1971). For a different approach, see Statz, Tang, & Koster (1966).

Table 9: LOWER ENERGY LEVELS OF CO_2

NOTATION OLD	NOTATION NEW	REPRESENTATION	STRENGTH ama^{-1} cm^{-2}	ISOTOPIC SPECIES AND ABUNDANCES								
				SYMMETRIC				ASYMMETRIC				
				626 0.9839	828 4. x10^{-6}	636 11. x10^{-3}	838 4. 5x10^{-8}	627 0. 8x10^{-3}	628 4. x10^{-3}	728 1. 6x10^{-6}	637 9. x10^{-6}	638 45. x10^{-6}
00^00	00^00	Σ_g^+	ground	<2534.68>$_S$	<2467.99>$_S$	<2482.00>$_S$	<2414.7>	<2517.20>$_S$	<2501.34>$_S$	<2473.9>	<2464.53>$_S$	<2448.47>$_S$
01^10	01^10	Π_u	217.	667.379$_\phi$	657.29$_x$	648.52$_D$	638.2	664.71$_B$	662.29$_B$	659.7	645.96$_S$	643.29$_C$
02^00	20^0,I	Σ_g^+	r	1285.412$_\phi$	1230.13$_S$	1265.82$_B$	1220	1272.35$_B$	1259.43$_C$	1244.7	1255.26$_S$	1244.93$_C$
10^00	20^0,II	Σ_g^+	r	1388.187$_\phi$	1347.00$_S$	1370.05$_C$	1318	1376.05$_S$	1365.84$_C$	1355.5	1355.83$_S$	1342.37$_C$
02^20	02^20	Δ_g	R	1335.129$_\phi$		1297.40$_C$		1329.79$_S$				
03^10	31^0,I	Π_u	4x10^{-3}	1932.466$_\phi$		1896.53$_C$		1916.70$_S$	1902.1$_E$			
11^10	31^0, II	Π_u	5x10^{-2}	2076.859$_\phi$	2024.24$_S$	2037.12$_C$		2057.00$_S$	2049.68$_E$			
03^30	03^30	Φ_u	-	2003.229$_B$		1946.69$_C$						
00^01	00^01	Σ_u^+	2300.	2349.142$_\phi$	2313.97$_x$	2283.490$_\phi$	2247.20$_x$	2340.00$_S$	2332.115$_\phi$	2322.4	2274.10$_S$	2265.973$_\phi$
04^00	40^0,I	Σ_g^+	r	2548.33$_S$		2507.45$_S$			2500.73$_E$			
12^00	40^0,II	Σ_g^+	r	2670.90$_S$		2644.89$_S$		2641.13$_S$	2614.20$_E$			2588.83$_S$
20^00	40^0, III	Σ_g^+	r	2797.02$_S$		2750.50$_S$			2757.14$_E$			
04^20	42^0,I	Δ_g	R	2585.01$_C$		2531.76$_C$						
12^20	42^0,II	Δ_g	R	2760.67$_S$		2700.37$_C$		2743.17$_S$				
04^40	04^40	Γ_g	-	2671.88$_C$								
01^11	01^01	Π_g	r	3004.012$_\phi$	2959.01$_S$	2920.28$_C$	2874.3	2992.72$_S$	2983.80$_S$			

Table 9, continued

NOTATION OLD	NOTATION NEW	REPRESENTATION	STRENGTH $ama^{-1}\,cm^{-2}$	ISOTOPIC SPECIES AND ABUNDANCES									
				SYMMETRIC				ASYMMETRIC					
				626 0.9839	828 $4.\times10^{-6}$	636 $11.\times10^{-3}$	838 4.5×10^{-8}	627 0.8×10^{-3}	628 $4.\times10^{-3}$	728 1.6×10^{-6}	637 $9.\times10^{-6}$	638 $45.\times10^{-6}$	
$05^{1}0$	$5^{1}0,I$	Π_u	3.5×10^{-4}	3181.33_C		3127.25_S		3153.53_S					
$13^{1}0$	$5^{1}0,II$		2.9×10^{-3}	3339.10_C		3289.55_B		3308.55_S					
$21^{1}0$	$5^{1}0,III$		(3×10^{-2})	3500.46_C		3433.65_B		3425.19_S					
$05^{3}0$	$5^{3}0,I$	Φ_u	-	3241.48_C									
$13^{3}0$	$5^{3}0,II$		-	3442.93_C									
$05^{5}0$	$05^{5}0$	H_u	-	3341.00_C									
$02^{0}1$	$2^{0}1,I$	Σ_u^+	31.	3612.844_ϕ	3525.20_x	3527.71_B		3591.36_S	3571.143_G		3508.31_S	3490.35_C	
$10^{0}1$	$2^{0}1,II$		45.	3714.782_ϕ	3638.02_x	3632.917_G		3693.38_S	3675.130_G		3609.28_S	3587.51_C	
$02^{2}1$	$02^{2}1$	Δ_u	*	3659.271_ϕ									
$06^{0}0$	$6^{0}0,I$	Σ_g^+	r	3792.702_B		3731.83_C							
$14^{0}0$	$6^{0}0,II$		r	3942.493_B		3898.39_C		3898.09_S	3856.72_S				
$22^{0}0$	$6^{0}0,III$		r	4064.240_B		4019.77_C		4023.48_B	3987.61_B				
$30^{0}0$	$6^{0}0,IV$		r	4225.111_B	4115.02_S	4145.53_C			4167.91_B				
$06^{2}0$	$6^{2}0,I$	Δ_g	R	3821.984_B		3752.34_C							
$14^{2}0$	$6^{2}0,II$		R	4007.900_B		3936.95_C							
$22^{2}0$	$6^{2}0,III$		R	4197.413_B		4109.49_C							

Table 9, continued

NOTATION OLD	NOTATION NEW	REPRESENTATION	STRENGTH $ama^{-1}\,cm^{-2}$	ISOTOPIC SPECIES AND ABUNDANCES								
				SYMMETRIC				ASYMMETRIC				
				626	828	636	838	627	628	728	637	638
				0.9839	$4.\times10^{-6}$	$11.\times10^{-3}$	4.5×10^{-8}	0.8×10^{-3}	$4.\times10^{-3}$	1.6×10^{-6}	$9.\times10^{-6}$	$45.\times10^{-6}$
06^40	6^40, I	Γ_g	-	3898.487_B								
14^40	6^40, II		-	4122.637_B								
06^60	06^60	I_g	-	4011.027_B								
03^11	3^11, I	Π_g	r	$\underline{4247.714}_B$	4151.17_S	$\underline{4147.24}_C$		4223.51_S	4200.82_S			
11^11	3^11, II		r	$\underline{4390.628}_B$	4303.73_S	$\underline{4287.77}_C$		4366.78_S	4345.92_S			
03^31	03^31	Φ_g	-	4314.985_B		4195.01_S						
07^10	7^10, I	Π_u	4×10^{-5}	$\underline{4416.150}_B$		4343.86_S		4376.45_S	4338.26_S			4274.51_S
15^10	7^10, II		4×10^{-4}	$\underline{4591.118}_B$		4527.28_B		4546.03_S	4504.40_S			4444.18_S
23^10	7^10, III		(4×10^{-3})	4753.45_B		4683.12_B		4710.73_S	4673.08_S			4596.81_S
31^10	7^10, IV		(4×10^{-2})	4973.72_S		4839.99_S		4902.77_S	4872.82_S			4765.58_S
07^30	7^30, I	Φ_u	-	4467.38_S		4381.33_S						
15^30	7^30, II		-	4676.68_S		4585.79_S						
23^30	7^30, III		-	4889.59_S		4781.67_S						
07^50	7^50, I	H_u	-	4558.46_S								
15^50	7^50, II		-	4801.60_S								
07^70	07^70	K_u	-	4681.02_S								

Table 9, continued

NOTATION OLD	NOTATION NEW	REPRESENTATION	STRENGTH $ama^{-1}\ cm^{-2}$	ISOTOPIC SPECIES AND ABUNDANCE								
				SYMMETRIC				ASYMMETRIC				
				626	828	636	838	627	628	728	637	638
				0.9839	$4.\times10^{-6}$	11.10^{-3}	4.5×10^{-8}	0.8×10^{-3}	$4.\times10^{-3}$	1.6×10^{-6}	$9.\times10^{-6}$	$45.\times10^{-6}$
$00^{0}2$	$00^{0}2$	Σ_g^+	r	4673.324 B	4604.01 S	4543.47 S	4467	4655.205 B	4639.502 B	4620.6	4524.88 B	4508.749 B
$04^{0}1$	$4^{0}1,I$	Σ_u^+	0.26	4853.630 ϕ	4721.90 E	4748.058 B		4821.50 B	4791.26 B		4718.35 B	4692.18 B
$12^{0}1$	$4^{0}1,II$		1.08	4977.830 ϕ	4833.17 x	4887.39 B		4939.35 B	4904.85 B		4849.99 S	4814.53 C
$20^{0}1$	$4^{0}1,III$		0.40	5099.662 ϕ		4991.35 B		5068.84 S	5042.54 E			4925.01 B
$04^{2}1$	$4^{2}1,I$	Δ_u	*	4888.001 ϕ		4739.50 C						
$12^{2}1$	$4^{2}1,II$		*	5061.776 ϕ		4939.05 S						
$04^{4}1$	$04^{4}1$	Γ_u	-	4971.04 S								
$01^{1}2$	$01^{1}2$	Π_u	(0.3)	5315.730 B		5168.50 S		5295.08 B	5277.069 B			5128.890 B

FOR NOTES SEE NEXT PAGE

Table 9, Notes

Column 2 — See Appendix B for explanation.

Column 3 — For asymmetric species, drop the subscripts g and u.

Column 4 — Strengths for species 626 are given for all lines allowed in the infrared for symmetric species. Figures in parentheses estimated from ratios as in ref. S, below. Other figures are averages of recent determinations.

R = allowed only in Raman, all species.

r = allowed only in Raman, symmetric species; allowed in infrared asymmetric species.

* = forbidden in Raman and infrared, symmetric species; allowed only in Raman, asymmetric species.

\- = forbidden in Raman and infrared, all species.

Columns 5-13 — In the isotopic species identification code, ten should be added to each digit to get the molecular weight of oxygen, carbon, and oxygen, respectively.

The figures in ( ) are the zero-point energies of the ground states. Other energies are referenced to this.

Observed levels are underscored; if solid, as transitions from ground; if dashed, as "hot bands".

In general, the latest of the following references have been used when several are available; others are estimated.

C = Courtoy (1957, 1959); S = Stull, Wyatt, & Plass (1963); E = Berney & Eggers (1964); G = Gordon & McCubbin (1966); D = Drayson & Young (1967); x = Chackerian & Eggers (1968); ϕ = Oberly et al. (1968); B = Benedict & Watson (1968).

Other

Remaining CO_2 species:	727	738	737	646
Abundances :	$16. \times 10^{-8}$	1.8×10^{-8}	0.18×10^{-8}	radioactive
$01^{1}0$ Level :	662.0	640.8	643.2	632.21_C
$00^{0}1$ Level :	2332.	2254.	2265.	2225.53_C

NOTE ADDED IN PROOF: See Cihla & Chedin (1971) for a more recent compilation extending to higher energies, with spectroscopic constants, and with potential constants to the sixth power of the normal coordinates.

APPENDIX B: DEFINITIONS AND NOTATION

1. Introduction

This Appendix defines the quantities and units used in infrared absorption, reviews the standard notation for symmetry representation of CO_2 vibrations, and recommends consistent means for denoting Fermi-group vibrational states and isotopic species.

2. Absorption Units

For radiation of initial intensity I_o passing through a medium which reduces its intensity to I, the transmittance T and optical thickness τ are defined by

$$I/I_o = T = e^{-\tau}, \text{ giving } \tau = -\ell n\, T \qquad (B1)$$

In a gas, optical thickness equals the gas amount u, times an absorption coefficient $\varkappa$. The common units for u, atm-cm, require correction for temperature and for departures from the ideal-gas law, so that units of amagat-cm are more appropriate, where the amagat density ρ is defined below. From the molecular viewpoint, the optical thickness τ equals σ, the absorption cross-section per molecule, times N, the number of molecules in a 1-cm^2 column. Comparing the two expressions: $\tau = \varkappa u = \varkappa \rho L = \sigma N = sLn$ (L and n are path length and molecular density). From this, $\varkappa/s = n/\rho = 2.69 \times 10^{19}$ molecules-cm^{-3} ama^{-1}. This is also equal to N_A/V_o.

With induced absorption, we can write

$$\tau = (\varkappa + \varkappa' \rho)\rho L \tag{B2}$$

where $\varkappa$ is the "allowed absorptivity" and $\varkappa'$ is the "induced absorptivity"; the latter's contribution to τ is thus proportional to density squared. The units of $\varkappa$ and $\varkappa'$ are $cm^{-1}\ ama^{-1}$ and $cm^{-1}\ ama^{-2}$, respectively. The strength of a line or band, also called its integrated absorption, is $K + \rho K' = \int \varkappa(\nu)d\nu + \rho \int \varkappa'(\nu)d\nu$. The units of K and K', allowed strength and induced strength, are $cm^{-2}\ ama^{-1}$ and $cm^{-2}\ ama^{-2}$.

In planetary atmospheres, τ is called optical depth. At altitude h_o,

$$\tau(h_o) = \int_{h_o}^{h_m} [\varkappa(\rho, T)\ \rho(h) + \varkappa'(\rho, T)\ \rho^2(h)]\, dh \tag{B3}$$

where the integration is from h_o to the top of the atmosphere h_m, using the proper profile of ρ and T versus h.

3. Representation and Selection Rules

The CO_2 molecule is in the symmetry class $D_{h\infty}$, where the D_h denotes dihedral symmetry around the x-y plane (orienting the long axis along z), and the ∞ indicates the number of angles of rotational symmetry. In linear molecules, the representation of vibrational states is the same as in diatomic molecules, with Σ, Π, Δ, Φ, Γ, H,

I, K, . . . for 0, 1, 2, 3, 4, 5, 6, 7, . . . units of vibrational angular momentum ℓ.

The subscripts g or u are used to denote symmetry or antisymmetry with respect to inversion at the origin; a superscripted + or - indicates symmetry or antisymmetry with respect to a plane through the z-axis. The Σ^- occurs only in overtones of degenerate modes of molecules with four or more atoms. In discussing rotational lines of states with non-zero ℓ, the superscripts c and d are added for the odd and even rotational levels. If $\ell = 0$, the zero nuclear spin of O^{16} means that only even rotational levels appear in Σ_g^+ and only odd in Σ_u^+.

In this representation, the ground state is Σ_g^+ and the three fundamentals ν_1, ν_2, ν_3 are respectively Π_u, Σ_g^+, and Σ_u^+. The representations of higher states are formed by combination rules given in Tables 31 through 33 of Herzberg (1945), and are shown in Table 9.

For infrared transitions, one of the upper and lower states must have the subscript g and the other u. $\Delta\ell$ may be 0 or $\pm$ 1; in the former case, the rotational J must change by $\pm$ 1, giving rise to P and R branches, but no Q branch.* If $\Delta\ell = \pm 1$, $\Delta J = 0$ is also allowed

*Except that in hot bands between two Π, Δ, Φ, etc. states, a weak Q is allowed but usually obscured.

so a Q branch appears. Raman selection rules require that the upper and lower states be both g or both u. Since ΔJ may be 0, ± 1, or ± 2, there are five branches: Q, P and R, and O and S. In CO_2, these rules mean that the sum $v_2 + v_3$ must be odd for infrared activity and must be even for Raman activity.

4. Fermi-Group Notation

In polyatomic molecules, a standard condensed method of describing complex vibrations has been to list the quantum numbers for each vibration in the same sequence as the vibrations are numbered. If the molecule is linear (so that one or more of the vibrations are degenerate), the angular momentum quantum number for the degeneracy is superscripted to the appropriate vibration. Thus the 1956 cm^{-1} level of C_2H_2 (which has five normal modes) is labeled $0002^{0}1^{1}$.

Even though CO_2 has a strong Fermi resonance which mixes levels $v_1 v_2^{\ell} v_3$ and $(v_1 - 1)(v_2 + 2)^{\ell} v_3$, it had long been customary to assign increasing values of v_1 to increasing energies within a Fermi group. This was done because it was believed that the unperturbed levels had energies increasing with v_1, and the "adiabatic assumption" assured that the predominant component of the mixed wave function in the perturbed levels followed the same sequence. Thus, the Fermi Raman pair at 1285 and 1388 cm^{-1} was labeled $02^{0}0$ and $10^{0}0$.

The first belief was cast in doubt by an apparent irregularity in the isotopic dependence of the Fermi interaction term W_{12} (Courtoy, 1959). Further work by Amat and Pimbert (1956) revealed that the unperturbed $02^{0}0$ level was actually the higher. This proves to be the case in a number of other Fermi groups, but not in all. The unperturbed energy may decrease or increase with increasing v_1; it is even possible for the behavior not to be monotonic in larger groups.

As a result, several new terminologies have been proposed which do not attempt to imply a particular sequence of v_1. Oberly, Rao, Hahn, & McCubbin (1968) use parentheses around the old notation for the highest and lowest members of the group, and add a Roman numeral decreasing with energy. The lines at 4853, 4978, and 5100 cm^{-1} (old $04^{0}1$, $12^{0}1$, $20^{0}1$) become $(20^{0}1\ .\ .\ 04^{0}1)$III, $(20^{0}1\ .\ .\ 04^{0}1)$II, and $(20^{0}1\ .\ .\ 04^{0}1)$I.

A somewhat less unwieldy scheme was used by Burch, Gryvnak, & Patty (1967), who use the maximum value of v_1, the minimum of v_2, and v_3. A Roman numeral, as above, is used as subscript. The value of ℓ is not given separately, as it is the same as v_2. The above lines become 201_{III}, 201_{II}, and 201_{I}; the old $04^{2}1$ and $12^{2}1$ become 121_{II} and 121_{I}. Even single lines without Fermi resonance are relabeled: $03^{3}1$ becomes 031_{I}. The maximum value of v_2 is inferred from $2v_1 + v_2$.

The lack of an explicit ℓ proved to be a disadvantage, and the earlier schemes have been partially supplanted by one used by Benedict & Wattson (1969). In this, the value of ℓ is given after a comma: $03^{3}1$ becomes $(031, 3)_{I}$. Some authors omit the parentheses.

These three schemes all have certain disadvantages. First, the Roman numerals move in the opposite direction with respect to energy than do the quantum numbers; this is a consequence of using the maximum value of v_1 to designate the group. Second, lines with the same values of all quantum numbers except ℓ look quite different: $13^{1}0$ and $13^{3}0$ become 211_{II} and 130_{I}. Third, a drastic break is made with the well-known notation used not only with CO_2 but with many other molecules.

The notation used herein attempts to use the positive features of the various proposals, but without their disadvantages. First, the maximum value of v_2 is used to designate the group, with the usual ℓ superscript. The corresponding (minimum) value of v_1 is zero, so it can be omitted for brevity. This makes it logical for the Roman numeral, used only in groups, to increase with energy. Omitting the Roman numeral is an easy way to identify an entire group. The standard notation is used for single levels without Fermi resonance, and for the unperturbed levels in Fermi-resonant groups.

The result is a notation which bears a definite resemblance to the standard notation, does not require relabeling of unperturbed levels or those not in Fermi groups, shows when levels are in groups by omitting the redundant v_1, requires no more symbols than the standard notation, has a logical progression of Roman numerals with energy, distinguishes between unperturbed and perturbed levels, and provides a convenient shorthand for a whole group.

Examples of its use are given in Table 3, in Table 9 (Appendix A), and in Table 10, below, which compares it with the other proposed notations.

TABLE 10: NOTATION COMPARISON

Level, cm^{-1}	Old	Oberly et al.	Burch et al.	Benedict	Herein
3181	$05^{1}0$	$(21^{1}0. . 05^{1}0)$III	210_{III}	(210, 1)III	$5^{1}0$, I
3339	$13^{1}0$	$(21^{1}0. . 05^{1}0)$II	210_{II}	(210, 1)II	$5^{1}0$, II
3500	$21^{1}0$	$(21^{1}0. . 05^{1}0)$I	210_{I}	(210, 1)I	$5^{1}0$, III
3241	$05^{3}0$	$(13^{3}0, 05^{3}0)$II	130_{II}	(130, 3)II	$5^{3}0$, I
3443	$13^{3}0$	$(13^{3}0, 05^{5}0)$I	130_{I}	(130, 3)I	$5^{3}0$, II
3341	$05^{5}0$	$05^{5}0$	050_{I}	(050, 5)I	$05^{5}0$

5. Isotopic Species

A compact notation has been proposed (Benedict, 1971) for isotopic species of simpler molecules. It gives the last digit of the atomic weight of each atom, in a sequence corresponding to its position in the molecule (e.g.: HOH, OCO, etc.). For diatomic or non-linear molecules, the order is that of the usual chemical symbol. Thus heavy water is 262, $C^{12}O^{16}O^{18}$ is 628, HCl^{35} is 15, partially deuterated ammonia is 4211.

In cases where confusion might arise, different elements may be set off by a comma. Thus, half-deuterated methane and acetylene are 2, 2211 and 22, 21. Though the system becomes unwieldy for more complex molecules, it is a considerable convenience for many common gases.

APPENDIX C: VALENCE-MODEL MATRIX ELEMENTS

1. Model and Assumptions

We wish to compare the matrix elements for the 10^00 and 02^00 transitions. These correspond to $(\partial\alpha/\partial\xi_1)_{\xi_1}$ and $(\partial^2\alpha/\partial\xi_2^2)_{\xi_2^2}$. Since there are no cross-derivatives, each motion can be treated separately. The molecular axis lies in the z-direction. Constants are as given in Appendix A, part 6.

2. Polarizability Components and Derivatives

For a field $E_\perp$ in the x- or y-direction, consider the molecule bent at an angle θ and with a C-O distance of R. The force on the oxygen atoms leads to a torque $(qE_\perp)(R\cos\theta) = k_\theta \Delta\theta$, where the additional bend is $\Delta\theta = \Delta x/R\cos\theta$. The increment in the dipole moment is $\mu_\perp = 2q\Delta x$ (where $\Delta x = \Delta x_1/2 + \Delta x_3/2$), so that the polarizability $\alpha_\perp = \mu_1/E_\perp = 2q^2R^2\cos^2\theta/k_\theta$.

The derivative with respect to the ν_1 normal mode is

$$\frac{\partial\alpha_\perp}{\partial\xi_1} = \sum_i^3 \frac{\partial\alpha_\perp}{\partial z_i} \Bigg/ \frac{\partial\xi_1}{\partial z_i}$$

where z_i are the displacements of the three atoms. Since $\xi_1 = z_1 - z_3$, the mode derivatives are $\xi'_{11} = 1$, $\xi'_{12} = 0$, $\xi'_{13} = -1$. The ν_2 mode is ignored by setting $\theta = 0$, $R = L + z_1 = -L - z_3$. This

gives

$$\frac{\partial \alpha_\perp}{\partial z_1} = \frac{2q^2}{(k_\alpha / L^2)L} = -\frac{\partial \alpha_\perp}{\partial z_3} \quad ,$$

so that

$$\frac{\partial \alpha_\perp}{\partial \xi_1} = \frac{4q^2}{(k_\theta / L^2)L} \quad ;$$

where we have set $z = 0$ for equilibrium.

The derivative with respect to the ν_2 normal mode is obtained similarly, with $\xi_2 = x_2 - (x_1 + x_3)m/M$. The mode derivatives are $\xi'_{21} = \xi'_{23} = -m/M$, $\xi'_{22} = 1$.

To ignore ν_1, set $R = L$, and note that $\Delta x = \Delta x_2 - (\Delta x_1 + \Delta x_3)/2$. Then

$$\frac{\partial \alpha_\perp}{\partial x_1} = \frac{\partial \alpha_\perp}{\partial x_3} = \frac{q^2 L \sin\theta}{k_\theta}$$

and

$$\frac{\partial \alpha_\perp}{\partial x_2} = \frac{2q^2 L \sin\theta}{k_\theta} \quad .$$

This gives

$$\frac{\partial \alpha_\perp}{\partial \xi_2^2} = \frac{4q^2 L \sin\theta}{k_\theta} \left(1 + \frac{M}{m}\right) \quad .$$

This is zero at equilibrium, which is to be expected from the fact that the ν_2 fundamental is infrared active, not Raman active.

Repeating the process to get the second derivative,

$$\frac{\partial^2 \alpha_\perp}{\partial \xi_2^2} = \frac{4q^2}{k_\theta} \left(1 + \frac{M}{m}\right)^2 .$$

For a field $E_{||}$ in the z-direction, the force on either oxygen atom is $Eq = k_1(z - z_2) \cos^2\theta$. The induced dipole along the z-axis is $2q(z - z_2)$, so the polarizability is $\alpha_{||} = \partial \mu_{||} / \partial E_{||} = 2q^2/k_1 \cos^2\theta$. This is independent of z, so its derivative with respect to ξ_1 is zero.

Following the above procedure, we find

$$\frac{\partial \alpha_{||}}{\partial \xi_2} = \frac{4q^2 \sin\theta}{Lk_1 \cos^4\theta} \left(1 + \frac{M}{m}\right)$$

which is again zero at equilibrium. The second derivative is

$$\frac{\partial^2 \alpha_{||}}{\partial \xi_2^2} = \frac{4q^2}{L^2 k_1} \left(1 + \frac{M}{m}\right)^2$$

at equilibrium.

The averaged values are the sum of the squares of the components, with the perpendicular weighted twice as heavily. The result is $\partial\alpha/\partial \xi_1 = 5.04 \times 10^{-17}$ cm^2 and $\partial^2\alpha/\partial \xi_2^2 = 4.36 \times 10^{-9}$ cm. Since this analysis assumes the charge is centered on the nuclei, it refers only to atomic polarizability, not electronic polarizability.

3. Matrix Elements

Evaluating the matrix elements, each derivative must be multiplied by the appropriate power of its normal coordinate and integrated between the ground state and the excited states $\psi_{10^0 0}$ and $\psi_{02^0 0}$, respectively. Using the results of Appendix E, we have: $A = 2.00 \times 10^{-26}$ cm^3 and $B = 1.78 \times 10^{-27}$ cm^3, for a ratio of $A/B = 11.2$.

It must be recognized that this comparison is based only on the atomic polarizability. Nevertheless, it suggests an explanation for higher-order matrix elements of the total derivative being smaller than those of lower order.

Let us examine the effect of an additional differentiation. There will be a moderate change in the numerical constants, but an additional power of the length $L = 1.16 \times 10^{-8}$ cm appears in the denominator. When the higher-order matrix element is formed, an additional power of a normal coordinate appears in the dipole term and in the Hermite polynomial. The latter brings in a normalization whose size is the same magnitude as the vibrational displacement: for CO_2, near 6×10^{-10} cm. Thus it is not surprising if each increase in the order of the matrix element decreases its size by an order of magnitude, unless symmetry causes a term to be zero.

Another viewpoint is to consider the extent to which the electron cloud can be shifted by an external field if the atoms are not in the equilibrium linear position. If the molecule is symmetrically stretched, the two portions of the cloud between the carbon and oxygen (the regions containing most of the 2p bonding electrons) will be further from the nuclei, the ratio between the nuclear field and an external field will decrease, and they will be more readily polarizable. The 1s and 2s electrons will be relatively unaffected.

On the other hand, if the molecule is bent, the nuclear spacing is unchanged, and the bonding region will be unaffected. Near the carbon, those of the 2p electrons inside the bend angle will be further from the nucleus and thus more polarizable - - but those outside the bend will be closer and less polarizable.

Putting it more simply, Brand and Sparkman (1960) state that electronic polarizability (the major contributor to total polarizability) depends strongly on bond length, which changes only with ξ_1.

APPENDIX D: MECHANICAL ANHARMONICITY

Overtone and combination lines can arise from mechanical anharmonicity (deviation of the potential from the form $k\xi^2$) as well as from electrical non-linearity (higher-order terms in the Taylor-series expansion of the dipole moment or the polarizability). In the present study, all the induced strength of the bands at 4248 and 4391 cm^{-1} has been ascribed to the last of these. To verify that mechanical anharmonicity can safely be ignored, a brief discussion follows.

Expanding the polarizability to order λ^3, many terms are zero because of the symmetry of the CO_2 molecule. Those which remain are:

$$\alpha = \alpha_0 + \lambda\alpha'_1\xi_1 + \lambda^2\left[\alpha''_{23}\xi_2\xi_3 + \frac{1}{2}\left(\alpha''_{11}\xi_1^2 + \alpha''_{22}\xi_2^2 + \alpha''_{33}\xi_3^2\right)\right]$$

$$+ \lambda^3\left[\alpha'''_{123}\xi_1\xi_2\xi_3 + \frac{1}{2}\left(\alpha'''_{122}\xi_1\xi_2^2 + \alpha'''_{133}\xi_1\xi_3^2\right) + \frac{1}{6}\alpha'''_{111}\xi_1^3\right] \quad \text{(D1)}$$

If the time-dependent normal coordinates are expanded as in Herzberg, p. 205 (1945), assigned powers of λ to indicate their order, and inserted in (D1), the only term giving a frequency of ω_1 (corresponding to the Raman-allowed or collision-induced unperturbed transition $00^00\text{-}10^00$) that is of lower order than λ^3 is*

* In this and other time-dependent expressions, an additional subscript has been added before the comma to indicate which normal coordinate's expansion the η comes from, as Herzberg's notation is ambiguous. For brevity, phase is omitted. Powers of λ are not grouped, but are written adjacent to the term in which they originally appeared, in order to show their origin.

$\lambda\alpha_1'\eta_{1,100}\cos(\omega_1 t)$, which has no anharmonic components. Similarly, most of the induced transitions with total quantum number change of 2 have only the harmonic term of lower order than λ^4:

$$\left.\begin{matrix} 00^00\text{-}02^00 \\ 00^00\text{-}02^20 \end{matrix}\right\} \text{ frequency } 2\omega_2: \quad \frac{\lambda^2}{2}\alpha_{22}''\left(\eta_{2,010}\cos(\omega_2 t)\right)^2$$

$$00^00\text{-}00^02, \quad \text{frequency } 2\omega_3: \quad \frac{\lambda^2}{2}\alpha_{33}''\left(\eta_{3,001}\cos(\omega_3 t)\right)^2$$

$$00^00\text{-}01^11; \quad \text{frequency } \omega_2+\omega_3: \quad \lambda^2\alpha_{23}''\eta_{2,010}\cos(\omega_2 t)\eta_{3,001}\cos(\omega_3 t)$$

However, the induced transition $00^00\text{-}20^00$ with frequency $2\omega_1$ has two terms, the second with mechanical anharmonicity:

$$\frac{\lambda^2}{2}\alpha_{11}''\left(\eta_{1,100}\cos(\omega_1 t)\right)^2 + \lambda\alpha_1'\lambda\eta_{1,200}\cos(2\omega_1 t)$$

In the case of the $00^00\text{-}11^11$ induced transition, the relevant frequency is $\omega_1+\omega_2+\omega_3$, and there are four terms of lower order than λ^5:

$$\begin{aligned} &\lambda^3\alpha_{123}'''\eta_{1,100}\cos(\omega_1 t)\cdot\eta_{2,010}\cos(\omega_2 t)\cdot\eta_{3,001}\cos(\omega_3 t) \\ &+\lambda^2\alpha_{23}''\lambda\eta_{2,110}\cos(\omega_1 t)\cos(\omega_2 t)\cdot\eta_{3,001}\cos(\omega_3 t) \\ &+\lambda^2\alpha_{23}''\eta_{2,010}\cos(\omega_2 t)\cdot\eta_{3,101}\cos(\omega_1 t)\cos(\omega_3 t) \\ &+\lambda\alpha_1'\lambda^2\eta_{1,111}\cos(\omega_1 t)\cos(\omega_2 t)\cos(\omega_3 t) \end{aligned} \qquad \text{(D2)}$$

The first term is harmonic, has been treated in section V. B., and will be called P_h; the last requires a term in the CO_2 potential

function of the form $k\xi_1^2\xi_2\xi_3$, which is zero by symmetry. In the second and third terms, $\eta_{2,110}$ stems from $73.9\xi_1\xi_2^2$ in the potential function, and $\eta_{3,101}$ from $-251\xi_1\xi_3^2$.

Parenthetically, it should be noted that mechanically anharmonic terms with frequency $2\omega_2$ or $2\omega_3$ might conceivably arise from the dipole moment. Again allowing for symmetry, the expansion is:

$$\mu = \mu_0 + \lambda\left(\mu_2'\xi_2 + \mu_3'\xi_3\right) + \lambda^2\left(\mu''_{12}\xi_1\xi_2 + \mu''_{13}\xi_1\xi_3\right)$$
$$+ \lambda^3\left[\frac{1}{2}\left(\mu'''_{112}\xi_1^2\xi_2 + \mu'''_{113}\xi_1^2\xi_3 + \mu'''_{222}\xi_2^2\xi_3 + \mu'''_{233}\xi_2\xi_3^2\right)\right.$$
$$\left. + \frac{1}{6}\left(\mu'''_{222}\xi_2^3 + \mu'''_{333}\xi_3^3\right)\right] \qquad \text{(D3)}$$

Inserting the normal coordinates as before, the terms leading to $2\omega_2$ and $2\omega_3$ are $\lambda\mu_2'\lambda\eta_{2,020}\cos(2\omega_2 t)$ and $\lambda\mu_3'\lambda\eta_{3,002}\cos(2\omega_3 t)$, respectively. However, they require terms in the potential function of the form $k\xi_2^3$ and $k\xi_3^3$, both zero by symmetry. Likewise, there are six terms from (D3) which lead to frequency $\omega_1 + \omega_2 + \omega_3$, but they also stem from terms in the potential which are zero by symmetry. If any mechanically anharmonic terms from (D2) were not zero, they would not require an inducing field, and would thus be proportional to density. Not only is such proportionality not observed except for asymmetric species (see section VII. A; Mannik, McKellar, Rich, & Stryland, 1970; Burch, Gryvnak, & Pembrook, 1970), but it would violate the rule that a transition which is

forbidden in the harmonic approximation does not become allowed if anharmonicity is added.

Returning to the remaining terms in (D2), we can determine their importance by solving for the time-dependent normal coordinates, using a first-order pertubation approach as in Baldwin (1967). We find:

$$\xi_2(t) = \eta_{2,010}\left[\cos(\omega_2 t) + 73.9\lambda\eta_{1,100}\left(\frac{\cos(\omega_1+\omega_2)t}{\omega_1^2+2\omega_1\omega_2} + \frac{\cos(\omega_1-\omega_2)t}{\omega_1^2-2\omega_1\omega_2}\right)\right]$$

$$\xi_3(t) = \eta_{3,001}\left[\cos(\omega_3 t) - 251\,\lambda\eta_{1,100}\left(\frac{\cos(\omega_1+\omega_3)t}{\omega_1^2+2\omega_1\omega_3} + \frac{\cos(\omega_3-\omega_1)t}{\omega_1^2-2\omega_1\omega_3}\right)\right]$$

Inserting these in (D1), the two mechanically anharmonic terms with frequency $\omega_1+\omega_2+\omega_3$ are

$$P_{m1} = \lambda^2\alpha''_{23}\frac{\eta_{2,010}\,73.9\lambda\eta_{1,100}}{\omega_1^2+2\omega_1\omega_2}\eta_{3,001} \quad \text{and} \quad P_{m2} = -\lambda^2\alpha''_{23}\eta_{2,010}\frac{\eta_{3,001}\,251\,\eta_{1,100}}{\omega_1^2+2\omega_1\omega_3}$$

Their contribution to the transition probability compared to that of the harmonic term P_H, is

$$\frac{P_{m1}^2 + P_{m2}^2}{P_h^2} = \left(\frac{\alpha''_{23}}{\alpha'''_{123}}\right)^2\left[\left(\frac{73.9}{3.58\times10^6}\right)^2 + \left(\frac{251}{8.07\times10^6}\right)^2\right]$$

Not only is the numerical factor small, but the second derivative is orders of magnitude smaller than the third. Neglect of mechanical anharmonicity is thus justified. Dunham (1930) reached a similar conclusion with HCl, after a more rigorous analysis.

APPENDIX E:

DEGENERATE EIGENFUNCTIONS AND HOT BAND STRENGTHS

1. *Radial Eigenfunctions*

The effects of degeneracy in ℓ must be considered when evaluating CO_2 matrix elements. While Hermite polynomials are the appropriate eigenfunctions for those transitions involving changes in quantum numbers of ν_1 or ν_3, both non-degenerate, they are only applicable to the degenerate ν_2 if the x and y components are treated separately. This is not as convenient as forming new eigenfunctions which are linear combinations of the components; see p. 81, Herzberg (1945).

Consider the case where ν_2 has one quantum of excitation. This can appear in either the x or the y component; the other will be unexcited. The eigenfunctions are, in dimensionless normal coordinates (where the subscripts on ψ indicate the quantum numbers of ν_{2x} and ν_{2y}, respectively):

$$\psi_{10} = 2^{-\frac{1}{2}} \pi^{-\frac{1}{4}} e^{-\xi_{2x}/2} 2\xi_{2x} \cdot \pi^{-\frac{1}{4}} e^{-\xi_{2y}/2}$$

$$\psi_{01} = \pi^{-\frac{1}{4}} e^{-\xi_{2x}/2} \cdot 2^{-\frac{1}{2}} \pi^{-\frac{1}{4}} e^{-\xi_{2y}/2} 2\xi_{2y}$$

With $x = \rho \cos\phi$, $y = \rho \sin\phi$, an obvious linear combination is

$$\psi_1^{\pm 1} = \frac{1}{\sqrt{2}} (\psi_{10} \pm i\psi_{01}) = \frac{1}{\sqrt{\pi}} e^{-\rho^2/2} \rho e^{\pm i\phi} \qquad \text{(E1)}$$

where the last exponential indicates an angular momentum with two possible directions.

The combined ground state is simply the product

$$\psi_0^0 = \psi_{00} = \pi^{-\frac{1}{2}} e^{-\xi_{2x}/2} \cdot \pi^{-\frac{1}{4}} e^{-\xi_{2y}/2} = \frac{1}{\sqrt{\pi}} e^{-\rho^2/2} \quad .$$

For two units of excitation, the x and y quantum numbers can be 2 and 0, 1 and 1, or 0 and 2. The appropriate linear combinations are

$$\psi_2^{\pm 2} = \frac{1}{2}(\psi_{20} - \psi_{02} \pm \sqrt{2}\, i\psi_{11}) \quad \text{and} \quad \psi_2^0 = \frac{1}{\sqrt{2}}(\psi_{20} + \psi_{02}) \, . \qquad \text{(E2)}$$

Similarly, the combinations for the next level are

$$\psi_3^{\pm 3} = \frac{1}{\sqrt{8}} (\psi_{30} \mp i\psi_{03} - \sqrt{3}\, \psi_{12} \pm \sqrt{3}\, i\psi_{21}) \qquad \text{(E3a)}$$

and $$\psi_3^{\pm 1} = \frac{1}{\sqrt{8}} (\sqrt{3}\, \psi_{30} \pm \sqrt{3}\, i\psi_{03} + \psi_{12} \pm i\psi_{21}) \, . \qquad \text{(E3b)}$$

Table 11: NORMALIZED RADIAL POLYNOMIALS FOR $\psi_n^{\pm \ell}$

	$\ell=0$	1	2	3	4	5	6
n=0	$1/\sqrt{\pi}$						
n=1		$\rho/\sqrt{\pi}$					
n=2	$(\rho^2-1)/\sqrt{\pi}$		$\rho^2/\sqrt{2\pi}$				
n=3		$(\rho^3-2\rho)/\sqrt{2\pi}$		$\rho^3/\sqrt{6\pi}$			
n=4	$(\rho^4-4\rho^2+2)/\sqrt{4\pi}$		$(\rho^4-3\rho^2)/\sqrt{6\pi}$		$\rho^4/\sqrt{24\pi}$		
n=5		$(\rho^5-6\rho^3+6\rho)/\sqrt{12\pi}$		$(\rho^5-4\rho^3)/\sqrt{24\pi}$		$\rho^5/\sqrt{120\pi}$	
n=6	$(\rho^6-9\rho^4+18\rho^2-6)/\sqrt{36\pi}$		$(\rho^6-8\rho^4+12\rho^2)/\sqrt{48\pi}$		$(\rho^6-5\rho^5)/\sqrt{120\pi}$		$\rho^6/\sqrt{720\pi}$

The explicit form of the first sixteen normalized radial polynomials is given in Table 11. They should be multiplied by $e^{-\rho^2/2}\, e^{\pm i\ell\phi}$, which has been omitted for brevity.

These have been related to the associated Laguerre polynomials by, for example, Shaffer (1941); including normalization, a more direct expression is

$$\psi_n^{\pm\ell} = \frac{e^{-\rho^2/2}\, e^{\pm i\ell\phi}}{\sqrt{\pi\left(\frac{n+\ell}{2}\right)!\left(\frac{n-\ell}{2}\right)!}} \sum_{p=0} \frac{(-)^p\, \rho^{n-2p}\left(\frac{n+\ell}{2}\right)!\left(\frac{n-\ell}{2}\right)!}{p!\left(\frac{n+\ell-2p}{2}\right)!\left(\frac{n-\ell-2p}{2}\right)!} \qquad \text{(E4)}$$

In order for the series to terminate, ℓ is restricted to the values n, n-2, n-4, ... 0 or 1.

To obtain transition probabilities, the squared matrix elements must be summed over the x and y components. Table 12 gives the values of

$$\left\langle \psi_{n_1}^{\ell_1} \middle| x^{n_2-n_1} \middle| \psi_{n_2}^{\ell_2} \right\rangle^2 + \left\langle \psi_{n_1}^{\ell_1} \middle| y^{n_2-n_1} \middle| \psi_{n_2}^{\ell_2} \right\rangle^2$$

for a few cases. The entries in Table 12 must be multiplied by the appropriate power of the coordinate normalization (Appendix A, Section 6), but the statistical weights due to degeneracy can be taken directly from the table by recalling that the energy of a level depends on the absolute value of ℓ but not on its sign.

Table 12: RADIAL TRANSITION PROBABILITIES

Based on Squared Matrix Elements of $x^{n_2-n_1}$ and $y^{n_2-n_1}$

LOWER n_1	LOWER ℓ_1	UPPER n_2	1		2			3			
		UPPER ℓ_2	-1	+1	-2	0	+2	-3	-1	+1	+3
0	0		1/2	1/2	1/4	1/2	1/4	3/16	9/16	9/16	3/16
1	-1				1	1/2	0	3/4	1	1/4	0
	+1				0	1/2	1	0	1/4	1	3/4
2	-2							3/2	1/2	0	0
	0							0	1	1	0
	+2							0	0	1/2	3/2

It is interesting to note that the selection rules appear as a result of the integration over ϕ, rather than from symmetry over the length coordinate, as is the case with Hermite polynomials. One consequence is that a given transition is affected not only by the matrix elements of the n_2-n_1 power of the normal coordinates, but also by the higher powers n_2-n_1+2, n_2-n_1+4, etc.

The values in Table 12 may be compared with the corresponding transition probabilities for the one-dimensional harmonic oscillator (using Hermitian polynomials), where

$$\left\langle \psi_{n_1} \left| x^{n_2 - n_1} \right| \psi_{n_2} \right\rangle^2 = \frac{n_2!}{n_1!\, 2^{n_2 - n_1}}$$

It is interesting to note that this formula leads to the correct values if used -- improperly -- for the $0^0\text{-}1^1$ and $0^0\text{-}2^0$ transitions, but is otherwise generally incorrect for degenerate transitions.

2. Hot Band Relative Strengths

Using the foregoing, the ratio of strengths between a hot band and the transition from ground with the same change in quantum numbers can be calculated. Though the discussion which follows applies to CO_2 hot bands, the principles apply generally.

First, consider transitions of the form $00^00\text{-}v_1 0^0 v_3$, with a non-degenerate upper level. The corresponding hot band is $01^10\text{-}v_1 1^1 v_3$, where the same matrix elements apply to ν_1, ν_2 (unity), and ν_3 in both cases; the hot band is degenerate in ℓ. On the other hand, both may be degenerate, as in the case of a transition of the form $00^00\text{-}v_1 1^1 v_3$, with the corresponding hot bands $01^10\text{-}v_1 2^0 v_3$ and $01^10\text{-}v_1 2^2 v_3$. For completeness, a case with $\Delta\ell = 2$ and one with a non-degenerate lower level may be considered. These are listed in Table 13, which includes the weighting factors for degeneracy.

Table 13: HOT BAND RELATIVE STRENGTHS

Transitions from Ground	Corresponding Hot Transitions	Strength Ratio $K_{hot}/K_0 B^*$
$00^00\text{-}v_1 0^0 v_3$	$01^10\text{-}v_1 1^1 v_3$	2
$00^00\text{-}v_1 1^1 v_3$	$01^10\text{-}v_1 2^0 v_3$	1
	$01^10\text{-}v_1 2^2 v_3$	2
$00^00\text{-}v_1 2^2 v_3$	$01^10\text{-}v_1 3^1 v_3$	5
	$01^10\text{-}v_1 3^3 v_3$	3
$00^00\text{-}v_1 v_2^{\ell} v_3$	$10^00\text{-}(v_1+1) v_2^{\ell} v_3$	(v_1+1)

In CO_2, the next-to-last line is allowed in the Raman effect or in induced absorption; other cases with $\ell < v_2$ need not be considered, as they are members of Fermi multiplets whose strength is dominated by the term with largest v_1.

---

* B is the Boltzmann population factor for the lower level in the hot transition (different in the last case).

X. REFERENCES

	Mentioned on pages:
Adel, A.; Slipher, V. M. "The Constitution of the Atmospheres of the Giant Planets" Phys. Rev. 46, 902-906 (1934).	22
Amat, G.; Pimbert, M. "On Fermi Resonances in Carbon Dioxide" Jnl. Molec. Spectr. 16, 278-290 (1965).	46, 105
Anding, David. "Band-Model Methods for Computing Atmospheric Slant-Path Molecular Absorption" Rpt. 7142-21-T, Willow Run Labs., U. of Mich., Ann Arbor (1967).	66
Armstrong, Kendall. (Rice University) Private communication (1971).	78
Avduevsky, V. S.; Marov, M. Ya.; Rozhedestvensky, M. K. "A Tentative Model of the Venus Atmosphere Based on the Measurements of Venera 5 and 6" Jnl. Atmos. Sci., 27, 561-568 (1970).	61, 68
Benedict, William S. Private communication (1971).	30, 108
Benedict, William S.; Wattson, Richard. Listing of vibrational constants, hot bands, and intensities for $C^{12}O_2^{16}$. Unpublished (1969).	54, 64, 67, 93, 106, 107
Berney, Charles V.; Eggers, Jr., David F. "Infrared Spectrum of Carbon Dioxide, Enriched in Oxygen 18" Jnl. Chem. Phys. 40, #4, 990-1000 (1964).	100
Birnbaum, George. "The Shape of Collision Broadened Lines Near Resonance and in the Far Wings" Phys. Rev., to be published.	42, 63
Brand, John C. D.; Sparkman, James C. Molecular Structure E. Arnold, London (1960).	52, 95, 113
Burch, Darrell E. Private communication (1971).	37
Burch, Darrell E.; Gryvnak, David A.; Patty, Richard R. "Absorption by CO_2 Between 4500 and 5400 cm^{-1}" Pub. #U-2955, Philco-Ford Aeronutronic Div., Newport Beach, Cal. (Dec. 1964).	27, 37, 67
_____. "Absorption by CO_2 Between 6600 and 7125 cm^{-1}" Pub. #U-3127 Philco-Ford Aeronutronic Div., Newport Beach, Cal. (June 1965, A).	27

_____. "Absorption by CO_2 Between 8000 and 10,000 cm^{-1}" Pub. #U-3200, Philco-Ford Aeronutronic Div., Newport Beach, Cal. (6 Aug. 1965, B). 27, 54, 68

_____. "Absorption by CO_2 Between 5400 and 6600 cm^{-1}" Pub. #U-3201, Philco-Ford Aeronutronic Div., Newport Beach, Cal. (31 Aug. 1965, C). 27

_____. "Absorption by CO_2 Between 7125 and 8000 cm^{-1}" Pub. #U-3930, Philco-Ford Aeronutronic Div., Newport Beach, Cal. (1967). 27, 68, 105, 107

_____. "Absorption by CO_2 Between 3100 and 4100 cm^{-1}" Pub. #U-4132, Philco-Ford Aeronutronic Div., Newport Beach, Cal. (1968). 27, 37, 38, 52, 54, 67

Burch, Darrell E.; Gryvnak, David A.; Patty, Richard R.; Bartky, Charlotte E. "The Shapes of Collision-Broadened CO_2 Lines" Pub. #U-3203, Philco-Ford Aeronutronic Div., Newport Beach, Cal. (1968). 56, 57, 63, 91

Burch, Darrell E.; Gryvnak, David A.; Pembrook, John D. "Investigation of the Absorption of Infrared Radiation by Atmospheric Gases" Pub. #U-4829, Philco-Ford Aeronutronic Div., Newport Beach, Cal. (1970). 38, 39, 45, 46, 51, 67, 116

Burch, Darrell E.; Gryvnak, David A.; Singleton, Edgar B.; France, Wilbur L.; Williams, Dudley. "Infrared Absorption by Carbon Dioxide, Water Vapor, and Minor Atmospheric Constituents" OSU Research Report on Proj. 8603, Ohio State U. (1962). 39, 66

Chackerian, Jr., Charles; Eggers, Jr., David F. "The Infrared Spectrum of $^{12}C^{18}O_2$" Jnl. Molec. Spectr. 27, 59-71 (1968). 100

Chandrasekhar, S. Radiative Transfer Dover Pubs., New York (1960). 70

Cihla, Z.; Chedin, A. "Potential Energy Function of Polyatomic Molecules: Fourth-Order Approximation to the Potential Energy Function of CO_2: Spectroscopic Constants of Nine Isotopic Species" Jnl. Molec. Spectr. 40, 337-355 (1971). 93, 95, 100

Condon, E. U. "Production of Infrared Spectra with Electric Fields" Phys. Rev. 41, 759-762 (1932). 90

Courtoy, Charles-Pierre "Spectres de Vibration-Rotation... avec Long Parcours d'Absorption: XII Le Spectre de $C^{12}O_2^{16}$ Entre 3500 et 8000 cm^{-1}..." Canadian Jnl. Phys. 35, 608-648 (1957). 100

_____. "Spectre Infrarouge a Grande Dispersion et Constantes Moleculaires du CO_2" Annales de la Societe Scientifique de Bruxelles 73, #1, 5-230 (1959). 100, 105

Dennison, David M. "The Infrared Spectra of Polyatomic Molecules, Part II" Rev. Mod. Phys. 12, #3, 175-214 (1940). 93, 95

Diamante, John M. "The Structure and Circulation of the Lower Atmosphere of Venus" Ph. D. Thesis, New York University (1969). 72

Dole, Stephen H. "The Atmosphere of Venus" Rand Report P-978, Rand Corporation, Santa Monica, Cal. (1956). 59

Drayson, S. R.; Young, C. "The Frequencies and Intensities of Carbon Dioxide Absorption Lines Between 12 and 18 Microns" Rpt. #08183-1-T, University of Michigan, Ann Arbor (1967). 100

Dunham, J. L. "Intensities of Vibration-Rotation Bands with Special Reference to Those of HCl" Phys. Rev. 35, 1347-1354 (1930). 117

Fahrenfort, Jacob. "The Infrared Absorption Spectrum of Compressed CO_2 and CO_2-Containing Gas Mixtures" Ph. D. Thesis, University of Amsterdam, pub. Wolters, Groningen, Neth. (1955). 34, 37, 38, 46, 51, 52, 54, 95

Fermi, Enrico. "Über den Ramaneffekt des Kohlendioxyds" Zeit. für Physik 71, 250-259 (1931). 92

Gaizauskas, V. "Studies of the Infrared and Raman Spectra of Gaseous Liquid and Solid Carbon Dioxide" Ph. D. Thesis, University of Toronto (1955). 37

Gillett, F. C.; Low, F. J.; Stein, W. A. "Absolute Spectrum of Venus from 2.8 to 14 Microns" in The Venus Atmosphere 279-282, eds. Jastrow & Rasool, Gordon & Breach, N. Y. (1969). 78, 79

Gordon, Howard R.; McCubbin, Jr., T. K. "The 2.8 Micron Bands of CO_2" Jnl. Molec. Spectr. 19, 137-154 (1966). 45, 100

Gryvnak, David A.; Patty, Richard R.; Burch, Darrell E.; Miller, Earl E. "Absorption by CO_2 Between 1800 and 2850 cm^{-1}" Pub. #U-3857, Philco-Ford Aeronutronic Div., Newport Beach, Cal. (1966). 27, 38, 67

Hanel, R.; Forman, M.; Stambach, G.; Meilleur, T. "Preliminary Results of Venus Observations Between 8 and 13 Microns" in The Venus Atmosphere, 257-278, eds. Jastrow & Rasool, Gordon & Breach, N. Y. (1969). 78, 79

Herzberg, Gerhard. Molecular Spectra and Molecular Structure: II Infrared & Raman Spectra of Polyatomic Molecules D. Van Nostrand Co., Inc., Princeton, N. J. (1945). 47, 55, 95, 103, 114

Ho, William; Birnbaum, G.; Rosenberg, A. "Far-Infared Collision-Induced Absorption in CO_2: I. Temperature Dependence" Jnl. Chem. Phys. 55, #3, 1028-1038 (1971). 62, 63, 64, 69, 74, 95

Low, Frank J. Private communication (1971). 78

Low, Manfred J. D. Private communication (1971). 66

McAdams, William H. Heat Transmission 186, McGraw-Hill, N. Y. (1954). 12

MacCormack, K. E.; Schneider, W. G. "Compressibility of Gases at High Temperatures. IV. Carbon Dioxide in the Temperature Range 0°-600° C, and Pressures up to 50 Atmospheres" Jnl. Chem. Phys. 18, #9, 1269-1272 (1950). 39

Mannik, L.; McKellar, A. R. W.; Rich, N.; Stryland, J. C. "The Anomalous Density Dependence of the ν_1 Bands of Carbon Dioxide in Pressure-Induced Absorption" Jnl. Chem. Phys. 48, #1, 95-98 (1970). 116

Marov, M. Ya. "First Results from Venera 7 on the Venus Atmosphere" NASA Colloquium, Goddard Institute for Space Studies, N. Y. (Feb. 4, 1971). 61

Michels, A.; Michels, C. "Isotherms of CO_2 Between 0° and 150° and Pressures from 16 to 250 Atm...." Proc. Roy. Soc. London, A 153, #A878, 201-214 (1935). 39

Mie, G. Ann. Physik 11, 657 (1903). 49

Münster, A. "Theory of the Liquid State" in Physics of High Pressures 241-296, ed. van Itterbeek, North-Holland Pub. Co., Amsterdam (1965). 49

Oberly, Ralph; Rao, K. Narahari; Hahn, Y. H.; McCubbin, Jr., T. K. "Bands of Carbon Dioxide in the Region of 4.3 Microns" Jnl. Molec. Spectr. 25, 138-165 (1968). 100, 105, 107

Parratt, Lyman G. Probability and Experimental Errors in Science J. Wiley & Sons, N. Y. (1961). 80

Perkin-Elmer. "Introduction to Infrared Spectrophotometry" Rpt. #990-9000, Perkin-Elmer Corp., Norwalk, Conn. (1952). 27

———. "Instruction Manual...Vol. 3A: Model 112/12C Single-Beam Single-Pass Spectrometer" Rpt. #990-9002, Perkin-Elmer Corp., Norwalk, Conn. (1956). 15

———. "Instructions: 40-Meter Long Path Cell" Rpt. #990-9070, Perkin-Elmer Corp., Norwalk, Conn. (1959). 10, 24

Pilston, Robert G. Private communication (1972). 23

Plyler, Earle K.; Peters, C. Wilbur "Wavelengths for Calibration of Prism Spectrometers" Jnl. Resch. of the NBS 45, #6, 462-468 (1950). 27

Pollack, J. B.; Morrison, David "Venus: Determination of Atmospheric Parameters from the Microwave Spectrum" Icarus 12, 376-390 (1970). 60

Rasool, S. Ichtiaque; deBergh, Catherine "The Runaway Greenhouse and the Accumulation of CO_2 in the Venus Atmosphere" Nature 226, #5250, 1037-1039 (1970). 59

Sagan, Carl. "The Radiation Balance of Venus" Tech. Report #32-34, Jet Propulsion Lab., Cal. Inst. of Tech., Pasadena (1960). 60

Statz, H.; Tang, C. L.; Koster, G. F. "Transition Probabilities Between Laser States in Carbon Dioxide" Jnl. Appl. Phys. 37, #1, 4278-4284 (1966). 50, 95

Stoicheff, B. P. Ph.D. Thesis, Univ. of Toronto (1950) 46

Stull, V. R.; Wyatt, P. S.; Plass, G. N. "The Infrared Absorption of Carbon Dioxide" Rpt. #SSD-TDR-127 Vol. II, Aeronutronic Div., Ford Motor Co., Newport Beach, Cal. (1963). 33, 55, 100

Thaddeus, Patrick. "The Composition of the Atmosphere of Venus" A report at the 45th Session of the American Geophysics Union, Washington (1964). 1, 60

_____. "The Dry Massive Model of the Atmosphere of Venus and the Microwave Phase Effect" in The Atmospheres of Venus and Mars 99-102, eds. Brandt & McElroy, Gordon & Breach, N. Y. (1968). 68

Vu, Hai. Ph. D. Thesis, Jnl. Recherche C. N. R. S. 11, 313 (1960). 33

Wattson, Richard. Private communication (1969). 75

Welsh, H. L.; Crawford, M. F.; Locke, J. L. "Infrared Absorption of Hydrogen and Carbon Dioxide Induced by Intermolecular Forces" Phys. Rev. 76, 580 (1949). 38

White, John U. "Long Optical Paths of Large Aperture" Jnl. Optical Soc. Amer. 32, 285-288 (1942). 3

The Fortran program for radiation properties of planetary atmospheres is available on request.

Portions of this work are being submitted for publication in Icarus and the Journal of Molecular Spectroscopy.